RICE UNIVERSITY

Tectonic and gravitational fold and thrust belts:
Insights from discrete element simulations and
Galicia Bank ocean-continent transition zone: New seismic reflection
constraints

by

Sarah Lois Dean

A THESIS SUBMITTED
IN PARTIAL FULFILLMENT OF THE
REQUIREMENTS FOR THE DEGREE

Doctor of Philosophy

APPROVED, THESIS COMMITTEE

Julia Morgan,
Professor, Earth Science

Dale Sawyer
Professor, Earth Science

Brandon Dugan
Associate Professor, Earth Science

John Anderson
Ewing Professor, Earth Science

John E. Akin
Professor, Mechanical Engineering

HOUSTON, TEXAS
June 2014

ABSTRACT

Tectonic and gravitational fold and thrust belts:
Insights from discrete element simulations
and
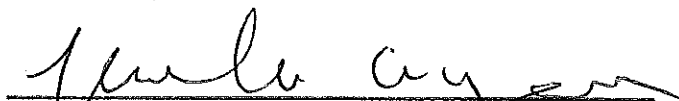Galicia Bank ocean-continent transition zone: New seismic reflection constraints

by

Sarah Lois Dean

The evolution and formation of tectonically and gravitationally driven fold and thrust belts were investigated with 2D numerical simulations using the discrete element method (DEM). In the tectonic study, the occurrence of triangle zones at the front of thrust belts was investigated, specifically how mechanical stratigraphy affects their formation. Simulations with homogenous stratigraphy deformed predominantly along forethrusts. Adding a weak upper unit caused more forethrusts and popup structures in the upper unit relative to the lower unit. Thicker décollement surfaces and strong upper and lower units enhanced decoupling and formed triangle zones. Results compared favorably with triangle zones in Alberta, Canada.

Simulations of gravitationally driven thrust belts consisted of an upslope extensional zone, syntectonically loaded with sediments, which is connected at depth to a downslope contractional zone. The whole system overlies a mobile shale unit. Our simulations show more diffuse décollements connecting the normal faults in the extensional zone with toe thrusts in the contractional zone, then are interpreted on seismic profiles. We also look at the distributions of stress and strain within out simulations, relating the distributions of the maximum principle stress direction to the vergence of thrust faults. We compare out models to the Niger Delta type locale for shale tectonics.

The West Iberia continental margin is a type locale for magma-poor rifting, and studies there have been instrumental in changing the classical view of the ocean-continent transition (OCT) from a discrete boundary juxtaposing continental and oceanic crust, into a more complicated zone of varying width that can include exhumed mantle. This study examines two new seismic lines in the Galicia Bank area extending west of the Peridotite Ridge, showing high resolution images of five new ridges. These ridges could be hyperextended continental crust, exhumed continental mantle, or rough ultra-slow spreading oceanic crust. There are no tilted fault blocks with pre-syn rift stratigraphy that would indicate continental crust. There are also no faults indicating mid-ocean spreading with seismic layer stratigraphy indicating normal oceanic crust. Therefore, it is likely the western ridges are also made of serpentinized mantle, defining a wide OCT similar to the southern Iberia abyssal plain.

Acknowledgments

Contents

List of Figures

List of Tables

Preface

This thesis consists of an introduction (Chapter 1) and three separate papers, each of which is a complete and independent document. Chapter 2 is a paper that was published in the Journal of Structural Geology in August 2013 (Dean et al, 2013). Co-authors are my thesis advisor Julia Morgan and Thomas Fournier, now at Shell Exploration and Production in Houston.

Chapter 3 is a paper that is accepted pending revision at the American Association of Petroleum Geologists Bulletin. Co-authors are Julia Morgan and JP Brandenburg, at Shell Exploration and Production in Houston.

Chapter 4 is a paper on the 2013 Galicia Seismic Survey that is in preparation for submission. Co-authors are Julia Morgan and Dale Sawyer.

The references have been combined into one section at the end of the document. Figure numbers reflect both the chapter and the place within the chapter (e.g., the first figure in Chapter 1 in Figure 1.1, the first figure in Chapter 2 is 2.1, etc.).

Chapter 1

Introduction

This study looks at the process by which continental margins deform, including tectonic contraction through the formation of fold and thrust belts, continental rifting to form a passive margin, and finally gravitationally driven deformation on a passive margin. I look at independent pieces of this continuum through three different projects and using two different approaches.

Observations of the stratigraphy and structures of different fold and thrust belts has found that frontal structures of some fold and thrust belts consist of units that dip toward the foreland rather than the hinterland. The basin-ward dipping horizons are indicators of a triangle zone, where the thrust belt has formed a wedge under the foreland basin, passively lifting the overlying sediments along a backthrust. Frontal structures record the earliest stages of deformation in a deforming belt, giving us insight into the initiation of thrust belts. In addition, frontal structures, particularly triangle zones, can be important hydrocarbon traps. The presence or absence of triangle zones been linked to the broad scale mechanical stratigraphy of the different thrust belts, specifically the ratio of strength between a lower duplexing unit and a sedimentary cover sequence (Couzens and Wiltschko, 1996). The first part of this study focuses on the frontal structures of fold and

thrust belts, and how large scale mechanical stratigraphy affects the presence and evolution of triangle zones.

In contrast to tectonically driven systems, gravitationally driven fold and thrust belts form on passive margins, and are typically composed of deepwater sediments and poorly lithified sandstones and shales. Many systems are underlain by overpressured shale or salt, which can be mobilized under low stress gradients, enabling downslope movement. Deformation in these systems typically consists of extension in the shallow areas, where rapid sedimentation occurs (e.g., in deltas), and contraction in deepwater, basinward areas in response to downslope movement. Mobile shale is usually transparent in seismic reflection data, making it difficult to recognize, and obscuring the details of internal deformation, for example, the existence of a discrete décollement that might link the zones of up-dip extension and down-dip contraction. The second part of this study investigates the evolution of both the décollements and the fold and thrust belts in the contractional zone of a gravity driven system overlying a mobile shale unit.

Conclusions from field observations and seismic interpretations can be tested through use of simplified numerical models. Forward models can be used to show the evolution of structures through time, and numerical models can provide stress and strain information about the deforming area. The Discrete Element Method (DEM), designed by Cundall and Strack (1979), allows for the simulation of large amounts of strain, an important consideration for development of fold and thrust belts, and can form discrete faults and/or distributed shear, allowing for investigations into amounts of localization. DEM can also reproduce realistic rheologies for sediments and rocks that experience brittle failure and frictional sliding, but also can approximate the assumed viscous rheology of

mobile shale. Here, it was used to simulate both tectonic and gravitational fold and thrust belt systems. DEM offers the ability to monitor and probe the progressive structural and mechanical evolution of the systems as well as the final stage, allowing for insight into the deformation process,

The third part of my study looks at the basement of the Iberia passive margin, which preserves the record of continental rifting and transition to oceanic spreading. This transition from continental rifting to seafloor spreading is a fundamental process in plate tectonics, but many details about the mechanics of the transition to oceanic crust remain poorly understood. Iberia and Newfoundland are ideal places to study the mechanical aspects of rifting processes because they are largely devoid of igneous and salt bodies that obscure seismic imaging, create volume conservation problems, and make it difficult to study the system using scientific ocean drilling (Borgmeyer, 2010). Seismic studies of the Iberia margin have shown that these rifted margins are typically characterized by landward-rotated, fault-bounded continental blocks that thin progressively seaward (Reston et al., 1996) until there is no more continental crust and instead serpentinized peridotite (hydrated upper mantle) is exhumed in the form of N-S trending peridotite ridges (Beslier et al, 1993; Henning et al, 2004). Oceanic crust has been assumed to occur just west of the peridotite ridge (Whitmarsh et al, 1996) but until now, few data of limited quality was available to study the nature of this region. I process and interpret two 2D seismic reflection profiles from the 2013 Galicia 3D Seismic Project, located on Iberia's thinned Galicia Basin, in order to characterize the crust west of the Peridotite Ridge.

Chapter 2

Geometries of frontal fold and thrust belts: Insights from discrete element simulations

2.1. Abstract

This study investigated the evolution of frontal structures of fold and thrust belts with 2D numerical simulations using the discrete element method (DEM). Of specific interest is the occurrence of triangle zones, and how mechanical stratigraphy affects the formation of the triangle zones. In our simulations, we varied the strength of a two unit stratigraphy, as well as the décollement horizons, to determine the controlling parameters of different types of frontal structures. For models with homogenous stratigraphy, deformation was concentrated along forethrusts, which involved both the upper and lower units. With the addition of a mechanically weak upper unit, deformation along forethrusts and popup structures largely occurred in the upper unit with relatively little deformation of the lower unit. With thicker décollement surfaces and strong upper and lower units, decoupling was enhanced and allowed for the formation of triangle zones in front of the deforming wedge. The triangle zones were uplifted along lower forethrusts, until a new frontal triangle zone formed. Results compared favorably with triangle zones found in the Canadian Cordillera in southern Alberta.

2.2. Introduction

Frontal structures of thin skinned fold and thrust belts often consist of units that dip towards the foreland basin with little evidence of shortening at the surface, contrasting with the hinterland dipping forethrusts that dominated the rest of the belt (Vann et al 1985). The basin-ward dipping horizons are indicators of a frontal triangle zone, where a major backthrust has passively lifted the overlying sediments. This model was first proposed by Gordy et al, (1977) and similar structures were referred to as passive-roof duplexes by Banks and Warburton (1986). Triangle zones are so named due to their appearance on seismic data (Jones, 1996) with the presence of conjugate dipping reflectors above a horizontal décollement forming a triangle of prominent reflectors (Figure 2.1b). The presence of frontal triangle zones has been recognized in thrust belts around the world, but the mechanical processes responsible for their presence or absence are not fully understood.

Numerical simulations have provided insight into the processes of frontal deformation and the incorporation of new material into fold and thrust belts, showing how they may evolve over time. Numerical models can also be used to assess the influences of different stratigraphies for the formation of various structures over time. Here, we use the discrete element method (DEM) to gain insight into the frontal processes and structures of fold and thrust belts. DEM has been used previously to study accretionary prisms, (Naylor et al, 2005; Yamada et al, 2006; Hardy et al, 2007) fold and thrust belts (Burbidge and Braun, 2002), detachment folds (Vidal-Royo et al, 2010), fault bend and fault propagation folds (Benesh et al, 2007; Cardozo et al, 2005) and volcanic deformation (Morgan and

McGovern, 2005; Hardy, 2008). In this study, we explore the role of mechanical

stratigraphy in order to determine their first order controls on fold and thrust belt

structural geometries and evolution, and to test hypotheses about the role of mechanical

stratigraphy on the formation of triangle zones.

2.3. Background

Couzens and Wiltschko (1996) examined the stratigraphy and structures of

different fold and thrust belts, to determine the controlling factors for triangle zone

formation. From their observations, they concluded that the relative internal strength

between a buried duplex unit and its cover sequence controlled the vergence of thrust

faults at the deformation front of a fold and thrust belt. They hypothesized that the

presence of a weak cover sequence corresponded to the formation of backthrusts that

passively lifted the cover sequence and carried it toward the hinterland, as the underlying

duplex was thrust toward the foreland (Figure 2.1b).The Cordilleran fold and thrust belt in

Alberta, Canada, served as an example (Figure 2.1e, f), with its abundance of well-studied

frontal triangle zones (e.g. Jones, 1982; Jamison, 1993; Lawton, 1996; Mackay et al, 1996;

Skuce, 1996; Slotboom 1996; Stockmal, 1996; Stockmal, 2001). By contrast, if a duplex and

cover sequence have similar strengths Couzens and Wiltschko (1996) hypothesized it

would deform through forethrusting in both the duplex and cover units (Figure 2.1a). The

central Appalachians have a relatively strong cover sequence, which is assumed to be

responsible for the lack of triangle zones and frontal backthrusts (Figure 2.1c, d).
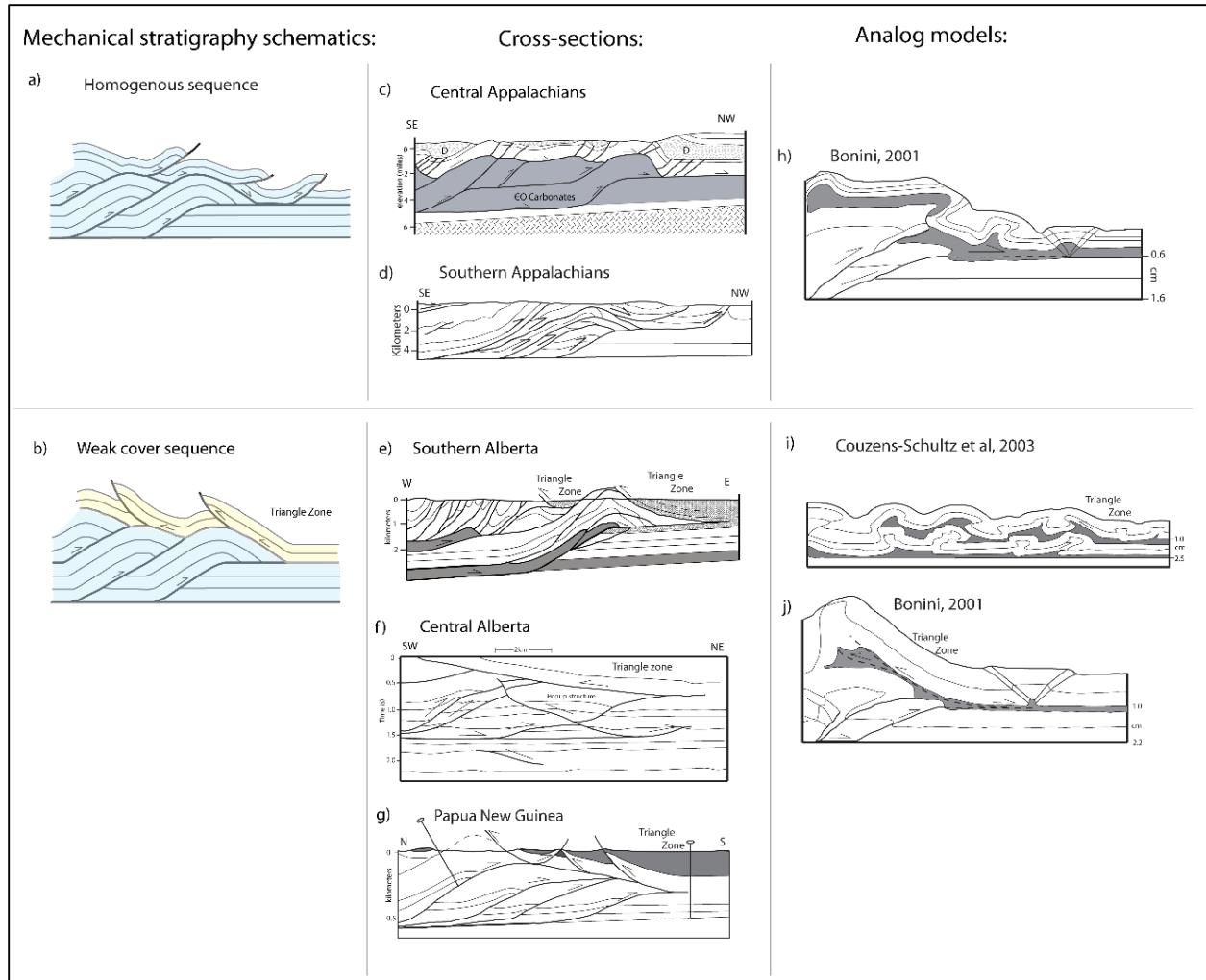
Figure 2.1 - Schematics, cross-sections, and analog models of folded belts with and without triangle zones. a) Schematic of a system without triangle zones, where the duplexing unit and cover sequence are mechanically similar (i.e. both blue) (modified from Couzens and Wiltschko, 1996). b) Schematic of a system with a triangle zone, where a weak cover unit (yellow) overlies a mechanically stronger unit (blue) (modified from Couzens and Wiltschko, 1996). c), d) Examples of fold and thrust belts from the Appalachians without triangle zones (modified from Couzens and Wiltschko, 1996; Couzens-Schultz et al., 2003; respectively). e), f), g) Examples of fold and thrust belts with triangle zones (modified from Couzens and Wiltschko, 1996; Lawton et al., 1996; Medd, 1996; respectively). h) Example of an analog fold and thrust belt model without triangle zones (modified from Bonini, 2001). i), j) Examples of analog fold and thrust belt models that formed triangle zones (modified from Couzens-Schultz et al., 2003; Bonini, 2001; respectively). Shaded regions in h), i) and j) represent silicone putty, used to simulate weak décollement zones.

Bonini (2001) studied the formation of passive roof duplexes using analog sand and silicone models (Figure 2.1h, j). His results suggested that foreland vergence dominates in most systems, but that backthrusting and dual vergence occurred in cases of a relatively weak décollement, weak coupling between the décollement and upper unit, or along-strike variations in décollement properties or geometry, including the occurrence of transverse faults (Bonini 2007). However, Bonini did not study the effects of a weak cover sequence. Thus, we hypothesize that both a weak décollement and a weak cover sequence may produce triangle zones, and we will test both parameters and attempt to determine their relative importance.

Couzens-Schultz et al (2003) performed similar analog models to Bonini (2001), where dry sand units were alternated with two décollement units of silicone polymers (Figure 2.1i). In their models, due to the viscosity of the material used, the strength of the décollements relative to the wedge was controlled by the shortening rate applied to the models. Strong décollements promoted underthrusting of the wedge beneath the upper unit of their models, forming triangle zones due to the shear resistance to forward propagation of the décollement. Weak décollements promoted forethrusting in the cover sequence, allowing it to move into the foreland by slipping on the décollement horizon. Therefore, in both analog studies, variation in décollement strength relative to wedge strength indicated a strong influence on the orientation and formation of frontal structures in fold and thrust belts. However, Bonini's results suggested the need for weak décollements, whereas Couzens-Schultz specified the need for a relatively strong upper décollement. The DEM simulations will allow us to quantify the role of these different strength conditions.

Stockmal et al (2007) expanded on these results with finite element models (FEM), which examined uniform, homogeneous wedge as well as wedges with two to three additional weaker units bounded by décollements. All of these models showed popup structures forming in front of the deforming wedge, which subsequently organized into larger forward verging thrust sheets. According to Stockmal et al (2007), the resulting structures were kinematically similar to those in fold and thrust belts in general and the southern Canadian Rockies in particular. However, none of their results produced frontal triangle zones, which are prevalent in the Canadian Cordillera in southern Alberta.

In this study, we test different mechanical stratigraphies using DEM simulations in order to observe their effects on frontal structures and the development of a fold and thrust belt. Our simulations also test whether any of the geometries support or reject previous hypotheses for the formation of triangle zones, and why they form in some mountain ranges and not in others.

2.4. Discrete Element Method

The discrete element method (DEM) is a numerical approach based on the interaction of discrete particles using the laws of contact physics. It is an effective tool for simulating elastic-frictional deformation in materials subject to brittle deformation and frictional slip. The original code (TRUBAL) was developed by Cundall and Strack (1979) and was adapted for this application (now referred to as RiceBal) as summarized by Morgan and Boettcher (1999) and Morgan and McGovern (2005). DEM has been used to simulate shallow crustal rocks subject to Coulomb behavior, as the particle assemblages

can form discrete structures, such as faults and shear zones that evolve over time. For

example, Morgan and Boettcher (1999) and Guo and Morgan (2004) and others used DEM

to simulate shear zones and micromechanics, while Morgan and McGovern (2005) and

others investigated deformation of volcanic edifices, and Naylor et al (2005) modeled the

evolution of an accretionary prism. In this study, we used DEM simulations to study

stratigraphic layers subjected to horizontal compression, leading to the formation of fold

and thrust belts.

DEM uses a time-stepping finite difference approach to solve Newton's equations of

motion for all particles in the system; solving

$$F_p = m_p * \ddot{x}_p$$ (Equation 1)

$$M_p = I_p * \ddot{\theta}_p$$ (Equation 2)

where F_p and M_p are the net force and net moment acting on each particle, m_p and I_p are the

mass and moment of inertia, and $\ddot{x}_p$ and $\ddot{\theta}_p$ are the linear and angular accelerations of the

particles. Gravitational forces, interparticle contact forces, and external forces prescribed at

the boundaries are summed for each particle and substituted into equations (1) and (2)

and solved for particle velocities and displacements (Figure 2.2). As particles are displaced,

they interact with adjacent particles. The calculation of contact forces is alternated with the

calculation of particle displacements which changes the net forces on each particle again,

and the process repeats until the whole assemblage is in equilibrium (e.g., Morgan and

McGovern, 2005).

The interparticle contact forces obey Hertz-Mindlin contact theory (nonlinear), where cohesionless particles respond elastically to normal forces, and resisted frictional sliding from shear forces. These forces are given by

$$f_n = k_n \, \delta_n \qquad \text{(Equation 3)}$$

$$f_s = k_s \, \delta_s \qquad \text{(Equation 4)}$$

where f_n and f_s are the normal and shear contact forces, δ_n and δ_s are the relative distance between the two particles perpendicular to the contact, and k_n and k_s are the normal and shear stiffness. The stiffnesses are nonlinear and a function of the contact area (Johnson, 1985). The shear force is limited by the interparticle coefficient of friction, so that when the shear forces are large enough, sliding occurs between particles. If slip is highly localized, faults can form (Morgan and McGovern 2005). Cohesion is simulated to create more realistic rock properties by adding bonds between particles (Guo and Morgan, 2004). Bonds introduce additional tensile and cohesive forces; once these bond strengths are exceeded, in either tension or shear, the bond breaks and the particles are free to displace relative to each other, creating faults.

Implicit in this method is that the bulk rheology of the granular material is a product of the particle interactions, rather than being an input property. Properties such as friction, density, and bond shear and normal forces are assigned at the particle scale. Calibration experiments were done using a numerical shear box which allowed us to quantify the bulk properties of the assemblage.

The shear box simulations were performed for selected materials used in the fold and thrust belt models. The simulations have two stages; the first of which is a consolidation stage where the particles are compressed to match their stratigraphic depths in the undeformed section. The particles are then bonded and sheared at five different confining pressures, to yield five shear stress versus shear strain curves (Figure 2.3a). The peak shear stress values (material assumed to be at failure) are plotted against the confining stress to define the Mohr-Coulomb failure envelope for which the material bulk cohesion and coefficient of friction can be measured (Figure 2.3b). These values compare well with values from laboratory experiments, ensuring realistic rock properties for the numerical materials (Table 2.1). The coefficient of friction of our materials is generally low, around 0.3-0.4, presumed to be due to the circular nature of the particles, and their ability to roll relative to one another (Morgan, 2004).

a) Contact Laws (Hertz-Mindlin)

δ_n

f_n

normal force

$f_n = k_n \delta_n$

δ_s

f_s

shear force

$f_s = k_s \delta_s$

$f_s^{max} = \mu_p f_n$

b) Newton's Equation of Motion

$F_p = ma$

f^1

$f^c \ (Fp = \Sigma f^c)$

f^2

c) Bonds

normal spring   shear spring
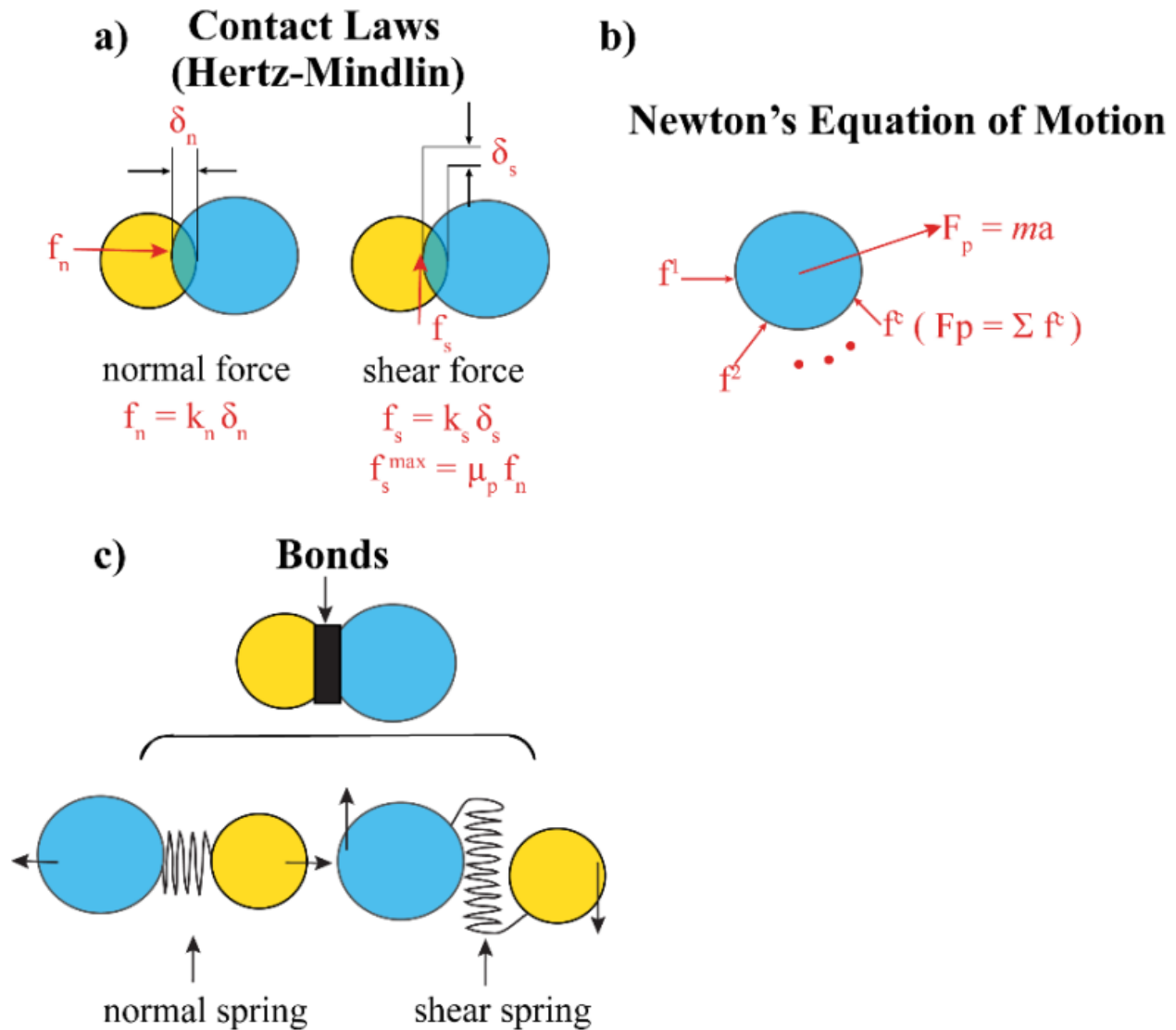
Figure 2.2 - Discrete element method used for this study. a) Particles respond elastically to normal forces, and frictionally resist shear forces. The force displacement laws for each particle are non-linear, implementing HertzeMindlin contact mechanics (Johnson, 1985). b) For each time-step, the contact forces acting on each particle are summed to fi nd the net force, which, using Newton's equation of motion, determines the net movement of the particle. c) Cohesion is introduced by bonding particles together with varying compressive and tensile forces so that the forces acting on the particles must overcome the bonding forces to cause the particles to move (form faults). The bonds break once these forces are overcome, and do not reform.
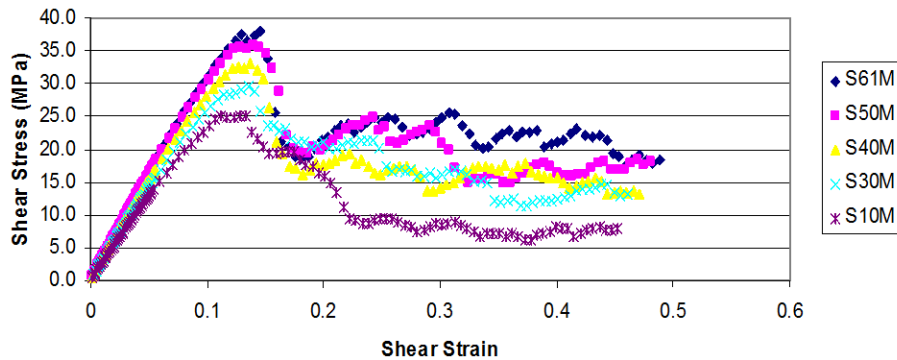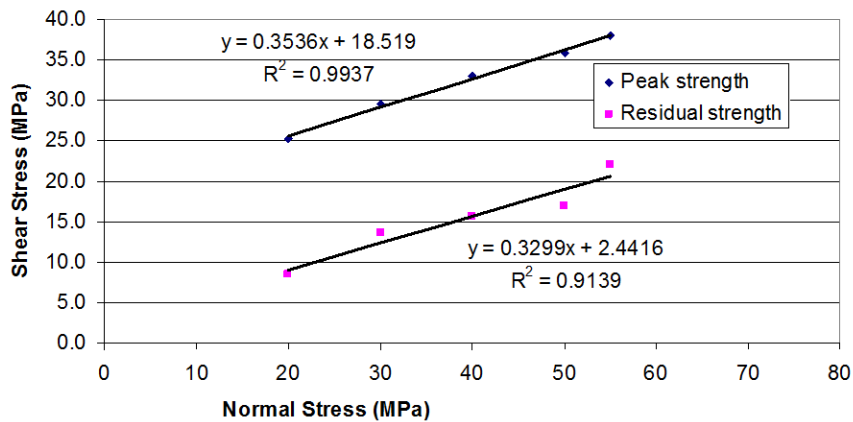
Figure 2.3 - Results of simple shear tests to determine mechanical properties of model materials. a) Shear strain vs. shear stress for each of the five shear tests at different confining pressures for the unit at 1.5 km depth. Each test shows elastic loading to peak strength, followed by strain softening to residual stress (where stress levels out). b) Peak strengths and an average of the residual stress values are plotted against confining stress, defining MohreCoulomb envelopes showing assemblage coefficient of internal friction and cohesion, and coefficient of sliding friction.
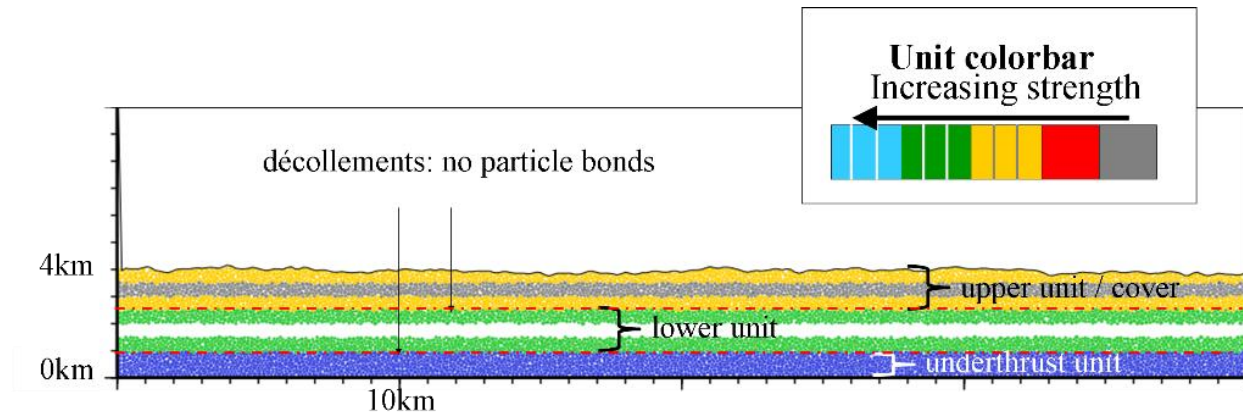
Figure 2.4 – Model setup. Models are created by generating 25,000-50,000 particles, which are allowed to settle under gravity. The particles are then bonded together; color pairs indicate bond strength (see colorbar). The particles along the décollement horizons are unbonded.

2.5. Experimental Design

To model the formation of fold and thrust belts, circular particles were randomly generated within a two dimensional domain. The model domain was 120 km long and 12 km tall. The particles had radii of 40, 60, and 80 m, and a density of 2,500 kg/m^3. The particles were allowed to settle under gravity, and once stable, they were captured into horizontal layers, and each unit was bonded together with different relative strengths (Figure 2.4). The lowest (dark blue) unit was defined as being underthrust the main basal décollement and assigned a high bond strength to limit plastic deformation, and the bonds were reset at regular intervals. A basal décollement was defined immediately above the subducting unit, by a thin layer of particles with no bonds and zero intra-particle friction. The rest of the particles were divided into two overriding units separated by another mechanically weak horizon, representing an upper décollement. Generally the lower unit had higher particle bond strengths, making it mechanically stronger than the uppermost

unit. The upper unit represented a potentially weaker cover sequence for the fold and thrust belt. After the stratigraphy was set up and the particles bonded, the left wall of the domain was moved inward at a rate of 2 m/s, imposing compression against the left side of the strata. The displacement rate was large compared to natural plate convergences rates, but allowed for reasonable computational times. We assume a quasi-static system, where friction is assumed to be constant, and therefore not affected by the fast velocity. Simulations run with slower wall velocities (0.5 m/s) were similar to the faster simulations in the number and distribution of faults. In addition, brittle deformation is largely time independent, so the high displacement rate is not expected to affect the final results significantly.

Since the simulations were two dimensional, they do not account for any out of plane motion that might occur along strike in an orogenic belt. Instead, we simulated different mechanical configurations that might occur in a fold and thrust belt to represent this variability. The simulations also simplified the basal geometry by not including subsidence or flexure. The effects of thermal heating or pore fluid pressure evolution were not incorporated in the models. Despite these simplifications, the simulations are able to produce many fold and thrust belts structures seen in natural systems. The addition of mechanically different stratigraphic units added a level of complexity to previous homogenous models (e.g. Burbidge and Braun, 1999; Bonini, 2001; Bonini, 2007; Couzens-Schultz et al, 2003).

simulation	color	Co (MPa)	μ	simulation type
MS001	upper unit	13	0.3	
	lower unit	19	0.4	uniform strength
MS004		16	0.3	
		23	0.3	
MS002		8	0.4	
		19	0.4	
MS021		8	0.4	weak cover sequence
		23	0.3	
MS022		13	0.3	
		23	0.3	
MS002c	upper unit	8	0.4	
	décollement	5	0.4	
	lower unit	19	0.4	weak decollement and
MS021c		8	0.4	weak cover sequence
		5	0.4	
		23	0.3	
MS039		16	0.3	
		5	0.4	
		23	0.3	weak decollment
MS040		13	0.3	
		5	0.4	
		19	0.4	
MS021b		8	0.4	
		0.5	0.1	
		23	0.3	unbonded decollement
MS002b		8	0.4	
		0.5	0.1	
		19	0.4	

Table 2.1 - Simulation geometries and bulk properties: coefficient of internal friction and cohesion values from shear box calibration simulation models for the each fold and thrust belt simulations. Colors denote strength of the units in simulations.

2.6. Results

The primary objective of this study was to determine the influences of various mechanical stratigraphies on frontal structures of fold and thrust belts. The first set of simulations had similar strengths for the top and bottom layers, with the bounding upper and lower weak décollement horizons. Subsequent simulations were carried out with various strengths for the upper, lower, and décollement units, with different colors for each unit, representing the relative strength of the units (Table 2.1). The evolution of each simulation is illustrated by four representative snapshots of the system during deformation (out of 200 total images) showing the particle configuration and the cumulative distortional strain, calculated as the second strain invariant of the deviatoric strain tensor (Figure 2.5-2.8). Zones of intense shear strain have high values of distortion, and therefore plots of distortional strain can be used as a proxy for shear strain.

2.6.1. Homogenous strength simulation (MS001)

Simulation MS001 tested the effect of a uniform strength upper (cover sequence) and lower units (Figure 2.5). The two décollement surfaces were 100 m or one particle thick, and unbonded. There was 2.8 km of layer parallel shortening before the initiation of the first forethrust. Deformation was dominated by forethrusts (Figure 2.5), which alternated between breaking the entire sequence or just the upper unit, merging with the upper décollement horizon. A backthrust formed in the middle of the simulation (Figure 2.5b) but was subsequently overturned by another forethrust located behind it. Minor backthrusts also occurred as conjugate faults in popup structures (Fault 7, Figure 2.5c). They accommodated relatively little movement relative to the associated forethrust. Therefore, much of the deformation occurred in the upper unit, and along the upper décollement, but several faults broke to the lower décollement, thrusting the lower unit over the upper unit, although the upper unit was also thrust separately over the foreland along the upper décollement.

Figure 2.5 – Simulation MS001. Reference simulation with the same strength for both upper and lower units. Particle configurations are shown on the left, overlain by the second strain invariant of the deviatoric strain tensor (distortional strain) on the right. The inset in d) shows the cohesion (C, MPa) and the coefficient of friction (μ) for each layer. a) Image 043 shows initial frontal forethrusts 1,2, and 3. b) Image 078 shows the formation of a backthrust 4, which is overridden by the subsequent forethrust 5. c) Image 143 shows a return to forethrusting, with thrust 6 merging with the upper décollement while thrust 7 merges with the lower décollement. Both formed initial popup structures, with conjugate fore and backthrusts at the surface. Subsequent motion occurs on the forethrust. d) Image 199 shows continued forethrusting involving both the upper and lower units (faults 8, 9). (Figure on next page)
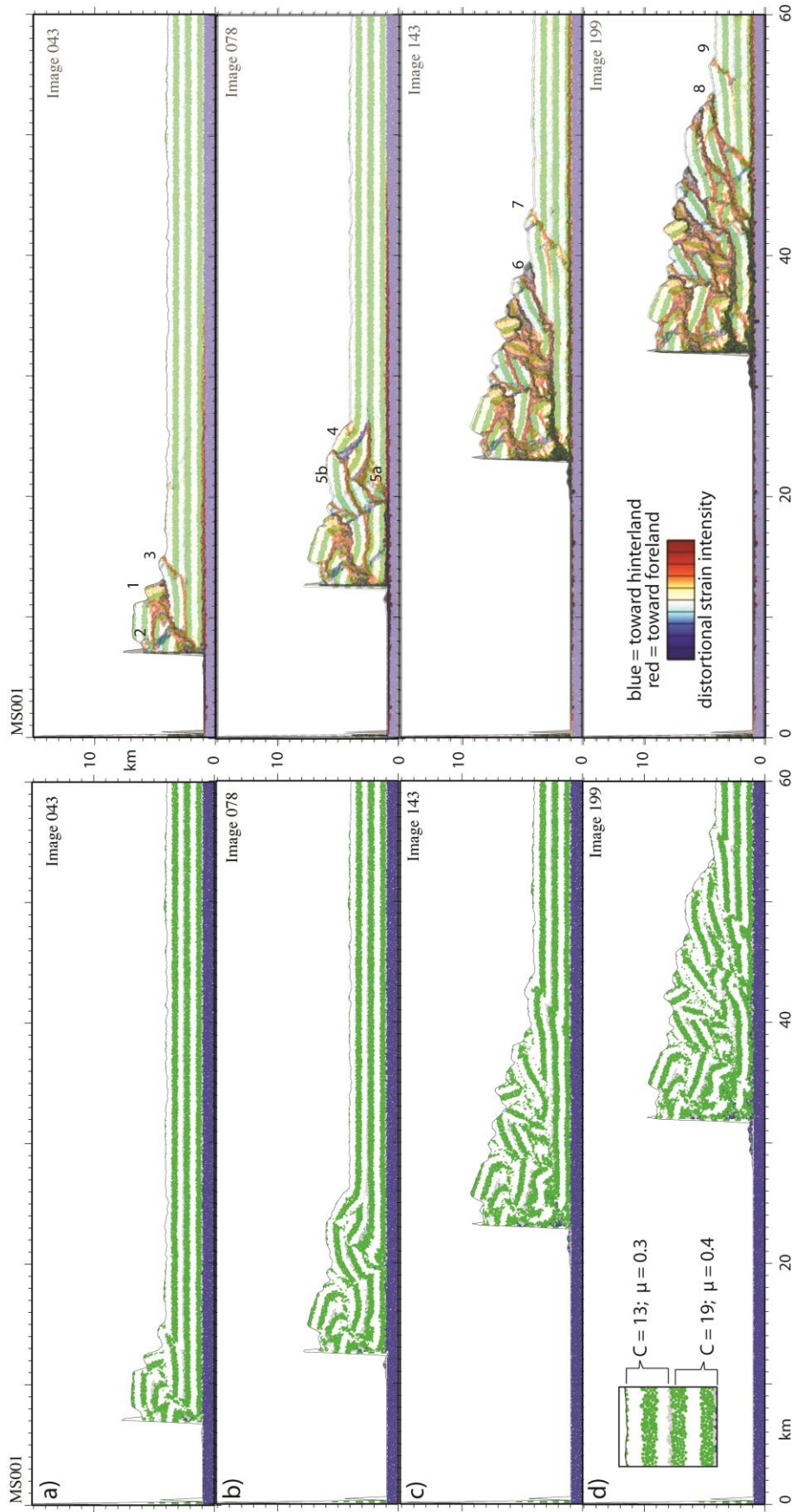
Figure 2.6 – Simulation MS021. Weak cover sequence simulation with the upper unit (yellow) having lower bond strengths then the lower unit (blue). Particle configurations are shown on the left, overlain by the second strain invariant of the deviatoric strain tensor (distortional strain) on the right. The inset in d) shows the cohesion (C, MPa) and the coefficient of friction (μ) for each layer. a) Image 050 shows an initial backthrust (fault 1) which is tilted by movement on fault 2, and turns into a popup structure with conjugate fault 1b. Forethrusting becomes dominant with the formation of fault 3. b) Image 074 shows the formation of a popup structure along conjugate faults 4a and b, and the subsequent slip along the forethrust (4a) as it reaches the lower décollement. c) Image 130 shows forethrusting of the cover unit with the initiation of faults 5 and 6. d) Image 200 shows continued deformation in the upper unit, with the creation of successive popup structures along faults 7a and b and 8a and b and a forethrust forming fault 9. (Figure on next page)
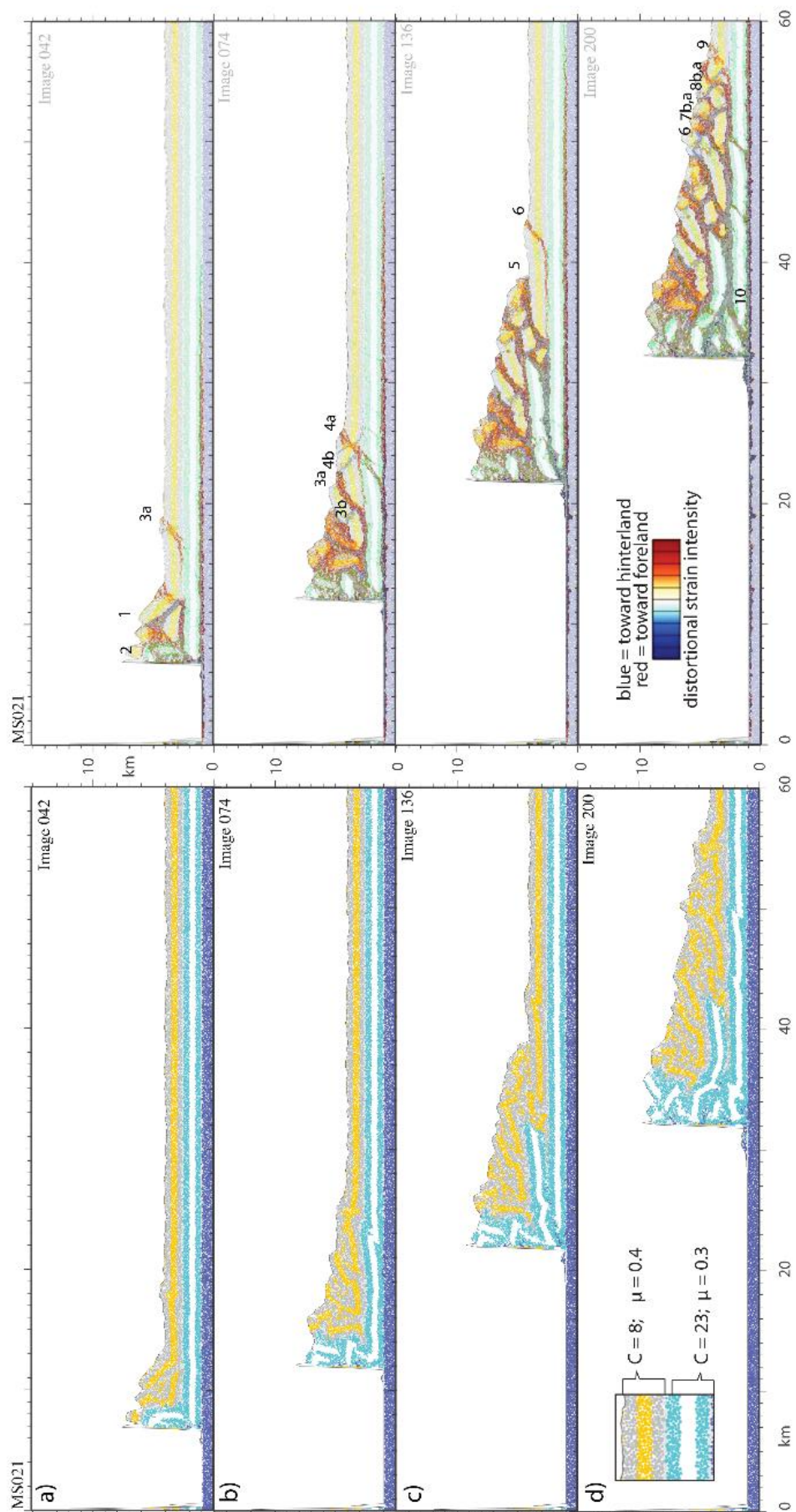
Figure 2.7 – Simulation MS021c. Thick shale/décollement simulation with thick, weakly bonded units at the décollement levels, with an additional weak cover sequence. Particle configurations are shown on the left, overlain by the second strain invariant of the deviatoric strain tensor (distortional strain) on the right. The inset in d) shows the cohesion (C, MPa) and the coefficient of friction (μ) for each layer. a) Image 043 shows the formation of forethrust 1, followed by a backthrust (fault 2) which turns into a popup structure with forethrust 3, which also merges with the upper décollement. b) Image 104 shows continued building of the wedge along forethrusts, one of which (fault 5) reaches the lower décollement and thrusts the lower unit over the upper one. c) Image 130 indicates a return to deformation in the upper unit along faults 6 and 7, the later of which starts as a popup structure. d) Image 200 continues deformation of the upper unit along faults 8a and b. A duplex system also forms near the moving wall. (Figure on next page)
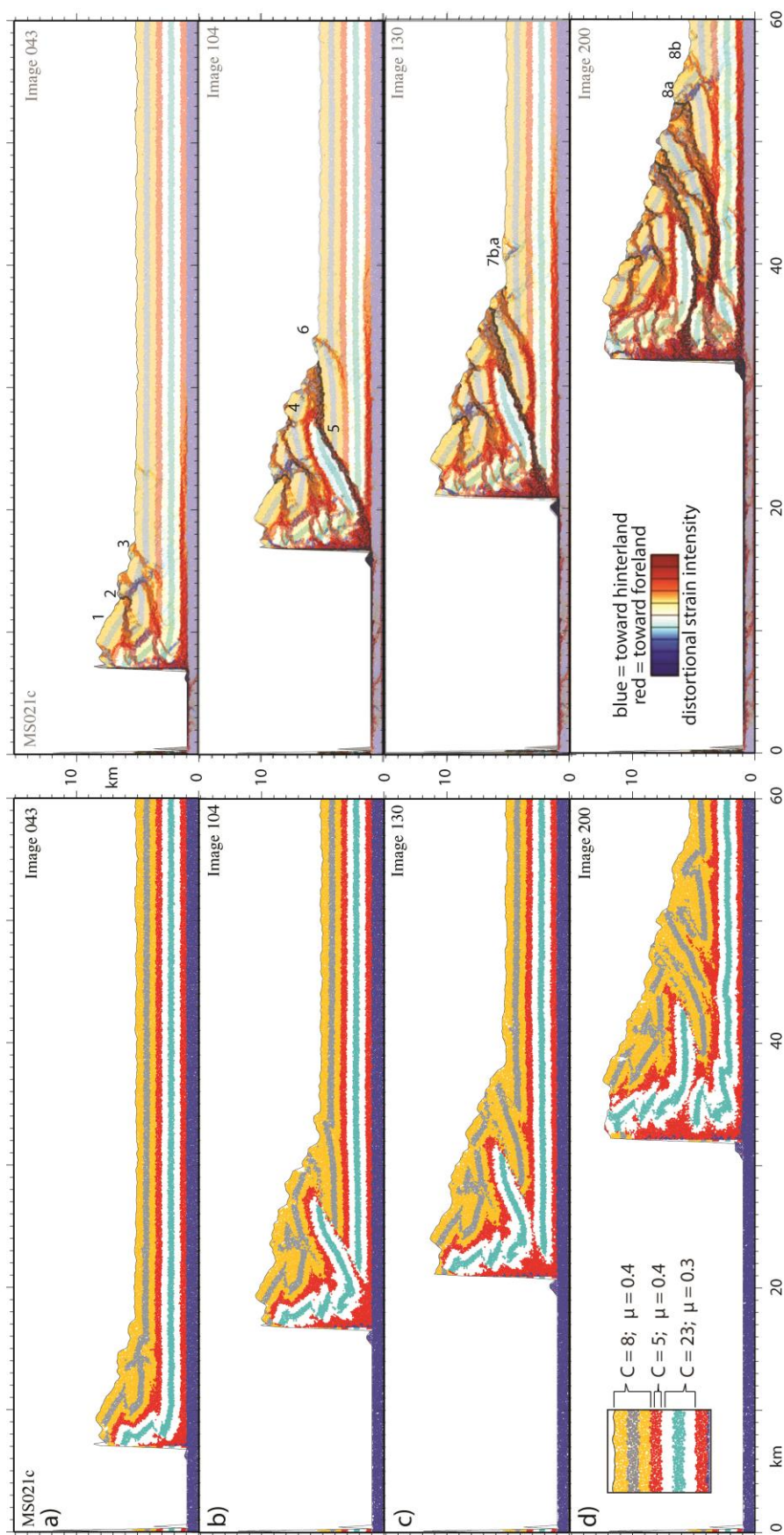
Figure 2.8 – Simulation MS039. Simulation where the weak décollement units are surrounded by strong lower and upper units. Particle configurations are shown on the left, overlain by the second strain invariant of the deviatoric strain tensor (distortional strain) on the right. The inset in d) shows the cohesion (C, MPa) and the coefficient of friction (μ) for each layer. a) Image 050 shows the initiation of deformation, along one backthrust (fault 1) and subsequent forethrusts (faults 2, 3, 3b) which build up a tectonic wedge. b) Image 108 shows the formation of a triangle zone along faults 5a and b. c) Image 138 shows faults 5b uplifting the triangle zone to the surface. d) Image 165 shows the formation of a second triangle zone along faults 7a and b. Similar repetition of triangle zones is seen in places in Alberta where the upper triangle zone has not been completely eroded (Figure 2.1a). (Figure on next page)
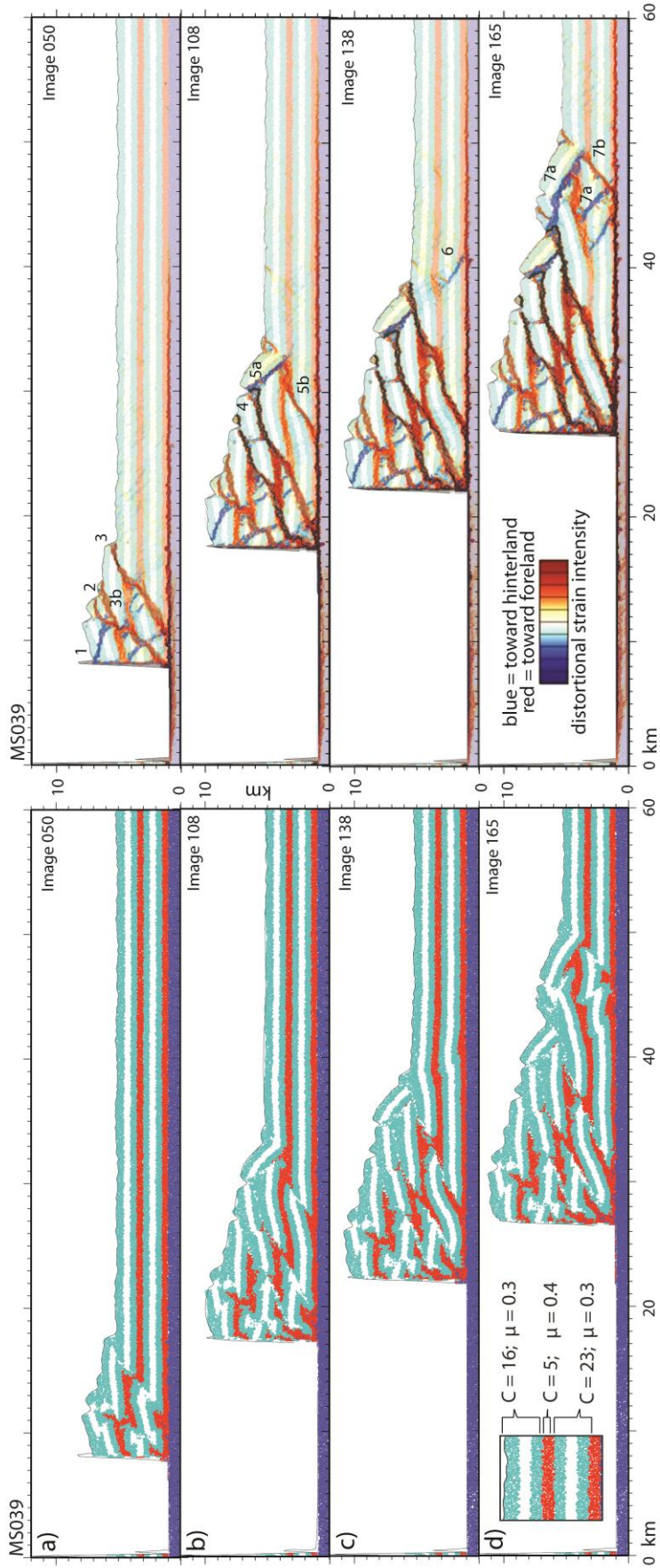
2.6.2. Weak Cover sequence simulation (MS021)

Simulation MS021 tested the effect of a mechanically weak cover sequence over a stronger cover sequence (Figure 2.6). The décollement surfaces were 100 m or ~ one particle thick, and unbonded. There was 1.8 km of layer parallel shortening before the initiation of the first fault. The first fault was a backthrust, forming at the surface and then breaking to and merging with the upper décollement. The next fault was a forethrust, breaking behind the backthrust to form an upside down popup structure. The third fault stepped into the foreland, verging toward the hinterland (Figure 2.6a), and started the sequence of foreland vergent thrusts that characterized subsequent deformation. Many of these forethrusts started as or evolved into popup structures, with conjugate backthrusts forming at the intersection of the forethrust and the upper décollement horizon (Faults 3b, 4b in Figure 2.6b). While one thrust (4a) did cause overthrusting and duplication of the lower unit, the rest of the deformation took place in the upper, weaker, unit, which showed comparatively more frontal deformation then the lower unit (Figure 2.6c,d). Faulting was imposed on the hinterland section of the lower unit as it intersected the moving wall, causing the formation of an antiformal duplex next to the wall (Figure 2.6d). In addition, there was considerable reactivation of older faults after they were rotated and uplifted by the new faults forming in front of the deforming wedge. There also was the tendency, once a wedge shape was established, for faults to form a stair-step geometry with a ramp forming in front of the deforming wedge, merging with the flat upper décollement, and linking with a ramp in the lower unit next to the moving wall. Therefore, most of the deformation occurred in the upper unit, with only one fault breaking into the lower unit to

thrust it towards the foreland. Otherwise, faulting in the lower unit was caused by the displacement of the moving wall, forming an antiformal duplex at the rear of the wedge.

2.6.3. Weak décollement simulation (MS021c)

Simulation MS021c tested the addition of a weak décollement to the weak cover sequence (Figure 2.7). The two décollement surface thicknesses were increased to 500 m and weakly bonded to represent a shale horizon. There was 2 km of layer parallel shortening before the initiation of the first forethrust, which cut from the surface to the upper décollement, before subsequently breaking in to the lower unit. Aside from popup structures, forethrusts dominated the deformation throughout the simulation, even with the enhanced decoupling created by the thicker décollement horizons. Similar to the previous simulation, only one fault (Fault 5, Figure 2.7b) broke to the lower unit and thrust it up over the upper unit. Otherwise, deformation in the front of the wedge remained in the upper unit as it was repeatedly cut by forethrusts (Figure 2.7c, d). The lower unit did form an antiformal duplex next to the moving wall at the rear of the wedge. These blind forethrusts that formed the duplex usually linked up with the upper décollement horizon, which merges with the forethrusts at the front of the wedge to form a ramp-flat-ramp geometry (Figure 2.7d).

2.6.4. Weak Décollement simulation 2 (MS039)

Simulation MS039 tested the effect of a weak décollement with a strong lower and upper units (Figure 2.8). The décollements were 500 m thick, with weak bonds to represent shale. There was 3 km of layer parallel shortening before the initiation of the first

thrust, which was a backthrust that merged with the upper décollement. Subsequent deformation occurred along a series of forethrusts that broke both the upper and lower units and uplifted them towards the surface Figure 2.8a). Secondary slip occurred on the upper décollement, which thrust the upper unit over the surface. Deformation then stepped into the foreland, as a new backthrust broke at the surface, merging at depth with a subsequent blind forethrust, together forming a frontal triangle zone (Figure 2.8b). The forethrust later broke to the surface, passively uplifting the backthrust and triangle zone (Figure 2.8c). A second triangle zone then formed in the foreland (Figure 2.8d), and was uplifted along the forethrust at the end of the simulation. The repeated triangle zones both initiated with the formation of a frontal backthrust, which was joined at depth by a blind forethrust. This forethrust latter became emergent as it uplifted the backthrust to the surface. There was relatively more faulting and deformation of the lower unit then in the previous models, resulting in the absence of an antiformal duplex next to the moving wall.

2.7. Discussion

In general, the study showed that all simulations with thin, and thus effectively strong, décollements were dominated by forethrusting. The presence of a weak cover sequence allowed for more deformation in the upper unit relative to the lower unit, and an increase in the formation of popup structures in the upper unit (MS021, Figure 2.6). The simulation with a thick décollement and weak cover sequence (MS021c, Figure 2.7) was very similar to the previous model (Figure 2.6), with more forethrusting in the upper unit and the development of a steeper wedge. The final model, MS039 (Figure 2.8), with strong upper and lower units and a thick décollement, allowed for deformation in both the upper

and lower units, and the thick décollement allowed for enhanced decoupling that created

triangle zones. Unlike the analog models of Couzens-Shultz et al (2003) the strength of the

décollement alone did not seem to control the resistance to forward propagation. Instead,

the strength of the upper unit above the upper décollement has a strong influence on

vergence of frontal faults; weak cover sequences were easily thrust over the foreland, while

stronger cover sequences, when coupled with a thick, weak décollement, were able to

decouple and over thrust the wedge, towards the hinterland, forming a triangle zone. These

triangle zones only developed after a deforming wedge had been built through a series of

forethrusts, suggesting that the differential loading of the strata was necessary to create a

triangle zone under the foreland.

The relatively low internal fiction coefficient used in these models (0.3) affects the

takeoff angle of the faults, but not their distribution. A lower coefficient of friction will

affect the slope of the Coulomb failure envelope, and therefore cause theta, the angle of the

fault with respect to the minimum principal stress, to increase. Most of the takeoff angles of

the simulation faults are correspondingly greater then a predicted 30 degrees. However,

we argue that the décollement strength (sliding friction) will be more important to the

distribution of faults and triangle zones, since the basal friction controls the taper of the

wedge. A low taper is more likely to allow backthrusting since there is less work needed

than in a wedge with a high taper.

2.7.1. Fault Evolution

The study demonstrates that the initiation and development of faults in simulated

fold and thrust belts are quite complicated. Figure 2.9 shows the activity along a fault in

simulation MS021c (Figure 2.7), where fault 1 initiates at the surface, and propagates

down, rather than propagating from the basal décollement (Figure 2.9a, b). This behavior

also has been described by Hardy et al (2009). The fault initiated as a frontal forethrust at

an angle of 37°, but as deformation continued, the fault progressively elongated along the

upper décollement even as the ramps were uplifted, until a second fault formed in front,

propagating from the surface to the upper décollement (Figure 2.9e). Eventually fault 2

linked with the lower ramp of fault 1, creating a stair-step geometry that resulted from a

frontal thrust propagating back into the hinterland and linking with another fault, rather

than propagating from the hinterland to the foreland (Figure 2.9f). Fault 1 was periodically

reactivated behind fault 2, indicating that while the sequence was usually a forward

breaking sequence, reactivation of older structures also occurs (Figure 2.9g, h). Also, once

the moving wall reached the lower part of fault 1, a new blind fault formed in front of it,

linking up to the fault 2 and causing duplexing next to the moving wall (Figure 2.9h). These

examples indicated a complex relationship between the formation of new frontal thrusts,

the linkage with older thrusts, and fault rotation, ultimately forming long stair-stepping

thrust faults.

Within this fault sequence, slip occurs along forethrusts only, and does not include

popup structures. In other simulations, such as MS021 (Figure 2.6) many of the faults

within the cover sequence initiate as popup structures. These pop-up structures are similar

to those observed in analog models where the basal detachment is weak (e.g., Bonini, 2001;

Figure 2.1h, j). Popups can also occur in nature, generally when the décollement is

composed of salt (Stockmal et al, 2007). The backthrusts in the popup structures

accumulate relatively little slip compared to the forethrust, where all subsequent motion
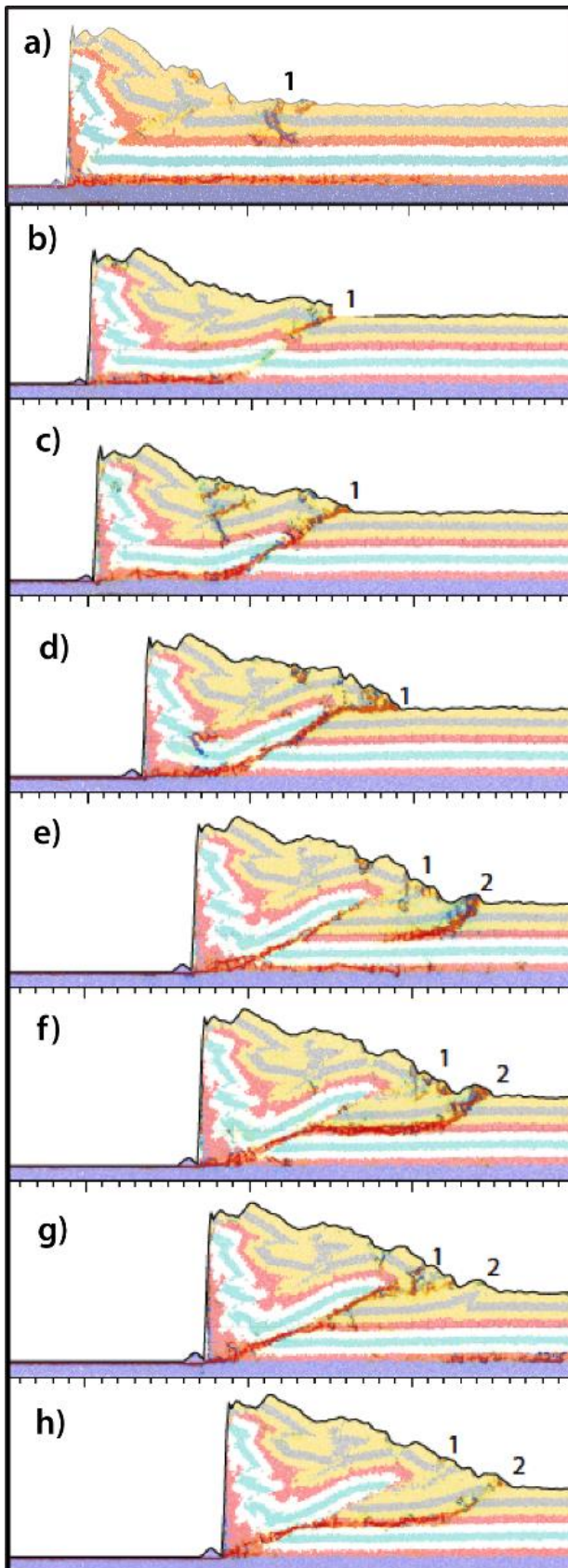
occurs. The popup structures tend to amalgamate into thrust sheets (Figure 2.6c, Fault 5), although they are still visible in the distortion plots since we plot the total strain accumulated in the simulation. Stockmal et al (2007) noted similar popup structures in their FEM models, and that these popup structures were lost with the addition of syntectonic sedimentation and erosion, processes that are not present in our simulations.

Figure 2.9 - Fault evolution. Snapshots of the incremental distortional strain (colorbar in previous figures) for a fault in simulation MS021c. Image shows initiation of Fault 1, breaking from the surface down to the upper décollement. b) Image shows Fault 1 breaks to the lower décollement. c) Image shows Fault 1 forming a thrust fl at at the surface. d) Image shows Fault 2 breaking in front of Fault 1. e) Image shows Fault 2 linking up with the lower portion of Fault 1. f) Image shows reactivation of Fault 1. g) Image shows deformation returns to the Fault 2.

2.7.2. Layer parallel shortening

In addition, all of the simulations showed a large degree of layer parallel shortening throughout the simulations. Up to 3 km occurred near the wall, prior to any faulting, amounting to about 10 percent of the total shortening as additional horizontal shortening occurred throughout the simulation. Similar values of layer parallel shortening have been observed in the field at the front of fold and thrust belts; Sans et al (2003) measured 16-25 % shortening caused by penetrative strain in the external part of the Southern Pyrenees fold and thrust belt, while Woodward et al (1986) measured around 5% shortening in the Appalachian valley and ridge province, and Mitra (1994) measured 9-35 % shortening in the Idaho-Utah-Wyoming fold and thrust belt. Layer parallel shortening has also been measured in analog experiments; Nilforoushan et al (2008) measured 5-12 % volume decrease in their sandbox models of fold and thrust belts. In our simulations the shortening is a result of particle reorganization, but it represents processes seen in the field, such as pressure solution and penetrative strain within thrust sheets.

2.7.3. Comparison with central Appalachians

The Appalachian cross-sections (Figure 2.1c, d) are characterized by forethrusting, with no backthrusts or triangle zones present. Figure 2.1d contains a buried duplex verging towards the northwest, with faults propagating both from a basal décollement and an upper décollement at about 2 km. This is similar to simulation MS001 where a duplex system is built with faults connecting to the basal décollement (Figure 2.5, faults 7 and 8) and from the upper décollement (Figure 2.6, faults 6 and 9). The duplex here is emergent however, rather than the buried Appalachian duplex. The cross-section in Figure 2.1c is

from a different part of the Appalachians, and is characterized by two different levels of deformation. The lower carbonate section (shaded) deforms as long buried sheets that thrust over top each other. Above these thrust sheets, the upper stratigraphic units (white) are deformed by a second set of forethrust, generally more closely spaced together, and not connected to deformation at depth. Simulations MS021 (Figure 2.6) and MS021c (Figure 2.7) behave similarly, with distinct deformation patterns in the lower and upper units. The lower unit tends to deform in long thrust sheets, aside from the duplex forced by the moving wall. The upper unit deforms mainly through popup structures in simulation MS021 (Figure 2.6d) and forethrusts in simulation MS021c (Figure 2.7c). The thicker décollement unit in the latter simulation allows for more decoupling between upper and lower units, and favors forethrusting of the upper unit, similar to the central Appalachians.

2.7.4. Comparison with Canadian Cordillera (Alberta) and Papua New Guinea

Within our results, the creation of a mechanically weak upper unit, defined as a cover sequence, does not support the formation of backthrusts and triangle zones within the fold and thrust belt, as hypothesized by Couzens and Wiltschko (1996). Instead, triangle zones form in the model with the strongest upper and lower units, when separated by thick and weak décollement horizons. This indicates that the strength contrast is important in the creation of triangle zones, however, the contrast between the upper and lower units and the décollements, rather then the lower vs. the upper unit. We note that the generalized stratigraphic column for Alberta (Stockmal et al, 2001) indicates that the upper décollement occurs in the weak Bearpaw Formation (Fm), which is composed of marine shale (Figure 2.10). The overlying unit, the St. Mary River Fm, is made up of sandstone and

shale, and is relatively significantly stronger then the Bearpaw Fm. It also is very similar in

strength to the Belly River Group that underlies the Bearpaw Fm (Stockmal et al, 2001).

Therefore, it is possible that this relationship between the relative strengths of the

décollement horizon and the bracketing units controlled the formation of frontal triangle

zones in Alberta, rather then the presence of weak units within the upper portion of the

stratigraphic column.

The cross-sections in Figure 2.1e, f, and g show triangle zones from Alberta, Canada

and Papua New Guinea, respectively. They all show the triangle zones forming a long thin

wedge into the foreland along an upper décollement surface. The backthrusts are concave

upwards. There is a vertical duplex in Southern Alberta, contrasting with the more

horizontally stacked duplex in Papua New Guinea. Simulation MS039 (Figure 2.8) is similar

to the two cross-sections, with the two triangles zones forming a wedge underneath the

foreland at the level of the upper décollement. Unlike the cross-sections, the backthrusts

are more convex upwards then concave, which may be due to the effect of the low internal

coefficient of friction on the takeoff angle of the faults, as discussed previously. The duplex

in simulation MS039 is similar to that of Papua New Guinea, with more of a horizontal

stacking rather then the vertical duplex of Southern Alberta. A popup structure forms at the

basal décollement underneath the second triangle zone, rather then a duplex (Figure 2.8d).

However, a similar popup structure beneath a triangle zone is seen in Lawton et al, (1996)

in central Alberta (Figure 2.1f). Therefore, although our stratigraphy is simplified relative

to nature, we still reproduce similar frontal structures.

In addition, the cross-section in Figure 2.1e shows two subsequent triangle zones; the first occurs behind the frontal anticline, which was uplifted within the deforming wedge and mostly eroded, and the second triangle zone occurs in front of the frontal anticline and extends underneath the foreland basin. This geometry is very similar to Figure 2.8d, the final configuration of our simulation MS039, which shows sequential stacked triangle zones forming at the front of the fold and thrust belt. This supports the belief that triangle zones are generally active at the front of a fold and thrust belt where new material is entrained, and subsequently, are uplifted and incorporated into the thrust belt, where they are usually not preserved due to erosion. As our simulations do not include erosion, the initial triangle zones are still visible (Figure 2.8d).

Triangle zones do not appear to form until a significant wedge has developed, indicating that some amount of differential loading and resulting stress reorientation is necessary to form a triangle zone. In our study, the wedge formed by sequential forethrusting, but the same effect might be generated by syntectonic sedimentation, which would preferentially load the frontal region of the foreland basin relative to more distal areas. Syntectonic sedimentation and erosion, as well as thinning of beds towards the foreland, are other parameters that might be important in the creation of frontal triangle zones, and will be considered in later simulations.
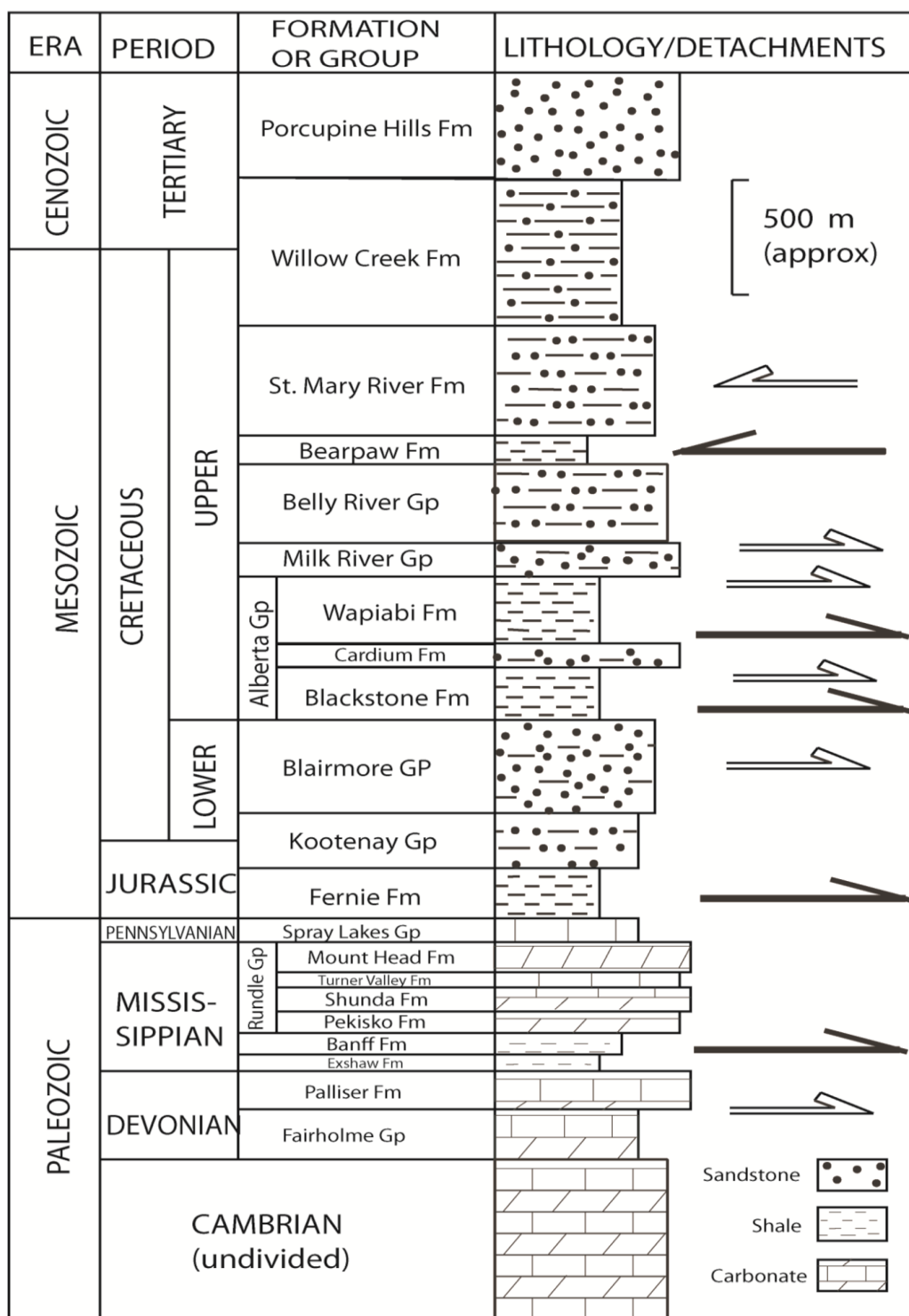
Figure 2.10 - Stratigraphic column of Alberta, Canada from Stockmal et al. (2001). Main upper décollement (direction of thrust indicated by arrows) occurs in the Bearpaw Formation, which is relatively weaker then the fl anking St. Mary River and Belly River formations.

2.7.5. Variability along strike

Our simulations are all two-dimensional, but they can be used to explore effects of along-strike changes in stratigraphic properties in a three dimensional thrust front (Figure 2.11). For example, the thinning out of the upper décollement horizon along strike, or a facies transition into a more competent material would represent a transition from simulation MS039, showing frontal triangle zones, to MS001 or MS004, simulations with the same upper and lower unit strength, but a thinner décollements, decreasing the ability of the upper unit to decouple from the lower unit. In the lower section of Figure 2.11, the décollement thickness does not change, but the cover sequence undergoes a transition from a more competent unit to a weaker, possibly more shaley, unit, represented by the transition from simulation MS039 to MS021c. The decrease in strength in the upper unit prevents it from coherently overriding the deforming wedge, and instead the unit deforms through forethrusting and the formation of dual verging popup structures. Therefore, the strength and thickness of the décollement and the upper unit are important parameters in dictating the formation of frontal structures, and a thick décollement horizon combined with a strong upper unit is needed to promote the formation of frontal triangle zones. Changes in these horizons will result in changes in the frontal structures along strike in a thrust front.
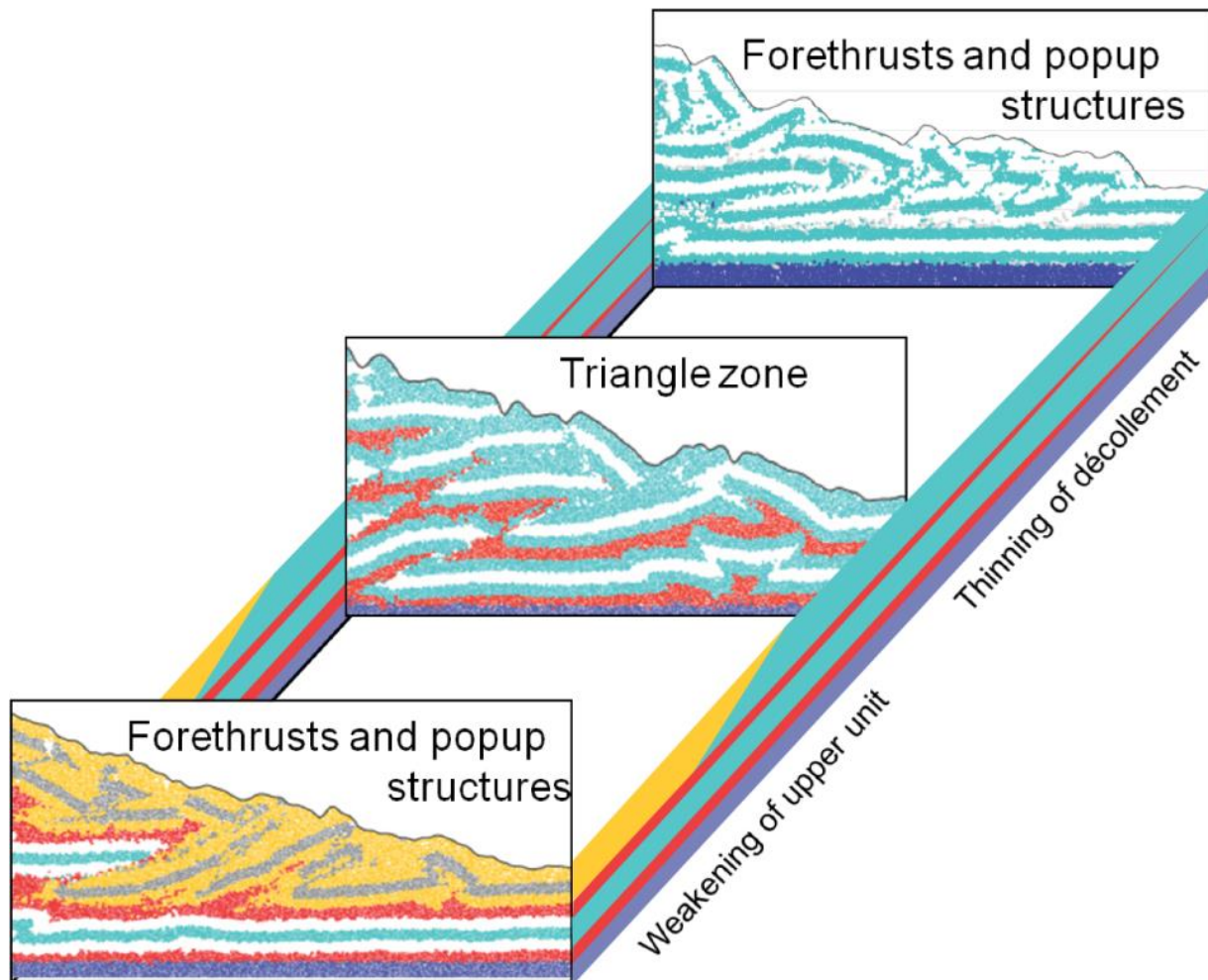
Figure 2.11 – Triangle zone formation. Triangle zones (middle panel) can form when there is a thick, relatively weak unit between two stronger units. If the upper unit is too weak (lower panel) then forethrusts and popup structures dominate in the upper unit and the lower unit is relatively undeformed. Alternatively, if the décollement becomes too thin (upper panel) there is not enough decoupling to create a triangle zone, and both units are thrust toward the foreland.

2.8. Conclusions

Our simulations support the idea that mechanical stratigraphy plays an important role in the types of frontal structures that form in different fold and thrust belts. In particular, one method for the formation of triangle zones has been shown to depend on a

relatively large strength contrast between the upper décollement and surrounding units, which allows the upper unit to decouple and deform through backthrusting, rather then by creating popup structures with active forethrusts that overshadow any slip on the conjugate backthrust. The overall thickness of both the sediments above the basal décollement and the thickness of the décollements themselves also was important in the creation of frontal backthrusts, and will be further explained in future simulations. Triangle zones also appear to need the buildup of a deforming wedge to form. Wedge development can occur through initial forethrusts or possibly through syntectonic sedimentation. Therefore, mountain belts where triangle zones are not found may not have the correct stratigraphy, or the décollement horizons may be too thin to allow for enough decoupling between the lower and upper units to form triangle zones. However, a weak cover sequence in our simulations produced mainly forethrusts, and was not a contributing parameter for the formation of frontal triangle zones.

<div style="text-align: right">

Chapter 3

</div>

Influence of mobile shale on thrust faults: Insights from discrete element simulations

3.1. Abstract

We study the effects of sedimentary loading of a mobile shale substrate, using two-dimensional discrete element modeling. We develop an updip extensional zone connected at depth to a downdip contractional zone, allowing us to study the formation of gravity driven fold and thrust belts, and the evolution of décollements within this system. We compare out models to the Niger Delta type locale for shale tectonics. In general, most seismic interpretations of the Niger Delta include décollement(s) at the top of the mobile shale unit, but exact locations vary depending on area of investigation. Our models, particularly ones with mobile shale thicker then 2 km, show more diffuse décollements, spanning the width of the mobile shale unit, which propagate out in front of the syntectonic sediment wedge and connect normal faults in the extensional zone with toe thrusts in the contractional zone. We also look at the distributions of stress and strain within out models, plotting the distributions of $\sigma 1$ and relating that to the vergence of thrust faults developed

in our models. We quantify the amount of strain in different sections of the models, showing that extension is much greater then compression in the fold and thrust belt(s) alone, and that there is distributed compression throughout the model, including in front of the fold and thrust belt.

3.2. Introduction

3.2.1. Deepwater fold and thrust belts

In many gravity driven deepwater fold and thrusts belts, such as the Niger Delta, Baram Delta, Port Isabel Fold Belt in the Gulf of Mexico, and Veracruz State fold and thrust belt in the Gulf of Mexico, stratigraphy is characterized by weak shales that form an underlying substrate for the system, and overlying sand and shale deltaic formations (Morley, 2003; Corredor et al, 2005; Alzaga-Ruiz, et al, 2009; Weiner et al, 2010; Morley et al, 2011). Deformation in these systems consists of extension in the shallow near shelf areas (delta) and contraction in deepwater, basinward, areas. Hydrocarbon basins containing mobile shale substrates have often been compared with salt systems (Morley and Guerin, 1996; Wu and Bally, 2000) but there are still questions about how mobile shale systems deform.

By definition, mobile shales are zones of overpressured mud or shale that deform ductily. Overpressures develop in sediments due to rapid burial beneath low permeability units, and hydrocarbon maturation (Morley and Guerin, 1996). Mobile shale is characterized by low seismic velocity, low density, and seismic transparency, making them

difficult to interpret and obscuring fault traces. Within mobile shales, ductile shale layers can occur at multiple levels, and mobility can change over time (Weiner et al, 2010).

Deformation in deep water fold and thrust belts is driven by updip extension, which is due to deltaic sedimentary loading. The rate of updip extension and sediment loading affects the rate of contraction in the fold and thrust belt. In-between the zones of extension and contraction, deformation is transferred through the mobile substrate, although the mode of propagation is debated; diffuse or forming a discrete décollement (Kruger and Grant, 2012). We suggest the thickness of the mobile substrate as well as the overlying unit, may affect the type of folds formed in the contractional zone and the vergence and spacing of the thrust faults. There are relatively more backthrusts in parts of mobile shale systems such as the Niger Delta, than occur in most fold and thrust belts (Bilotti and Shaw, 2005; Corredor et al, 2005). Thrusts changing vergence along strike are also common in these environments, (Kostenko et al, 2008).

We suggest that these characteristics relate to the mechanical properties and behaviors of the system. Our implementation of DEM allows us to explore the causes and controls using forward mechanical modeling. Here, we study the effects of varying thickness and sedimentation rate of a linked extension and contractional system driven by sediment loading in order to understand the influence of mobile shale on deepwater folds and thrusts, and to characterize the evolution of décollements within the system. We then compare our results to the Niger Delta type locale for shale tectonics.

3.2.2. Geologic Background

The Niger Delta is located on the West African continental margin in the Gulf of Guinea (Figure 3.1a). It is one of the largest deltas worldwide, and is considered a type location for shale tectonics (Wu and Bally, 2000). The delta extends about 300 km from the onshore extensional zone to the distal fold and thrust belts, and about 500 km along strike. The fold and thrust belts form two lobes, each about 200 km wide, separated by the Charcot Fracture Zone, which is mostly unaffected by thrusting (Morley et al, 2011). The Niger Delta is a major-hydrocarbon region that contains an abundance of mobile shale, which forms a weak ductile substrate (Figure 3.1b). The stratigraphy of the region is made up of Cretaceous to Holocene marine and deltaic deposits deposited directly upon oceanic crust (Doust and Omatsola, 1990; Wu and Bally, 2000). The major mobile shale unit in the Niger Delta is the Tertiary Akata formation. The Akata formation has low seismic velocities and is seismically transparent, suggesting it is regionally overpressured (Bilotti and Shaw, 2005; Corredor et al, 2005). The Akata formation ranges in thickness from 2 km in the distal areas of the delta to 7 km thick under the continental shelf. Overlying the Akata formation is the Agbada Formation, consisting of a deltaic succession of sands and shales. It represents the delta front, delta topset, and fluviodeltaic environments (Corredor et al, 2005). At about the same time of initiation of deformation in the outer fold and thrust belt, about 4 km of Agbada paralic siliciclastics was deposited on top of the Akata shale in the distal region, influencing the outer fold and thrust belt (Kruger and Grant, 2012). Onshore there is a third tectononstratigraphic unit, the Benin Formation, that is composed of

alluvial and coastal plain deposits, and is up to 2 km thick (Corredor et al, 2005). This unit is not present in the region of this study.

The Niger Delta is a classic example of a linked updip extensional and downdip contractional systems (Wu and Bally, 2000; Kostenko et al, 2008; Weiner et al, 2010). Gravity-driven spreading of the delta creates a broad sedimentary wedge above an oceanward dipping detachment. Loading occurs through sedimentation on the continental shelf, which drives the gravitational collapse of the delta. The updip extensional faults are interpreted to be linked at depth to the down dip contractional fold and thrust belts at the delta toe through several interpreted detachments localized in the Akata Fm. (Wu and Bally, 2000; Corredor et al, 2005). There are five main structural provinces defined for the Niger Delta (Corredor et al, 2005). Going seaward from the continent, (right to left in Figure 3.1b) these provinces are; 1) a proximal extensional province consisting of both regional (seaward dipping) and counter-regional (landward dipping) normal faults, 2) a mud-diapir zone; 3) an inner fold and thrust belt consisting of predominantly imbricate forethrusts; 4) a transitional zone containing large, broad, detachment folds above thickened Tertiary marine shale; and 5) an outer fold and thrust belt consisting of both forethrusts and backthrusts and their associated folds (Corredor et al, 2005; Maloney et al 2010) (Figure 3.1a & b).

Previous workers have interpreted décollements within the mobile substrate in the Niger Delta system, which connect updip extension along normal faults to downdip contraction accommodated within the frontal fold and thrust belts (Bilotti and Shaw, 2005; Corredor et al, 2005; Briggs et al, 2006; Kostenko et al, 2008, Maloney et al, 2010; Weiner

et al, 2010; Kruger and Grant, 2012). Most of the deepwater thrust faults are listric, with steeper, more planar geometries in the upper part of the faults, which become subhorizontal at depth near the top of the mobile shale. The listric geometry of these thrust faults and their relationship with the mobile shale at their bases are strongly suggestive of the presence of a décollement surface (Briggs et al, 2006).These décollements have been interpreted at various levels and positions within the mobile shale in different parts of the Delta. Briggs et al (2006) interprets two main décollement horizons, one between the Akata and Agbada Formations, and one at the top of the Akata formation. In some locations, they report another décollement surface within the Akata formation. Corredor et al (2005) and Maloney (2010) describe a main décollement surface occurring within the Akata formation. Wiener et al (2010) identifies the décollement surface occurring at the top of the mobile shale unit, although he states that the décollement may occur on a specific horizon across which there is a strong mechanical contrast, or within an interval of weak shale. Benesh et al (2014) also interpret the primary basal detachment at the top of the Akata formation. In general, most interpretations include décollement(s) at the top of the Akata formation, but specifics depend on the particular area of investigation. Few, if any reflections appear to correlate with a décollement surface itself, and most interpretations locate the décollement where the listric toe thrusts become subhorizontal.

However, still to be resolved is the thickness of the décollement layer(s), and over what region deformation occurs, i.e. along a plane or distributed throughout the seismically transparent zone. In addition, how is deformation transferred from the extensional to the compressional regime? Kruger and Grant (2012) state that deformation in the mobile shale

is distributed throughout the mobile shale under the inner fold and thrust belt, and then transfers onto more discrete décollement horizons near the outer fold and thrust belt. Whether this localization is due to a change in mechanical properties of the shale, or related to the thinning of the shale oceanward is unclear.

Most thrust faults in the southern delta lobe verge toward the foreland, whereas the outer fold and thrust belt in the northern lobe includes some backthrusts. In some locations, the vergence of a single thrust fault changes along strike (Kostenko et al, 2008). According to Corredor et al (2005) and Bilotti and Shaw (2005), the backthusts occur in places where the bathymetric slope, basal detachment, and maximum horizontal stress directions are inferred to be essentially parallel to one another, yielding an equal preference for fore- and backthrusts. With the low taper of the Niger delta wedge, and the inferred low basal friction within the mobile shale, the work needed to create a backthrust is approximately the same as that needed to create a forethrust and thus, both vergences should be equally likely. We test this idea by looking at the stress fields in out numerical DEM models.

Figure 3.1 - a) Map view of the Niger Delta. The Niger Delta is located on the western coast of Africa, divided into five structural zones: the extensional zone in dark blue, the mud diapir zone in light blue, the inner fold and thrust belt in yellow, the detachment zone in pink, and the outer fold and thrust belt in green. A to A' marks the line of the cross-section in b) (modified from Kostenko et al 2008). b) Interpreted seismic cross-section A-A' through the Niger delta showing the Akata Fm. (mobile shale) in green, and the overlying Agbada formation with horizons. Interpreted faults shown in black (modified from Kostenko et al, 2008). (See figure on next page)

b)

A ← ← → → A'

← Outer Fold and Thrust Belt → ← Transitional Detachment Fold Zone → ← Inner Fold and Thrust Belt → ← Diapiric Belt → ← Extensional Province →

Continental Slope

Mud Diapir Zone

Highly Imbricated Agbada and Younger Sequences

5 km

10

Oceanic Basement

Mobile Shale - Akata Fm

0   10   20 km

a)

100 km

N

5°00'N

Detachment Province

Inner Fold and Thrust Belt

Outer Fold and Thrust Belt

4°00'N

Mud-Diapir Province

A'

Extensional Province

3°00'N

Abyssal Plain

A

3°00'E   4°00'E   5°00'E   6°00'E   7°00'E   8°00'E

3.2.3. Numerical simulations

Numerical simulations have provided important insight into the evolution of deltas above mobile shales (Morency et al, 2007; Albertz et al, 2010; Ings and Beaumont, 2010) and the evolution of fold and thrust belts (Sassi and Faure, 1996; Burbidge and Braun, 2002; Strayer et al, 2004; Benesh et al, 2007; Sanz et al, 2007; Stockmal et al, 2007). Interest in gravitational systems has been focused on the generation of pore pressure within sub-delta shales, and the threshold at which such shales become mobile. Albertz et al (2010) investigated the conditions for failure and gravitational spreading of a delta overlying mobile shale. They found that wide margins (~400 km wide) similar to the Niger Delta, required pore-fluid pressures of 95-99 % of the overburden in order to fail, though there was a dependence on the intrinsic strength of the modeled sediments. Ings and Beaumont (2010) expanded on Albertz et al's (2010) models, using coupled fluid and mechanical finite element method (FEM) models. They concluded that for gravitational instability to occur, the basin must be underlain by a décollement layer composed of weak sediments. Fluid pressures along that horizon must be 90-95 % of lithostatic pressure to cause the weak shale to fail and mobilize. Due to the continuous nature of the FEM models, only shear zones develop, rather than discrete faults. Deformation in the mobile shale therefore occurred as slug flow in front of the extensional domain, and shear flow throughout the unit in the compressional domain. In addition, no backthrusts developed in the models, even in the case of a horizontal basement.

Gravitationally collapsing deltas have also been simulated using numerical models. In analog models that use silicone putty to represent mobile shale (McClay et al, 2003) the

deformation in the mobile shale is similar to the deformation in numerical models (Ings and Beaumont, 2010). The mobile shale deforms by slug flow, where a large shale bulge develops at the distal end of the extensional zone, landward of the fold and thrust belt(s). Shale diapirs also have been interpreted in seismic sections, near the inner fold and thrust belt (Corredor et al, 2005). In contrast, analog models that use injected compressed air to simulate pore fluids in sandbox models have décollements form as very fine shear bands (Mourgues and Cobbold, 2006; Mourgues et al, 2009). As the fluid pressures increase, the décollement zone thickens and the fine sand flows ductily. Sand volcanos are also formed as the sand is highly overpressured (Mourgues et al, 2009). Similar to the analog and numerical models, the thickness of the mobile shale might therefore affect the deformation in the overlying unit.

Here, we use a 2D discrete element method (DEM), to simulate the Niger delta linked extensional - contractional system driven by sediment loading. We use these models to investigate the formation and evolution of the toe structures and their relationship with the underlying mobile shale. We focus on the evolution of the fold and thrust belts, rather than the pore pressure generation in the mobile shale. Although we don't include fluids and overpressures in our models, the mechanical effects of a very weak mobile layer overlain by a stronger, pre-delta layer can be evaluated in response to sediment loading. Therefore, the effect of pore fluid pressures was modeled by modifying the properties of the mobile shale unit to be weak and deform ductily. This does mean that the mobile shale is considered overpressured throughout the simulations, and is not altered. The discrete nature of DEM models allows us to better investigate the nature of the deformation in the

simulation, in particular, the degree of localization within the system, resolving the occurrence of discrete faults or distributed shear. In addition, we explore the role of stress state on the deformation field.

We use an initial two layer stratigraphy, representing the Akata and Agbada Fms., and add sediments to the upslope region over time. We vary the thickness of each layer, as well as the sedimentation rate, to determine the effects on the formation of the fold and thrust belts(s), fault vergence and the nature of basal slip and décollements in such systems. We also quantify the amounts of extension and contraction in the models, to determine how they compare with each other.

Numerical simulations have provided important insight into the evolution of deltas above mobile shales (Morency et al, 2007; Albertz et al, 2010; Ings and Beaumont, 2010). Interest has been focused on the generation of pore pressure within sub-delta shales, and the threshold at which such shales become mobile. Albertz et al (2010) investigated the conditions for failure and gravitational spreading of a delta overlying mobile shale. They found that wide margins (~400 km) similar to the Niger Delta, required pore-fluid pressures of 95-99 % of the overburden in order to fail, though there was a dependence on the intrinsic strength of the modeled sediments. Ings and Beaumont (2010) expanded on Albertz et al's (2010) models, using coupled fluid and mechanical finite element method (FEM) models. They concluded that for gravitational instability to occur, the basin must be underlain by a décollement layer composed of weak sediments. Fluid pressures along that horizon must be 90-95 % of lithostatic pressure to cause the weak shale to fail and mobilize. Due to the continuous nature of the FEM models, only shear zones develop, rather

than discrete faults. Deformation in the mobile shale therefore occurred as slug flow in front of the extensional domain, and shear flow throughout the unit in the compressional domain. In addition, no backthrusts developed in the models, even in the case of a horizontal basement.

Mobile shale is often seen in analog models (McClay et al, 2003) and previous numerical models (Ings and Beaumont, 2010) to deform by slug flow, where a large shale bulge develops at the distal end of the extensional zone, landward of the fold and thrust belt(s). Shale diapirs also have been interpreted in seismic sections, near the inner fold and thrust belt (Corredor et al, 2005). The thickness of this shale bulge might therefore affect the deformation in the overlying unit.

Here, we use a 2D discrete element method (DEM) to simulate the Niger delta linked extensional - contractional system driven by sediment loading. We use these models to investigate the formation and evolution of the toe structures and their relationship with the underlying mobile shale. We focus on the evolution of the fold and thrust belts, rather than the pore pressure generation in the mobile shale. Although we don't include fluids and overpressures in our models, the mechanical effects of a very weak mobile layer overlain by a stronger, pre-delta layer can be evaluated in response to sediment loading. The discrete nature of DEM models allows us to better investigate the nature of the deformation in the simulation, in particular, the degree of localization within the system, resolving the occurrence of discrete faults or distributed shear. In addition, we explore the role of stress state on the deformation field.

We use an initial two layer stratigraphy, representing the Akata and Agbada Fms., and add sediments to the upslope region over time. We vary the thickness of each layer, as well as the sedimentation rate, to determine the effects on the formation of the fold and thrust belts(s), fault vergence and the nature of basal slip and décollements in such systems. We also quantify the amounts of extension and contraction in the models, to determine how they compare with each other.

3.3. Discrete Element Method

The discrete element method (DEM) is a numerical approach based on the interaction of discrete particles using the laws of contact physics. It is an effective tool for simulating elastic-frictional deformation in materials subject to brittle deformation and frictional slip. The original code (TRUBAL) was developed by Cundall and Strack (1979) and was adapted (and renamed RICEBAL) as summarized by Morgan and Boettcher (1999). The method has been used to model shear zones and micromechanics (Morgan and Boettcher, 1999; Guo and Morgan, 2004) as well as larger structures such as accretionary prisms and fold and thrust belts (Burbidge and Braun, 2002; Naylor et al, 2005; Dean et al, 2013) and salt tectonics (Maxwell, 2009).

DEM uses a time-stepping finite difference approach to solve Newton's equations of motion for all particles in the system; solving

$$F_p = m_p * \ddot{x}_p \qquad \text{(Equation 1)}$$

$$M_p = I_p * \ddot{\theta}_p \qquad \text{(Equation 2)}$$

where F_p and M_p are the net force and net moment acting on each particle, m_p and I_p are the

mass and moment of inertia, and $\ddot{x}_p$ and $\ddot{\theta}_p$ are the linear and angular accelerations of the

particles. Gravitational forces, interparticle contact forces, and external forces prescribed at

the boundaries are summed for each particle and substituted into equations (1) and (2)

which are solved for particle velocities and displacements (Figure 2.2b). As particles are

displaced, they interact with adjacent particles. The calculation of contact forces is

alternated with calculation of particle displacements which changes the net forces acting

on each particle. The process repeats until the whole assemblage of particles is in

equilibrium (e.g., Morgan and McGovern, 2005). The interparticle contact forces obey

Hertz-Mindlin contact theory (nonlinear), where cohesionless particles respond elastically

to normal forces, and resist frictional sliding from shear forces (Figure 2.2a). These forces

are given by

$$f_n = k_n\, \delta_n \qquad\qquad\qquad\qquad\qquad \text{(Equation 3)}$$

$$f_s = k_s\, \delta_s \qquad\qquad\qquad\qquad\qquad \text{(Equation 4)}$$

where f_n and f_s are the normal and shear contact forces, δ_n and δ_s are the relative distance

between the two particles perpendicular to the contact, and k_n and k_s are the normal and

shear stiffness. The stiffnesses are nonlinear and a function of the contact area (Johnson,

1985). The shear force is limited by the interparticle coefficient of friction, so that when the

shear forces are large enough, sliding occurs between particles. If slip is highly localized,

faults can form. Cohesion is simulated by adding bonds between particles to create more

realistic rock properties (Guo and Morgan, 2004). Bonds introduce interparticle tensile and

cohesive forces (Figure 2.2c); once these bond strengths are exceeded, in either tension or

shear, the bond breaks and the particles are free to displace relative to each other, creating faults.

3.4. Numerical Material Properties

In DEM materials, the bulk rheology of the granular material is a product of the particle interactions, and can vary with deformation. Properties such as friction, density, and bond strengths and moduli are assigned at the particle scale. The bulk properties of an assemblage must be constrained through calibration tests (Figure 3.3a, b). Accordingly, we obtained the mechanical properties of our materials by performing shear box tests on the numerical assemblages for specific combinations of particle friction, density and bond strengths. The resulting coefficients of internal friction and cohesions were compared with published values for mobile shale and salt used by Albertz et al (2010), Maxwell (2009), and Ings and Beaumont (2010) to ensure that the models represent realistic properties of the Niger Delta formations (Figure 3.3, Table 1).

The mobile shales underlying the delta are adequately modeled using a viscous rheology (Cohen and McClay, 1996). The frictional nature of DEM particles is an imperfect approximation. Therefore, they are represented as very weak non-cohesive particles with low densities of 1300 kg/m^3 and 1500 kg/m^3 (corrected for submersion by subtracting a water density of 1000 kg/m^3). Although the particles are frictional, the unbonded particles will respond to stress by moving to areas of low stress, i.e. out from beneath a sediment wedge. The bulk motion of the particles therefore flows away from the extensional zone, such that the bulk assemblage behaves in a ductile way. Apparent viscosity, which is time

dependent, is introduced in our DEM materials due to time dependent numerical parameters such as viscous damping of particle motions (Morgan and McGovern, 2005). To characterize the apparent viscosity of this mobile shale unit, we performed a series of shear box tests on the material, as described above, using a range of wall velocities to control the shear strain rate. The plotted shear stress and shear strain rates show that at a strain rate of $5x10^{-2}$ to $5x10^1$, the mobile shale particles has an approximate viscosity of about $4x10^8$ Pa*s to $3x10^9$ Pa*s (Figure 3.4), increasing with depth (which is indicated by increasing the confining pressure). Our particles display a nonlinear trend, similar to many plastic fluids (Menard, 2008). Decreasing the thickness of mobile shale (5 km in model 1.7, 2 km in model 2.6) increases the strain rate and the shear stress in the material, and decreases the viscosity. For scaling purposes, we have approximated the viscosity as linear, at roughly 10^8 Pa*s.

This apparent viscosity of our unbonded DEM materials is much less than the viscosities of natural mobile shales, which are poorly known and assumed to have similar viscosities as salt (10^{18}-10^{20} Pa*s; Albertz, 2009; Ings and Beaumont, 2010). However, the low friction ($\mu < 0.1$) and cohesion (C < 5 MPa) can cause deformation in this material to be broadly distributed, consistent with viscous flow rather than localized brittle faulting (Maxwell, 2009).

The low apparent viscosity of our numerical material can be compensated for by scaling time in our models. Time must be accounted for explicitly since the simulations are driven by sedimentary loading, which is a time dependent process. Thus, we can directly relate shear stress and sedimentation rate. Assuming that the shear stresses in the models

and in nature are the same (Figure 3.4), we can balance equations for model and natural shear stress, which we assume should match, as follows:

$$1 = \frac{\tau_{model}}{\tau_{nature}} = \frac{\gamma_{model} * \eta_{model}}{\gamma_{nature} * \eta_{nature}}$$
(Equation 5)

where τ represents shear stress, γ is shear strain rate, and η defines viscosity. Thus, the viscosity ratio will be proportional to the inverse ratio of shear strain rate:

$$\frac{\gamma_{model}}{\gamma_{nature}} = \frac{\eta_{nature}}{\eta_{model}} = \frac{10^8}{10^8} = 10^0$$
(Equation 6)

As viscosity in the models is lower then in nature, strain rate should be correspondingly higher. For example, a natural viscosity of 10^{18} Pa*s and a model viscosity of 10^8 Pa*s results in a viscosity ratio of 10^{10}. Therefore the model shear strain rate should be 10^{10} s^{-1} greater than the shear strain rate in natural systems. Considering that sediment loading is responsible for shear deformation within the shale, we can scale time in the models by scaling the natural sedimentation rate of 160 m/Ma by 10^{10}, resulting in sedimentation rate of 0.05 m/s in the models. This higher sedimentation rate, many orders of magnitude larger than in nature, yields approximately the same values of shear stress in the models as occur in the natural system. We argue that the overall structures that develop in our simulations should be representative, especially in the overlying sedimentary rocks that are assumed to have very little time dependence in their rheology (Jaeger and Cook, 1969).
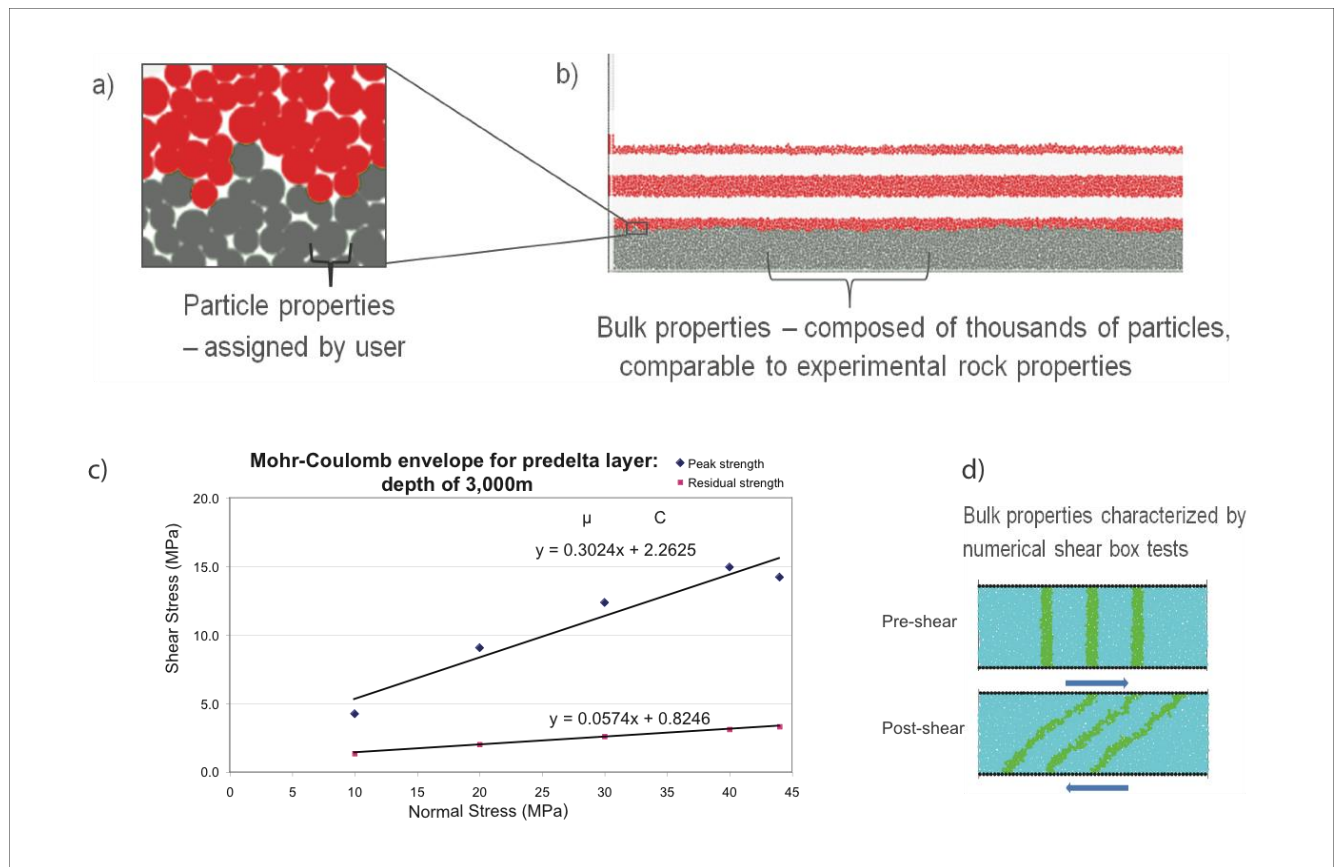
Figure 3.2 - Calibrating DEM simulations. a) Close up of particles in a model. b) Section of a model domain showing pre-loading strata. c) Plot of shear and normal stresses derived from simple shear tests of model materials used here. The peak shear stress (blue diamonds) and an average of the residual strength (pink squares) are plotted vs. the confining stresses for a suite of shear box tests. d) Representative shear box simulation: the top box shows the undeformed state, while the second box shows the simulation after a period of shear strain.
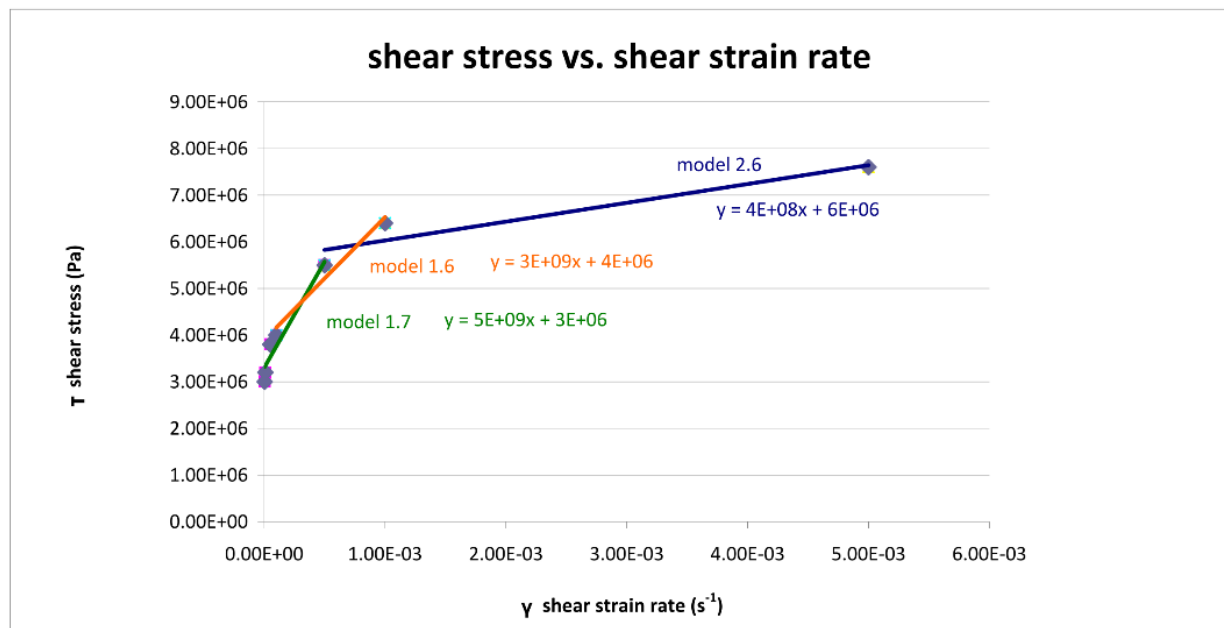
Figure 3.3 - Aparent viscosity of particles. Results of a suite of simple shear tests to determine the apparent viscosity of the unbonded DEM material representing the mobile shale. Shear stress is plotted versus shear strain rate for a suite of experiments at uniform confining pressure, and various strain rates. The slope yields the apparent viscosity of the material (mobile shale unit).
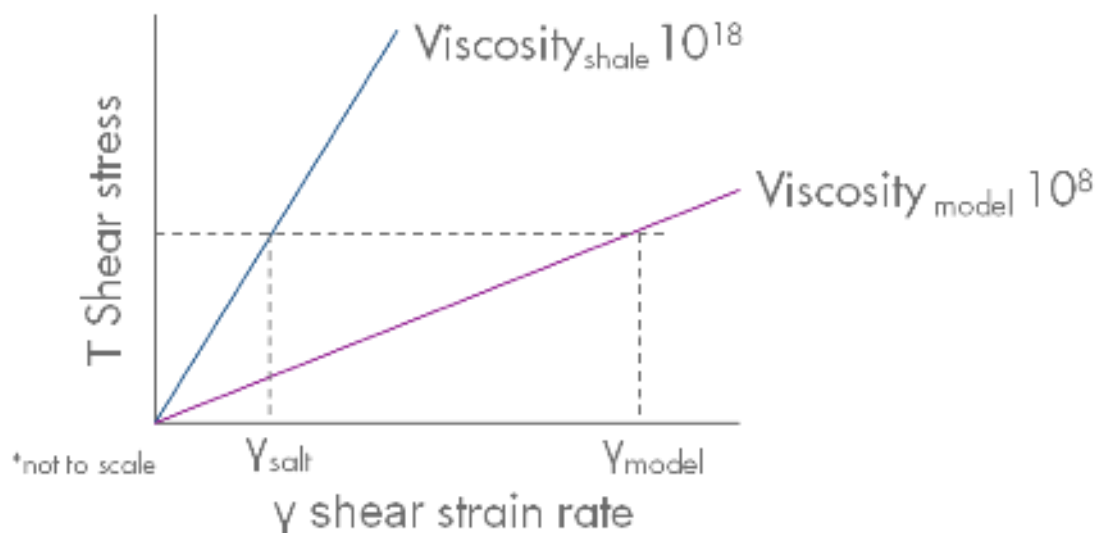
Figure 3.4 - Schematic plot of model versus mobile shale viscosity. To maintain realistic model shear stress, we rescale strain rate, which is controlled by sedimentation rate.

Table 3.1 Particle parameters

	mobile shale unit	predelta unit
density of unit (kg/m^3)	2300	2500
density of water (kg/m^3)	1000	1000
particle coefficient of friction	0.0	0.0
bonds (MPa) — compression	0	40
bonds (MPa) — tension	0	10
results of calibration expts — peak — bulk coefficient of friction	0.05	0.11
results of calibration expts — peak — cohesion (MPa)	0.6	5.6
results of calibration expts — residual — bulk coefficient of friction	0.04	0.05
results of calibration expts — residual — cohesion (MPa)	0.9	0.8

3.5. Experimental Setup

To model the development of linked extensional and compressional systems we define a two to three layer stratigraphic system: first the mobile shale particles are deposited (Figure 3.6), with particle densities of 2,300 kg/m^3, 1,300 kg/m^3 after being corrected for submersion. Secondly, another layer of particles is deposited, with densities of 2,500 kg/m^3 (1,500 kg/m^3). This layer is alternatively colored red and white, in order to better see subsequent deformation. This overlying unit, representing the pre-growth sedimentation part of the Agbada Fm. is referred to as the 'predelta layer' in our models.

We realize the Agbada Fm. is composed of the distal facies of the Niger Delta, and use "predelta" to indicate the strata deposited before the delta was large enough to cause gravitational collapse and downdip contraction. We do not include growth sedimentation in in the distal part of the simulations, but we do change the pre-delta (pre-deformation) thickness in order to observe its effects on the thrust faults.

All particles, with radii of 60 and 80 m, were randomly generated and allowed to settle within a two dimensional domain 120 to 240 km long and 15-20 km tall, defined by fixed walls of particles at the lateral edges of the domain and along the base. The particles of the predelta layer are then bonded together (Table 1) introducing a cohesive strength. Thus, the predelta layer will tend to deform brittley when loaded through sedimentation while the mobile shale flows underneath. Once the substrata are defined, layers of sediments are deposited in the proximal region to mimic deltaic loading. This sediment wedge is formed by adding particles above the left 20 km of the models and letting them settle (Figure 3.6b). Sedimentation rates of 10,000 m/Ma, 800 m/Ma, and 160 m/Ma are used, with intervals between depositions defining the rate. The lowest rate is an estimate of actual sedimentation rates in the Niger Delta, rescaled to 0.05 m/s in the models, (Shell, pers. comm.) while the other two rates are exaggerated. Each new layer is designed to be ~1 particle thick (80 m), and intervals in-between deposits are higher for the slower sedimentation rates.

Five model suites were run in order to investigate the effects of five different parameters (Table 2): Models 1.1-1.7 investigated the effects of varying the thickness of the mobile shale, since this parameter can change over time in natural systems, and might vary

in different parts of the delta. Models 2.1-2.6 investigated the effects of changing the pre-delta layer thickness, since this layer also increases over time in natural systems, and therefore might affect deformation patterns such as fault spacing. Model 3 investigated the influence of a continent-ward slope in the basement. The Niger Delta in particular is has a basal slope toward the continent, rather than being horizontal. Models 4.1 and 4.2, combined with model 1.4, explore the effects of sedimentation rate. Model 5 examines the case of oceanward thinning of the predelta and mobile shale layers, similar to the Niger Delta (Figure 3.1b).
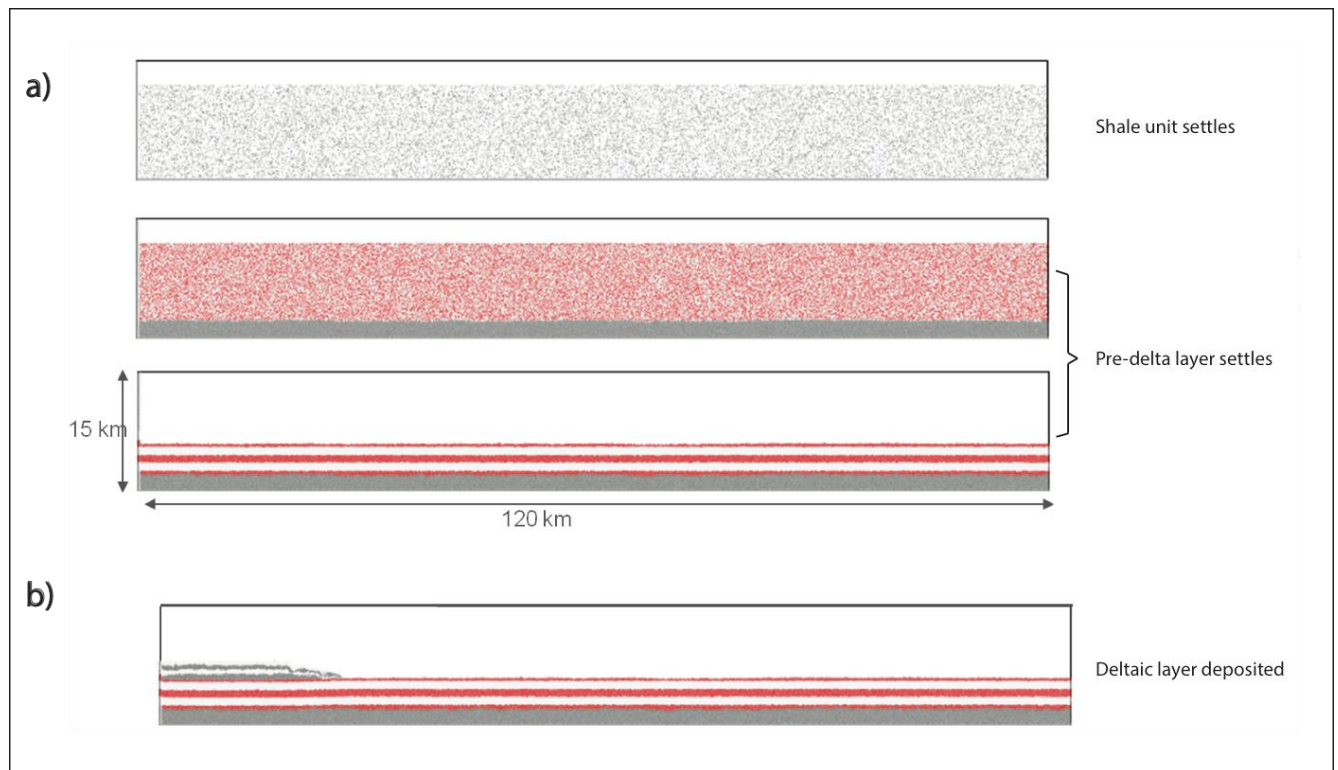
Figure 3.5 - Construction of model domain. a) Particles are randomly generated with a domain 120 km long and 15 km high, and are allowed to settle under gravity. Strata are colored, and properties assigned. b) Sediments are added incrementally over the left 20 km of the domain, driving deformation of the pre-existing strata.

3.6. Results

All five of our model suites produced linked extension-compression fault systems, with normal faults occurring under and within the sediment wedge, and thrust faults forming at the toe of the wedge. The specific locations of the thrust faults and the nature of the deformation within the mobile shale vary with the model suites. The models are displayed in Figures 3.6-3.13, showing the particle configurations and distortional strain, calculated as the 2nd strain invariant of the deviatoric stain tensor, for four representative stages during deformation (Dean et al, 2013). Within the strain plots, shear strain with the top moving towards the foreland is shown in red, while blue indicates shear strain directed towards the hinterland. In the deltaic sediments, the strain plots show the distinct sedimentary layers separated by blue lines. An artifact of the processing, the lines reflect apparent relative displacement of the old and new particles. Therefore, although they do not represent deformation in the sediments, they are good stratigraphic markers in the deltaic growth strata, and highlight normal faults that develop in the sediments, as they are initially horizontal, and rotate and are offset as they are cut by normal faults.

Table 3.2 Model suites and parameters

Suite	Models		Shale thickness (km)	Predelta thickness (km)	Sed. rate (m/Ma)	Base angle (º)
Model suite 1	1.1	1.1.1 1.1.2 1.1.3 1.1.4 1.1.5 1.1.6 1.1.7 1.1.8 1.1.9 1.1.10	0.0	4.0	10,000	0
	1.2		0.5	4.0	10,000	0
	1.3		1.0	4.0	10,000	0
	1.4*		2.0	4.0	10,000	0
	1.5		2.3	4.0	10,000	0
	1.6		4.0	4.0	10,000	0
	1.7		5.0	4.0	10,000	0
Model suite 2	2.1		2.0	1.0	10,000	0
	2.2		2.0	1.7	10,000	0
	2.3		2.0	2.5	10,000	0
	2.4		2.0	3.0	10,000	0
	2.5*		2.0	4.0	10,000	0
	2.6		2.0	4.6	10,000	0
Model suite 3	3.1		2.0	4.0	10,000	3
Model suite 4	4.1		2.0	4.0	800	0
	4.2		2.0	4.0	160	0
Model suite 5	5.1		4.5-2.0	4.0-2.0	10,000	0

* indicates same model

3.6.1. Model Suite 1

Model Suite 1 was run with seven different thicknesses of mobile shale ranging from 0 km to 5 km. Fig. 3.6-3.8 display the resulting particle configuration (top plot) and 2nd strain invariant (second plot) for four different stages of deformation for three representative models, 1.1, 1.4, and 1.7, respectively.

The typical sequence of deformation in these models consists of sedimentary wedge growth, which causes normal faults to develop. The normal faults start in the sedimentary wedge and propagate down into the predelta layer. In addition, a sliding surface develops between the frontal portion of the sedimentary wedge and the predelta layer. In all of the models, normal faults formed with both regional and counter-regional dips. Generally one pair of normal faults dominated the extensional deformation (Figure 3.6a, 3.7a). Once the sedimentary wedge grows large enough, is causes contraction in the frontal (distal) region; thrust faults developed in the predelta layer at the wedge toe, then broke forward (towards the basin) as deformation and sediment loading continued. Toe thrusts of both vergences occurred in each model.

Key differences were observed in the model runs. Model 1.1 contained no mobile shale, so slip was localized at the contact between the predelta layer and the base of the model, and only formed popup structures during deformation. These structures continued to contract and were partially closed, the faults became concave down as they were squeezed together, after formation (Figure 3.6d). Model 1.4, with 2 km of mobile shale (Figure 3.7), developed a forward breaking sequence of three forethrusts and two backthrusts in the predelta layer (Figure 3.7d). A décollement developed along the base of the model, between the mobile shale and the base, with some distributed deformation occurring in the mobile shale above. Model 1.7, with 5 km of mobile shale (Figure 3.8), initially developed a major regional normal fault near the back wall (Figure 3.8a), in contrast to the regional and counter-regional pairs that dominated the extensional deformation in previous models. Deformation with the thicker mobile shale layer, was

defined as a diffuse region of distributed strain that propagated oceanward over time. Thrust faults initiated at shallow depths in the pre-delta layer and propagated down to merge with the sheared zone in the mobile shale (Figure 3.8b-d). This is in contrast to the models with mobile shale units thinner than 4 km, where normal faults extended to the mobile shale, into a décollement until linking up with thrust faults at the toe.

3.6.2. Model Suite 2

Model Suite 2 was run with constant mobile shale thickness (2 km) but with six different thicknesses of the pre-delta layer, ranging between 1 and 4.6 km. Figures 3.9 and 10 display the resulting particle and 2nd strain invariant field for representative models 2.1 and 2.6. The same typical sequence of deformation was observed in these models as was observed in model suite 1. Both simulations display normal faults under and within the sedimentary wedge, which drove compression and thrust faulting at the wedge toe. Both forethrusts and backthrusts occurred in each simulation.

In model 2.1 two pairs of regional and counter-regional faults dominated the extensional deformation under the sediment wedge (Figure 9a). Deformation extended down to the base of the model, and slip occurred primarily along the very base, connecting the normal faults with the toe thrusts. The toe thrusts initially formed a broad popup structure (in the predelta layer) immediately in front of the sediment wedge (Figure 3.9b). A forethrust developed in front of the pre-existing popup structure, and is subsequently intersected by a backthrust (Figure 3.9c). Oceanward of the backthrust, three in-sequence fore thrusts then form (Figure 3.9d). The first forethrust forms a popup structure with the

backthrust. In general, more faults form in model 2.1, with the thin predelta layer, then form in models with thicker predelta layers. In addition, strain in the thin predelta layer is highly localized, but becomes more distributed in the mobile shale layer.

In Model 2.6, deformation initiates a little differently, with two regional faults forming within and beneath the sediment wedge (Figure 3.10a). Eventually, a counter-regional fault forms below the slope break of the sediment wedge, although most of the extension continues on the regional faults. Sliding along the base of the model connects the regional normal faults with the toe thrusts, the first of which forms as a backthrust at the tip of the sediment wedge (Figure 3.10b). This initial structure evolves into a popup structure with the formation of a subsequent forethrust (Figure 3.10c). Finally, another backthrust forms out in front of the popup structure (Figure 3.10d). In total, only three toe thrusts form, compared to seven observed in model 2.1 (Figure 3.9d), for the same amount of sedimentary loading.

3.6.3. Model Suite 3

Model Suite 3 (Figure 3.11), consisting of only one simulation, used a different initial basal geometry. The base of the model sloped ~3° toward the continent, representing the end stage of the evolving regional slope of the basement, interpreted on seismic cross-sections of the Niger delta (Figure 3.1b). Otherwise, the modeling parameters are the same as Model 1.4 (Figure 3.7), with a mobile shale 2 km thick and a predelta layer 4 km thick. In this case, deformation initiates under the sediment wedge, with an intersecting regional and counter-regional fault pair. The regional fault forms a diffuse zone of shear in the

mobile shale that eventually propagates updip in front of the sediment wedge (Figure

3.11a). This strained zone connects to the toe thrusts, the first of which forms just in front

of the sediment wedge (Figure 3.11b). A second in-sequence thrust forms as deformation

and sedimentary loading continues (Figure 3.11d). The first thrust forms at approximately

the same location and at about the same time in both models 3.1 and 1.4. However, it takes

twice as long for the second thrust fault to form in model 3.1 than in model 1.4. For the

same amount of time, of the model runs, only two thrusts form in model 3.1 versus five in

model 1.4.

Figure 3.6 – Model 1.1. Four stages during the deformation of Model 1.1, which has no mobile shale. Top plot of each pair is the particle configuration, the bottom plot is the 2nd strain invariant of the deviatoric strain tensor. For the latter, red indicates movement towards the foreland, and blue indicates movement toward the hinterland. a) Sedimentation begins, and a counter-regional and regional normal fault pair develop underneath. Shortening in front of the sediment wedge is accommodated b sliding along the base of the model. b) The first thrust faults form a popup structure in front of the sediment edge. c) A second popup structure forms in front of the first, while locally a weld develops under the sediment wedge. d) the thrust faults from c) are partially closed due to contraction, and become slightly concave. (Figure on next page)

Model 1.1
Image 010
a)
counter-regional and regional fault pair
sliding along base of model

Image 020
b)
first popup structure

Image 026
c)
second popup structure
sliding along base of model

Image 030
d)
faults become concave

Figure 3.7 - Model 1.4. Four stages during the evolution of Model 1.4, which has a mobile shale layer of 2 km. Colors and panels same as in Fig. 3.6. a) A counter-regional and regional normal fault pair develops under the sediment wedge. Shortening in front is accommodated by sliding along the base of the model. b) The first thrust fault develops in front of the sediment wedge, while a second normal fault pair develops beneath it. c) A series of in-sequence thrusts develops, with relatively discrete strain in the predelta layer broadening to a more distributed region in the mobile shale. d) Two backthrusts form, the first of which is blind and intersects the previous forethrust while the second in emergent. (Figure on next page)

a) model 1.4 / 2.5 — Image 010. counter-regional and regional fault pair. sliding along base of model.

b) Image 016.

c) Image 023. In-sequence thrust faults develop. distributed strain in mobile shale.

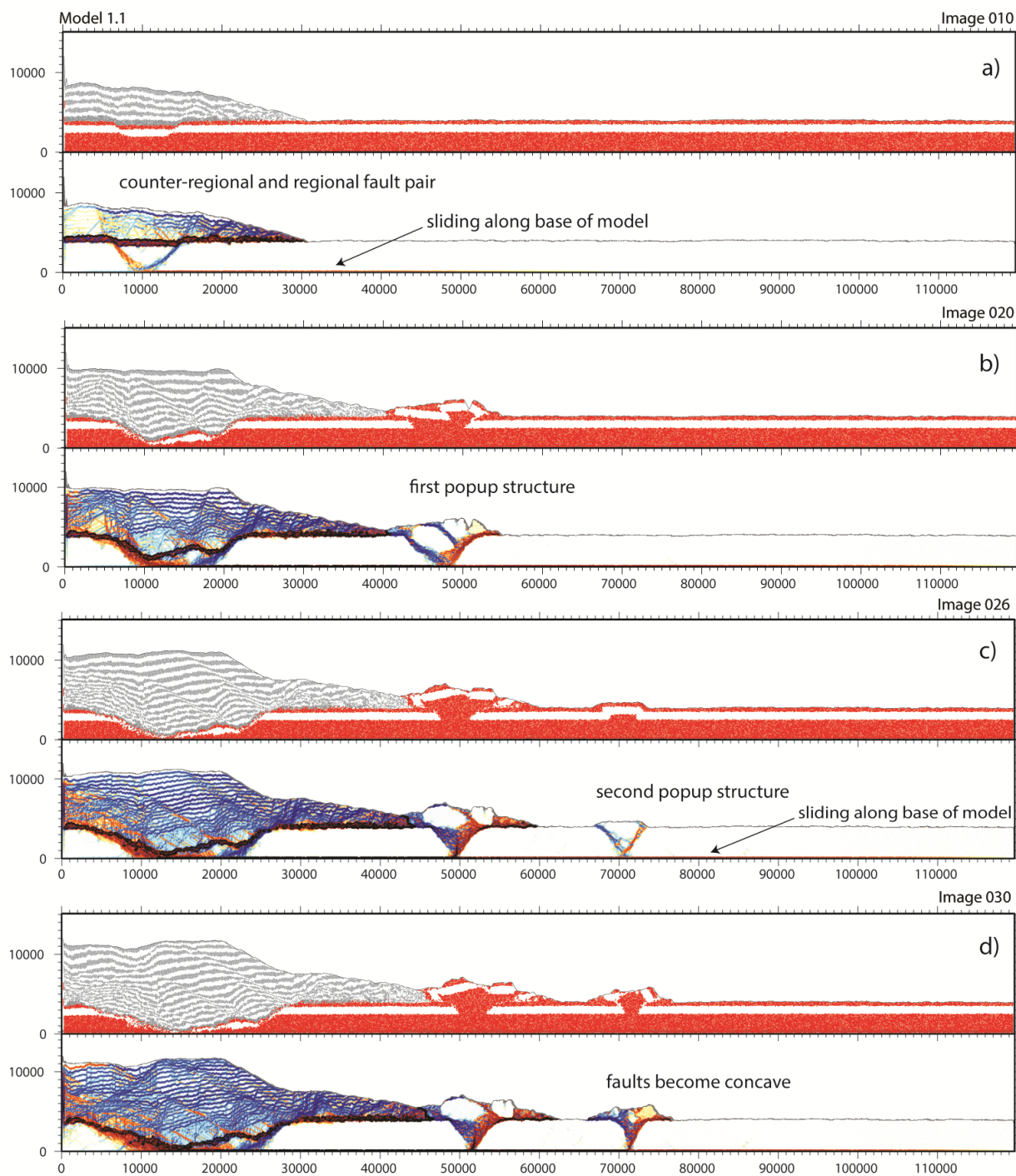d) Image 030. formation of backthrusts.

Figure 3.8 – Model 1.7.

Four stages during the evolution of Model 1.7, which has a mobile shale layer of 5 km. Colors and panels same as in Fig. 3.6. a) A regional fault develops first, becoming a subhorizontal zone of distributed strain in the mobile shale layer. b) A smaller counterregional fault develops in the sediment wedge, while the first thrust fault forms in front of it, propagating from the pre-delta layer down into the strained zone in the mobile shale. c) A second regional normal fault develops, as well as a second thrust fault. d) A blind backthrust intersects the last forethrust. (Figure on next page)

model 1.7 — Image 010

a) regional fault — distributed strain inmobile shale model

Image 018

b) Propagates down into mobile shale

Image 025

c) regional and counter-regional fault pair develops
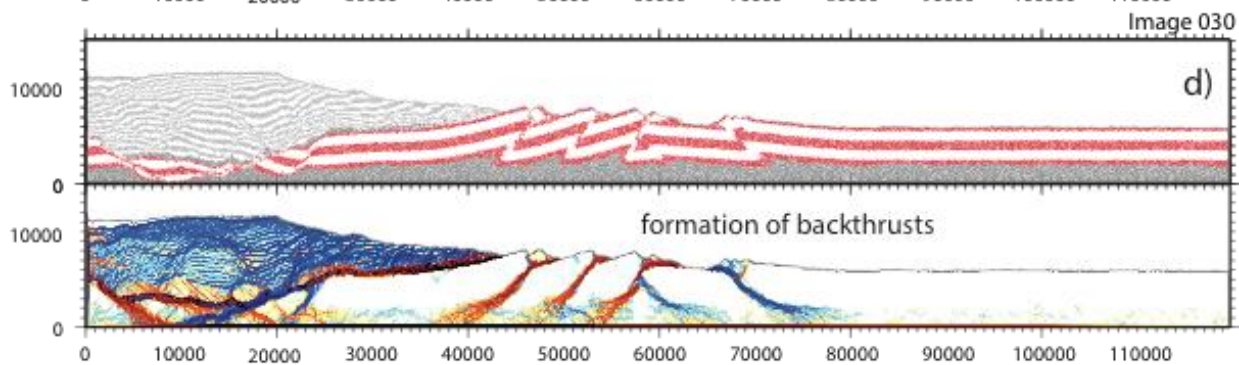
Image 031

d) blind backthrust intersects forethrust
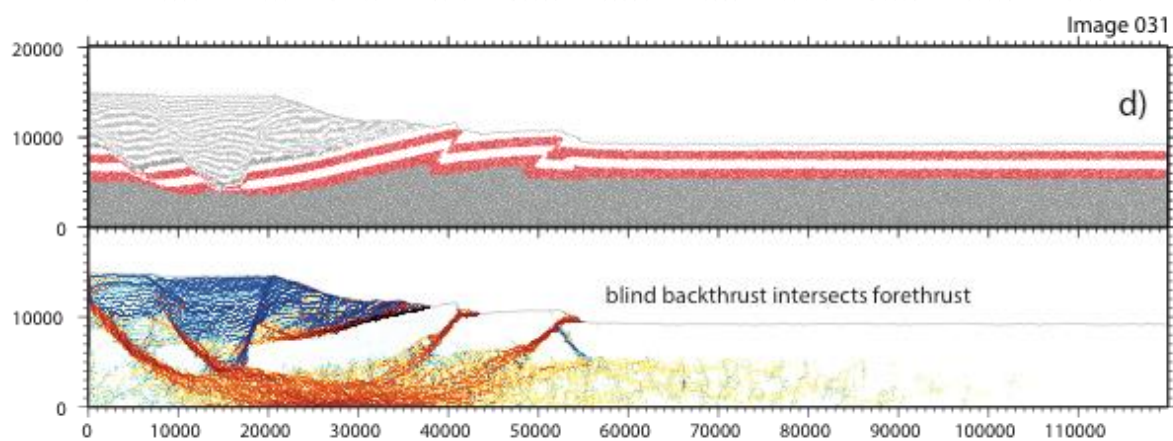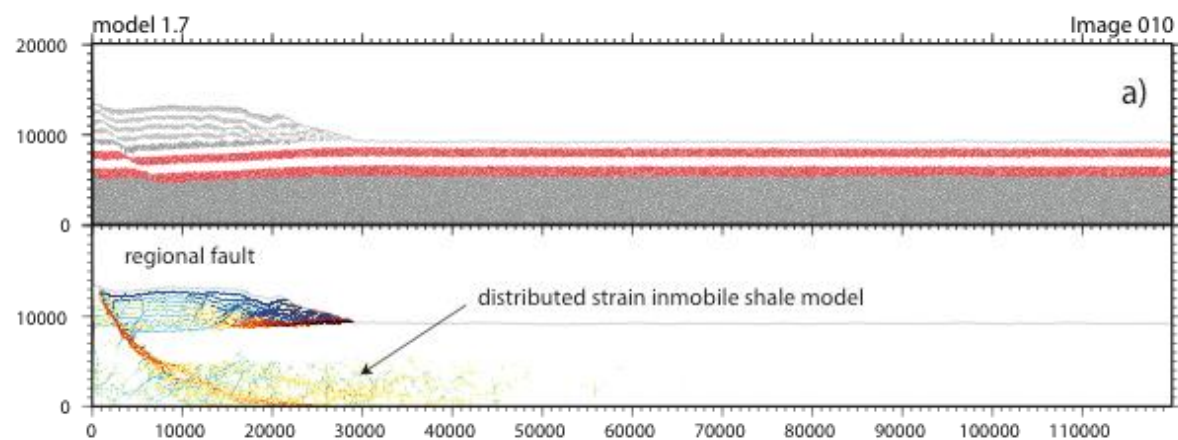
Figure 3.9 – Model 2.2. Four stages during the evolution of Model 2.2, which has a predelta layer of 1.6 km. Colors and panels same as in Fig. 3.6. a) Multiple regional and counter-regional faults develop in the sediment wedge, and a backthrust forms at its tip. Additional contraction is accommodated by sliding on the base of the model. b) A forethrust forms a broad popup structure with the previous backthrust. The strain in the predelta layer is relatively discrete in the predelta layer, but becomes more diffuse in the mobile shale. c) A second forethrust forms, followed by a backthrust. d) The previous backthrust intersects the forethrust behind it, creating an "x" structure. In front, three in sequence forethrusts develop. (Figure on next page)

model 2.2 — Image 010

a) multiple regional and counter-regional faults form

sliding along base of model

Image 013

b) broad popup structure

distributed strain in mobile shale

Image 020

c)

Image 030

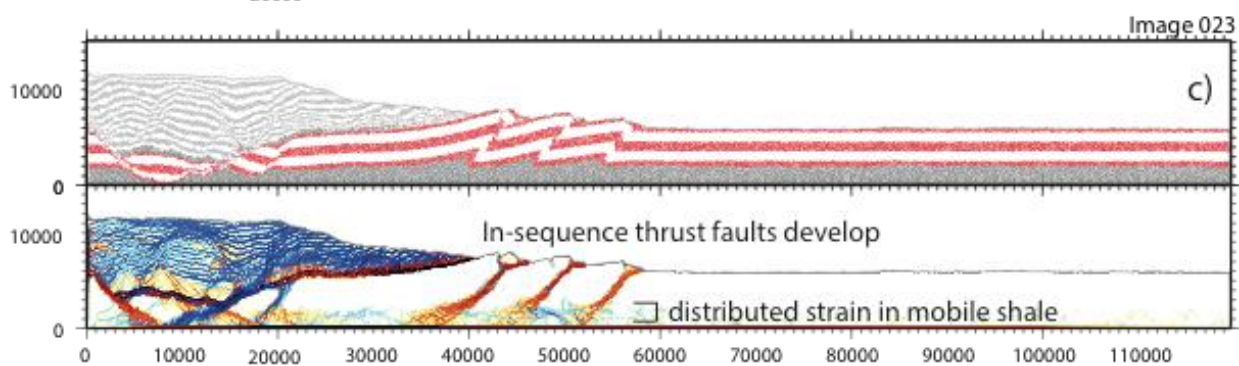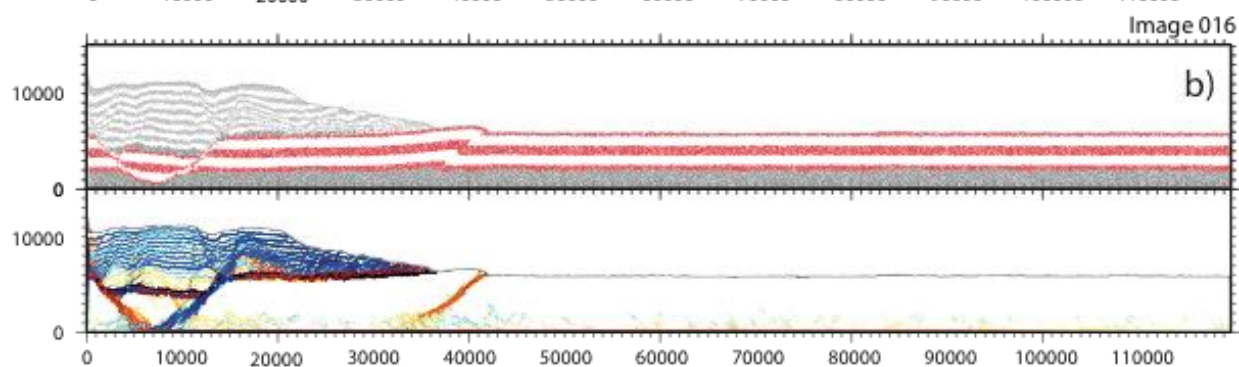d) intersecting forethrust and backthrust
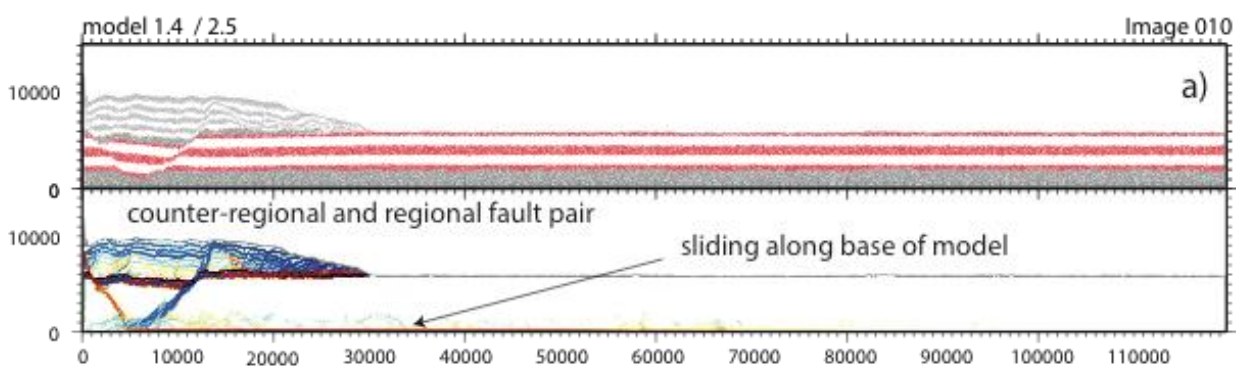
in-sequence forethrusts
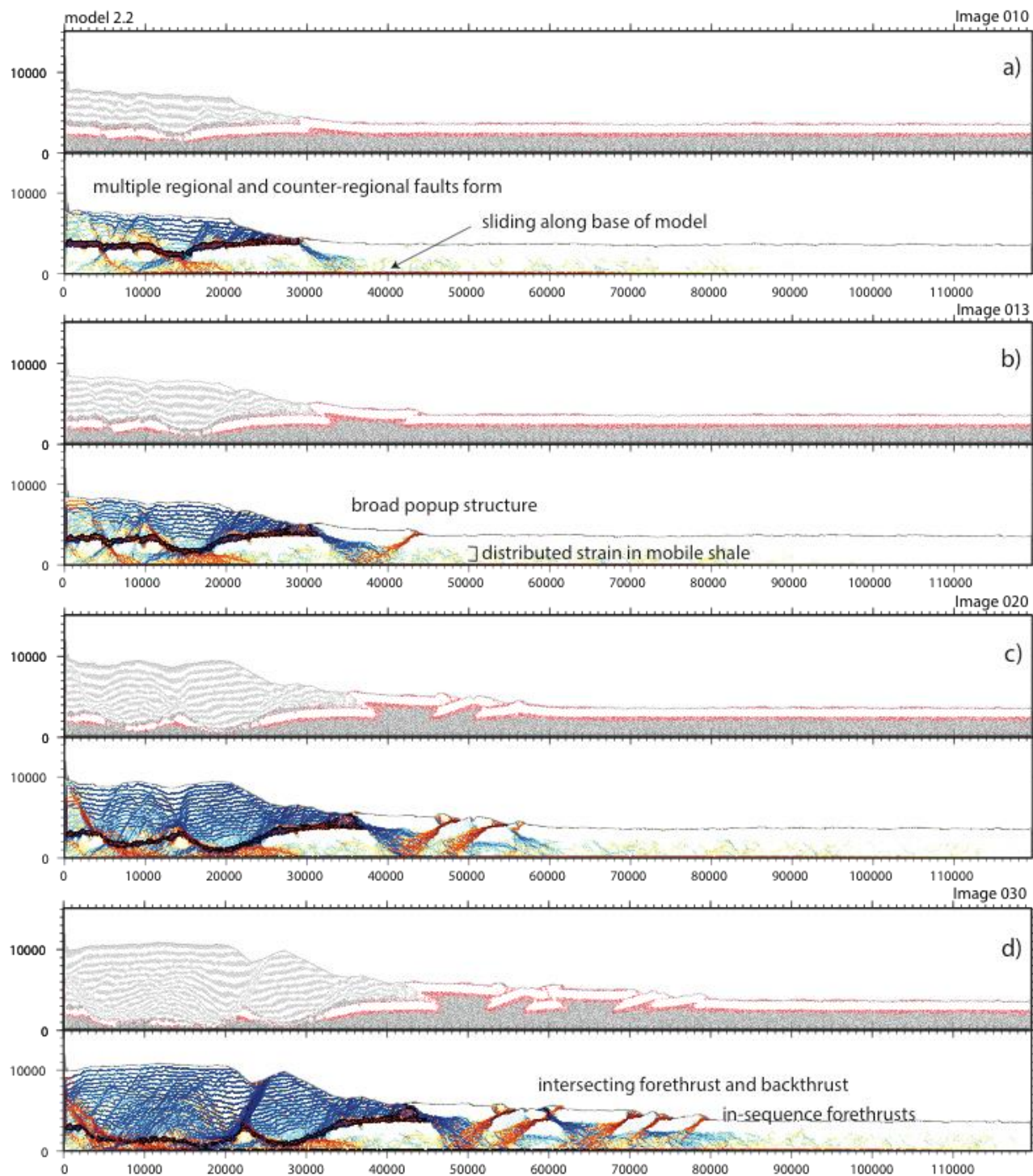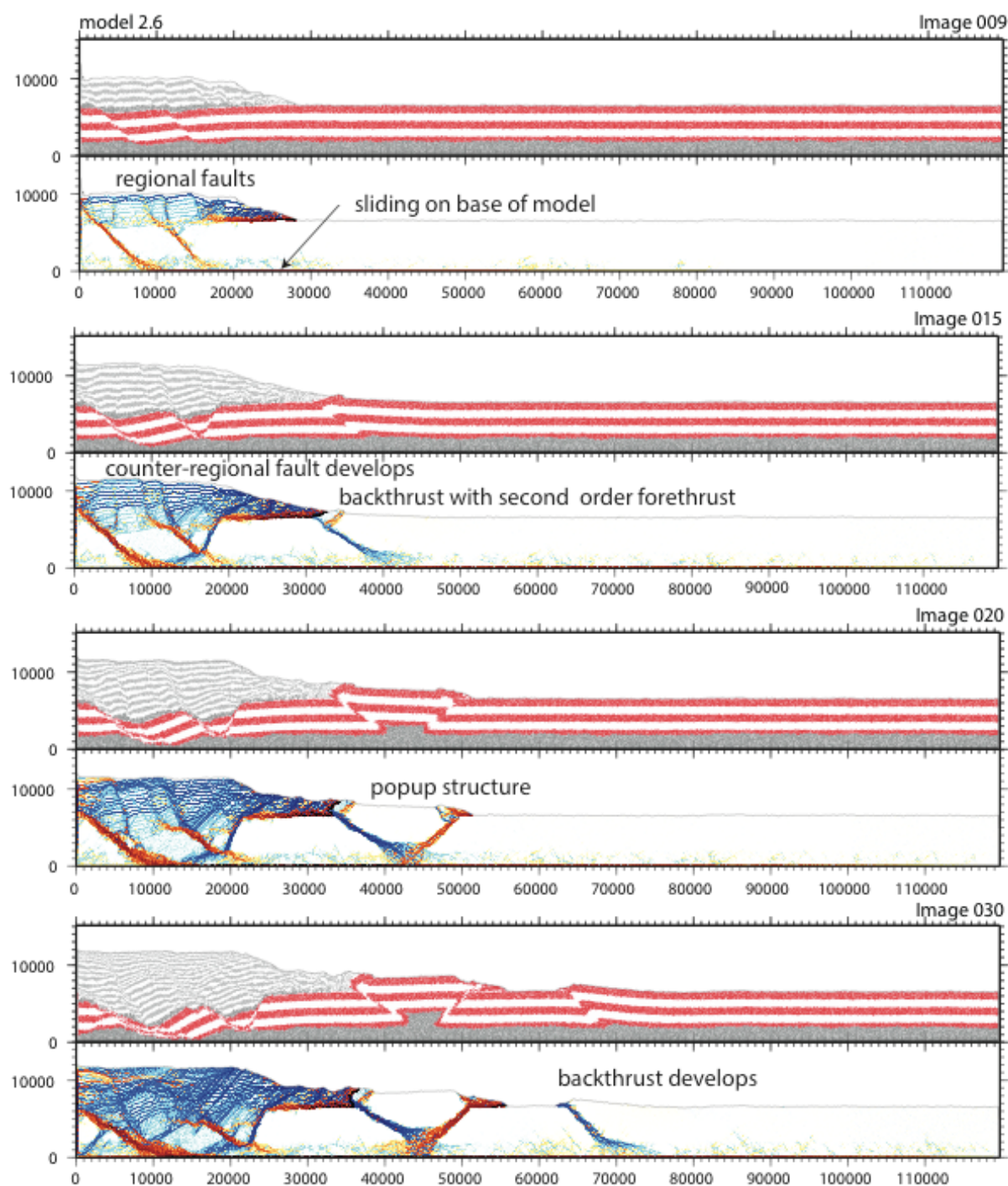
Figure 3.10 – Model 2.6. Four stages during the evolution of Model 2.6, which has a pre-delta layer of 4.6 km. Colors and panels same as in Fig. 3.6. a) Two regional faults develop under the sediment wedge. b) A backthrust with a second order forethrust forms in front of the sedimentary wedge. c) A forethrust forms in front, creating a popup structure. d) A final backthrust develops in the foreland.

Figure 3.11 – Model 3.1. Four stages during the evolution of Model 3.1, which is the same as model 1.4 except the base is tilted three degrees. Colors and panels same as in Fig. 3.6. a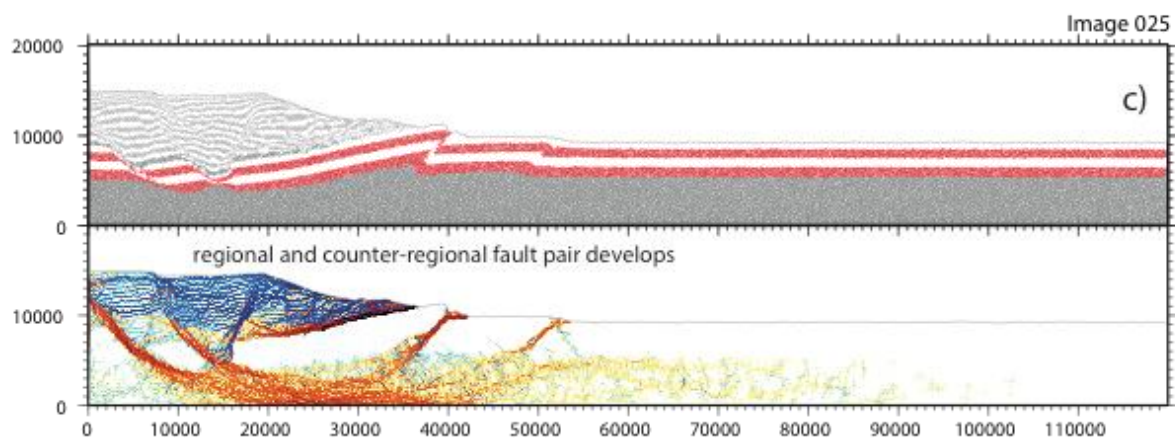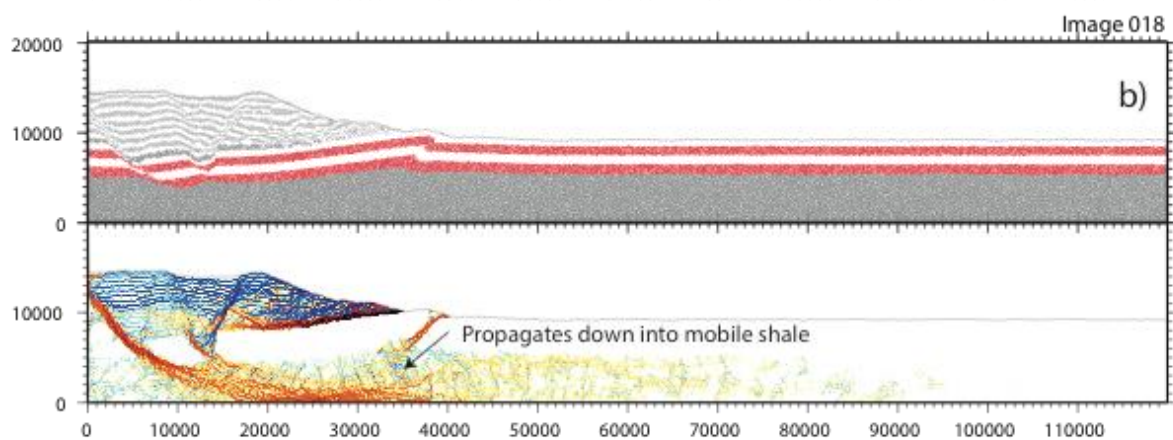) A regional and counter-regional fault pair develop under the sediment wedge, with the regional fault propagating into the mobile shale towards the tip of the sediment wedge. b) A forethrust develops in front of the sediment wedge. c) Strain propagates in front of the forethrust within the mobile shale. d) A second forethrust forms in front of the first. (Figure on next page)

a) Image 012

regional and counter-regional faults develop

distributed strain in mobile shale

b) Image 018

new regional fault

forethrust

c) Image 030

strain extends through total thickness of mobile shale

d) Image 040

forethrust
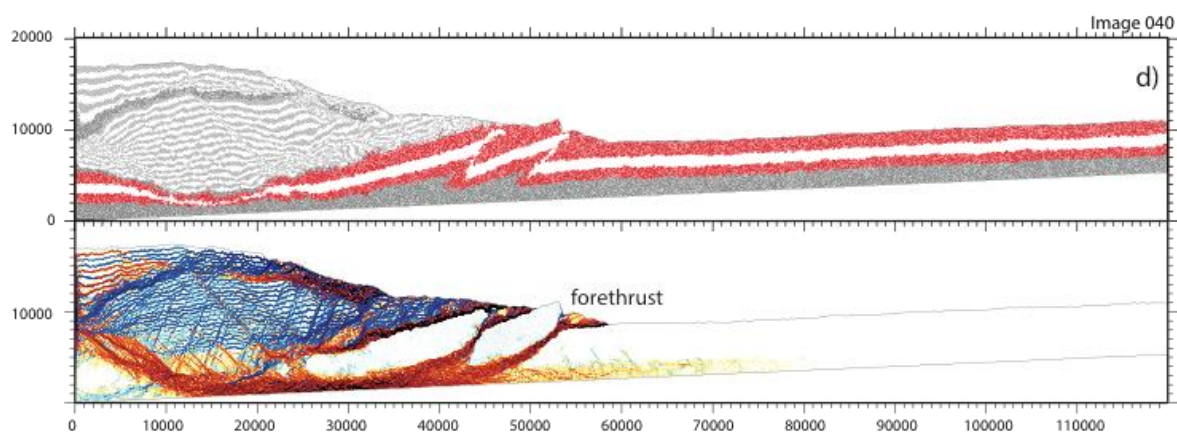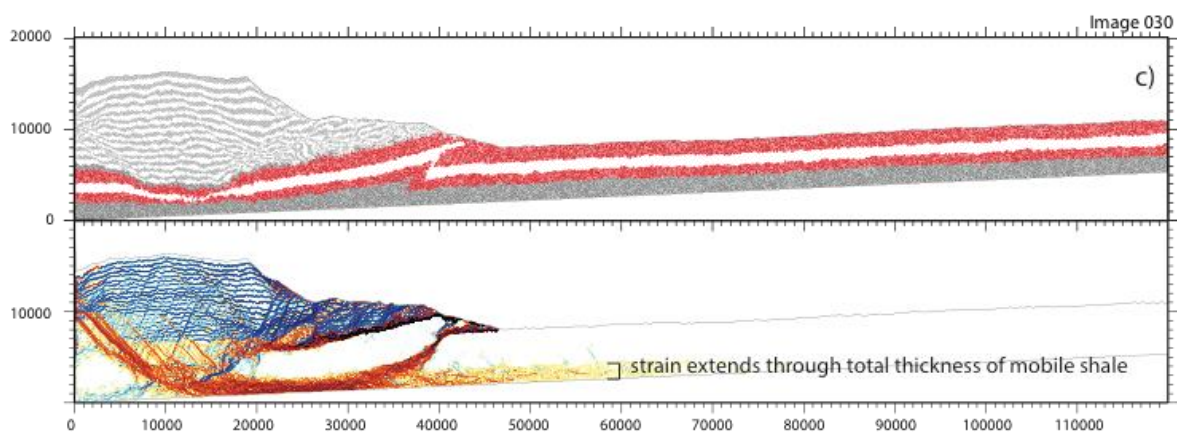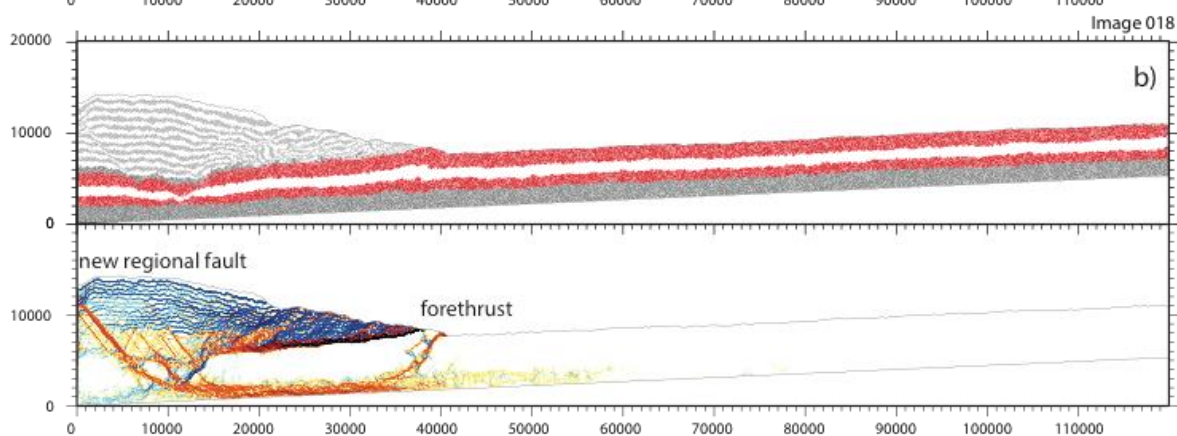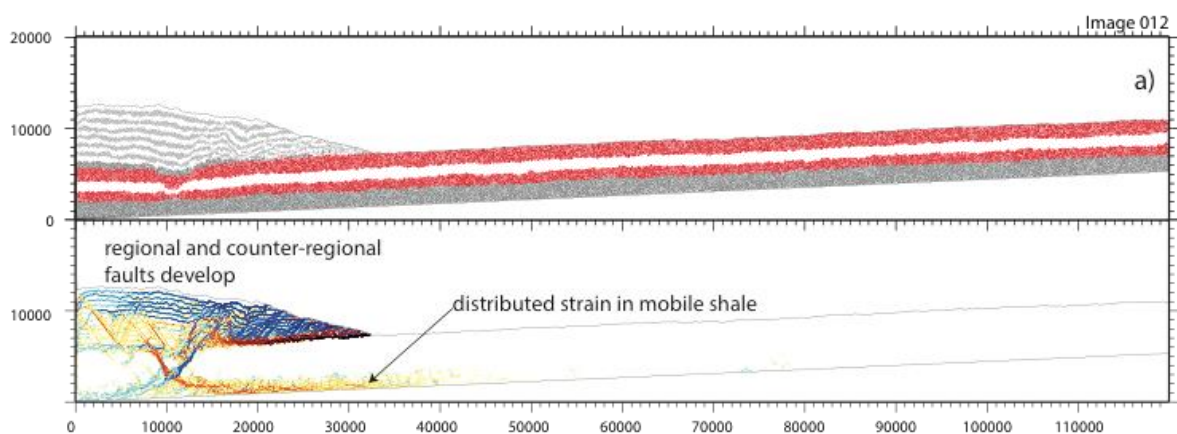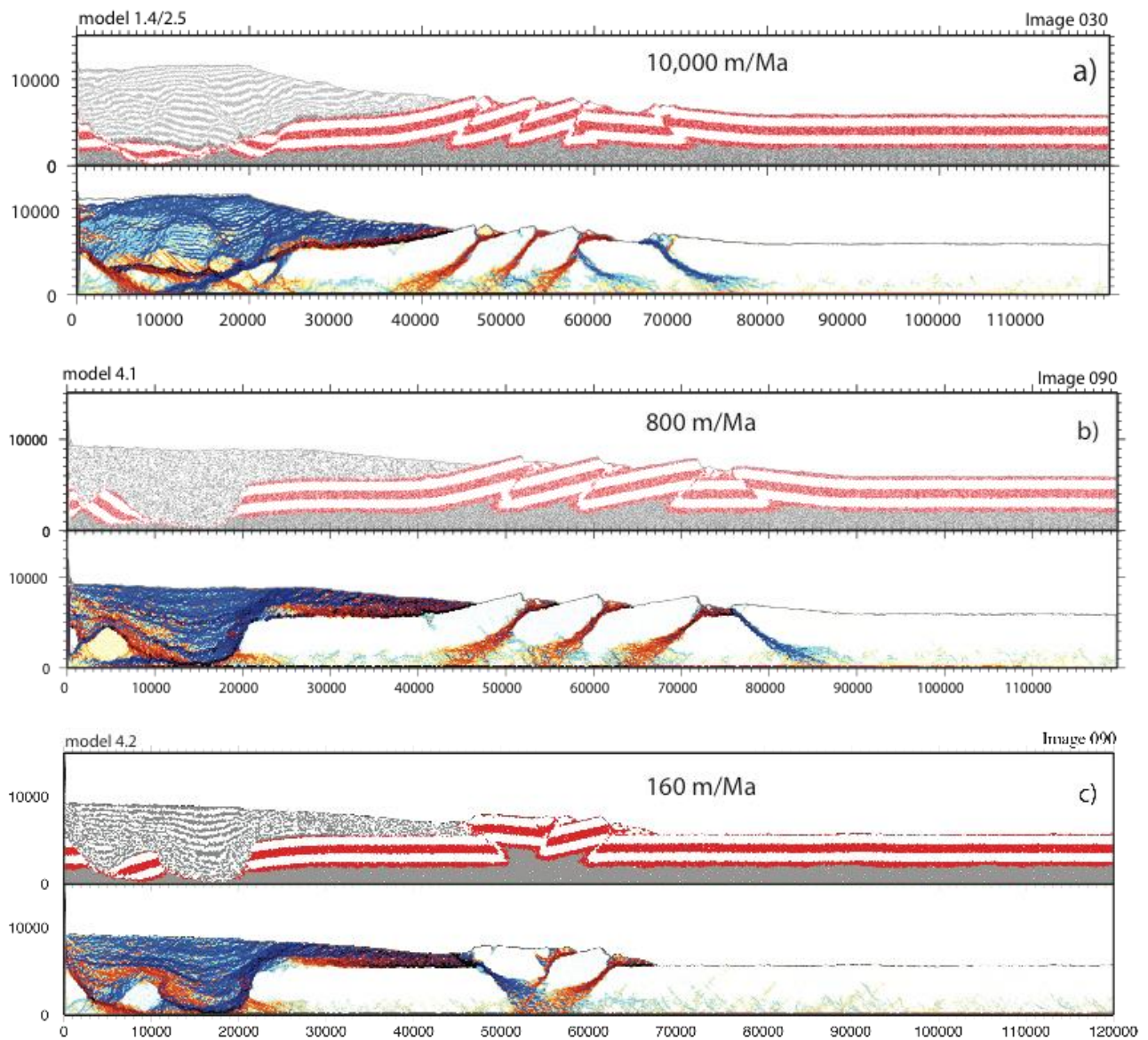
Figure 3.12 – Sedimentation rate models. Three final configurations of Models 1.4, 4.1 and 4.2 (a-c) with respective sedimentation rates of 10,000 m/Ma, 800 m/Ma, and 160 m/Ma. Each plot shows the same general structures in the same location in front of the wedge tip, indicating that sedimentation rate is not a controlling parameter in the formation or vergence of the toe thrusts.

3.6.4. Model Suite 4

Model Suite 4 explored the effects of sedimentation rate, with other parameters matching those of Model 1.4, with 2 km thick mobile shale and 4 km thick predelta layer. The sedimentation rate of model 1.4 was 10,000 m/Ma, whereas model 4.1 and 4.2, had sedimentation rates of 800 m/Ma and 160 m/Ma, respectively. Figure 3.12 shows the final configuration for each of the three simulations. The simulations have very similar faulting sequences and final patterns, particularly Model 1.4 and 4.1. The pattern of normal faulting in the fastest sedimentation rate model (model 1.4, Figure 3.7) is complex, with multiple regional and counter-regional faults in the predelta layer and in the sediment wedge, although ultimately two fault pairs dominate the deformation. In contrast, the models with slower sedimentation rates show one (model 4.1) or two (model 4.2) regional and counter-regional pairs that dominate deformation. No additional faulting develops in the sediment wedge, and the final configuration shows one to two large basins above the normal faults. Faulting in models 4.1 and 4.2 continues until the pre-delta layer has detached beneath the wedge and the sediments are in direct contact with the mobile shale and occasionally the base of the model. Sliding occurs along the base of the model connecting the normal faults in all three models to the toe thrusts. All models have both forethrusts and backthrusts in the toe area, although models 1.4 and 4.1 have in-sequence forethrusts, while model 4.2 shows a popup structure. The amount of time for the structures to form increases with sedimentation rate, but the final structures are similar kinematically. Therefore sedimentation rate is not a controlling parameter in the deformation of the system.

3.6.5. Model Suite 5

Model Suite 5 investigated the effect of oceanward thinning of the mobile and

predelta layers (Figure 3.13), similar to the cross-section shown in Figure 3.1b. Initially,

regional faults formed within the sedimentary wedge and predelta layer (Figure 3.13a),

followed by the development of a highly sheared zone in the mobile shale layer that

propagated down dip and connected to two backthrusts that formed in front of the

sediment wedge (Figure 3.13b). Shear in the mobile shale layer eventually propagated out

to 120 km, throughout the thinned zone of mobile shale, where it connected with another

backthrust that formed at about 120 km (Figure 3.13c). The same amount of sedimentation

occurred in this model as in models 1 and 2 (Figures 3.6-3.9), but the resulting deformation

propagated much further. This is likely due to the smaller amount of work needed to

deform a thinner mobile shale unit compared to a thicker package.

Figure 3.13 – Model 5. Four stages during the evolution of Model 5, which have decreasing thickenessses of mobile shale and predelta layer from 60 to 120 km. Plots extend to 240 km, through only the first 140 km is shown. Colors and panels same as in Figure 3.6. a) A regional normal fault develops, and forms a diffuse zone of strain in the mobile shale layer. b) Two insequence backthrusts develop in front of the sediment wedge. c) An additional backthrust forms 60 km in front of the previous faults, where the mobile shale and predelta layer are at their narrowest. The faults are connected by the slightly strained mobile shale layer. d) Strain in the mobile shale between the two thrust faults increases. (Figure on next page)

model 5

Image015

a)

regional normal fault

Image020

b)

in-sequence backthrusts

Image020

c)

distributed strain in mobile shale

backthrust

Image030

d)

strain increases
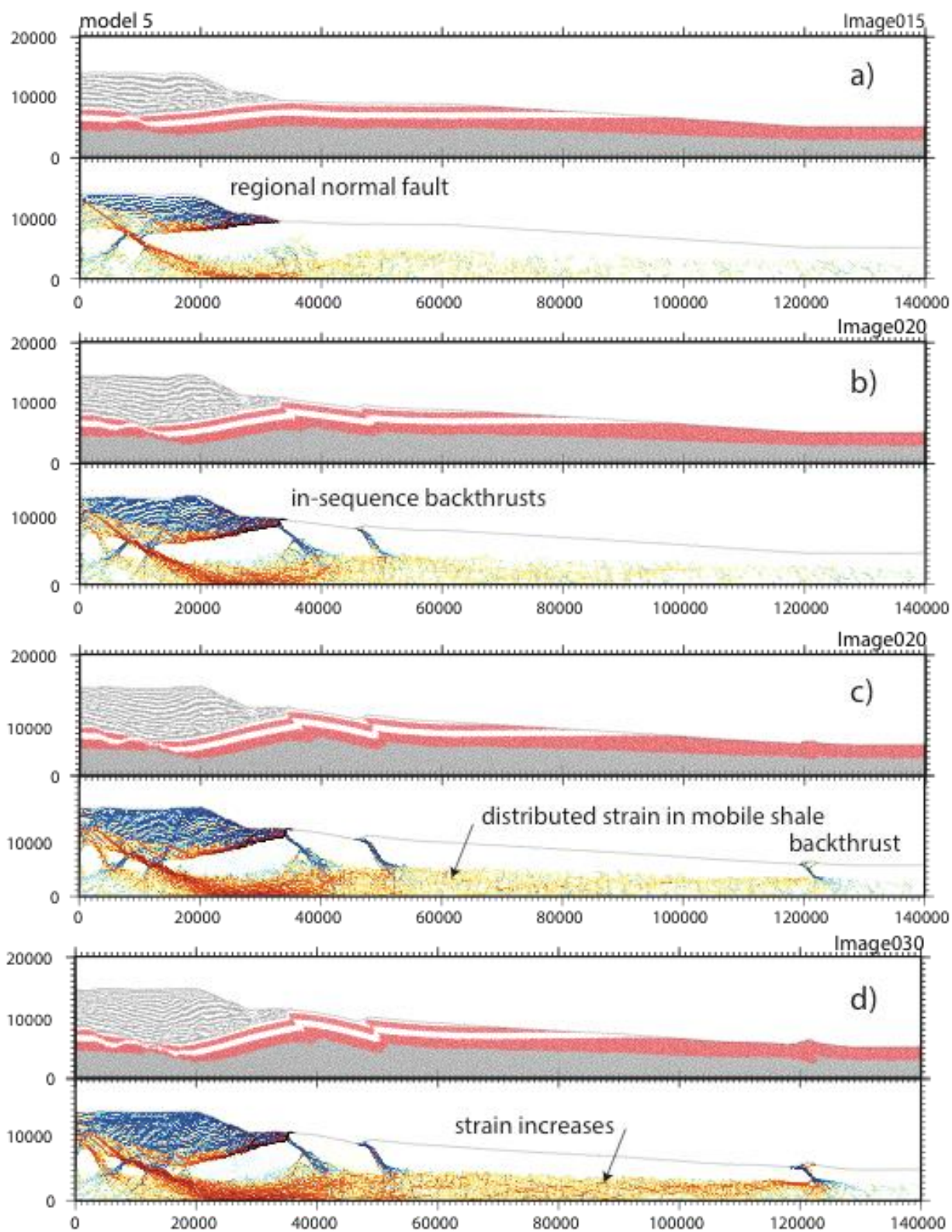
3.6.6. Fault spacing and vergence

In DEM models, faults develop where local heterogeneities either weaken the material or concentrate stress, which varies with particle distributions. In order to better establish the significance of the abundance and distribution of forethrusts and backthrusts, we carried out ten replicate simulations of model 1.4, constructed with different initial random distribution of particles, but otherwise run under identical conditions. Figure 3.14 shows the final distribution of faults for this suite of models; backthrusts are plotted as negative fault dips, and forethrusts as positive fault dips. Among the ten models, 18 forethrusts and 17 backthrusts formed, indicating nearly equal probability of each fault type. In addition, different particle arrangements affect fault vergence for each simulation.

Fault angles were consistent in most cases, from 30 to 50 degrees, with a horizontal σ_1. Fault locations were distributed over 30 to 80 km, measured from the rear wall of the simulation. Generally, faults occurred in forward breaking sequences for the ten simulations, although the distributions of forethrusts, backthrusts, and associated popup structures were different for each simulation. Therefore, the different particle arrangements for each simulation created different patterns of heterogeneities, resulting in different locations of stress concentration. That guided fault formation,and thrust faults initiated in different locations, and with different vergences due to these heterogeneities.

Thrust fault spacing was also examined in model suites 1 and 2 to explore the relationship between mobile shale thickness or predelta thickness, and fault spacing. Figure 3.15 shows the relationship between mobile shale thickness and thrust fault spacing for each experiment in model suite 1; each line represents a different model. Fault spacing

was measured in the first snapshot where a new fault appeared, and the spacing between

the new fault and the previous one was measured at the midpoint of the faults. Models 1.1

and 1.2 show a bimodal distribution of fault spacing, where the values near 5,000 m

represent the spacing between faults within popup structures, while the larger values

represent spacing between pop up structures. In the remaining models, there is no obvious

correlation between fault spacing and mobile layer thickness over the range investigated.

In model suite 2, which varied the thickness of the predelta layer, we anticipated

there to be a correlation between fault spacing and thickness of the predelta layer, as has

been observed in accretionary wedge sandbox models (Storti and McClay, 1995). However,

Figure 3.16 shows a plot of fault spacing versus predelta layer for each model in the suite 2,

and there is no clear correlation, particularly when backthrusts are present. But there is a

correlation between thickness of the predelta layer and the number of faults formed in

each model; the red triangles (Figure 3.16) denote the number of thrust faults for each

model, which generally decreases steadily as the pre-delta layer thickness increases. For

example, model 2.1 (Figure 3.9d) with a predelta layer of 1 km, has both closely spaced

faults and very broad popup structures, so that the fault spacing varies widely, from 2 km

to 17 km. Model 2.3, with a predelta layer thickness of 2.5 km (Figure 3.10d), also has

varied fault spacing, ranging from 8 km to 0 km (fault spacing is 0 km when a forethrust

and a backthrust intersect). Therefore, there is no systematic change in fault spacing with

the increase in the predelta layer. However, model 2.1, with the thinner predelta layer, has

10 faults, while model 2.3, with a thicker predelta layer, has 6 faults. Therefore, the fault

spacing appears to vary independent of predelta layer thickness, but the number of faults

in each model decreases with increasing predelta layer thickness.
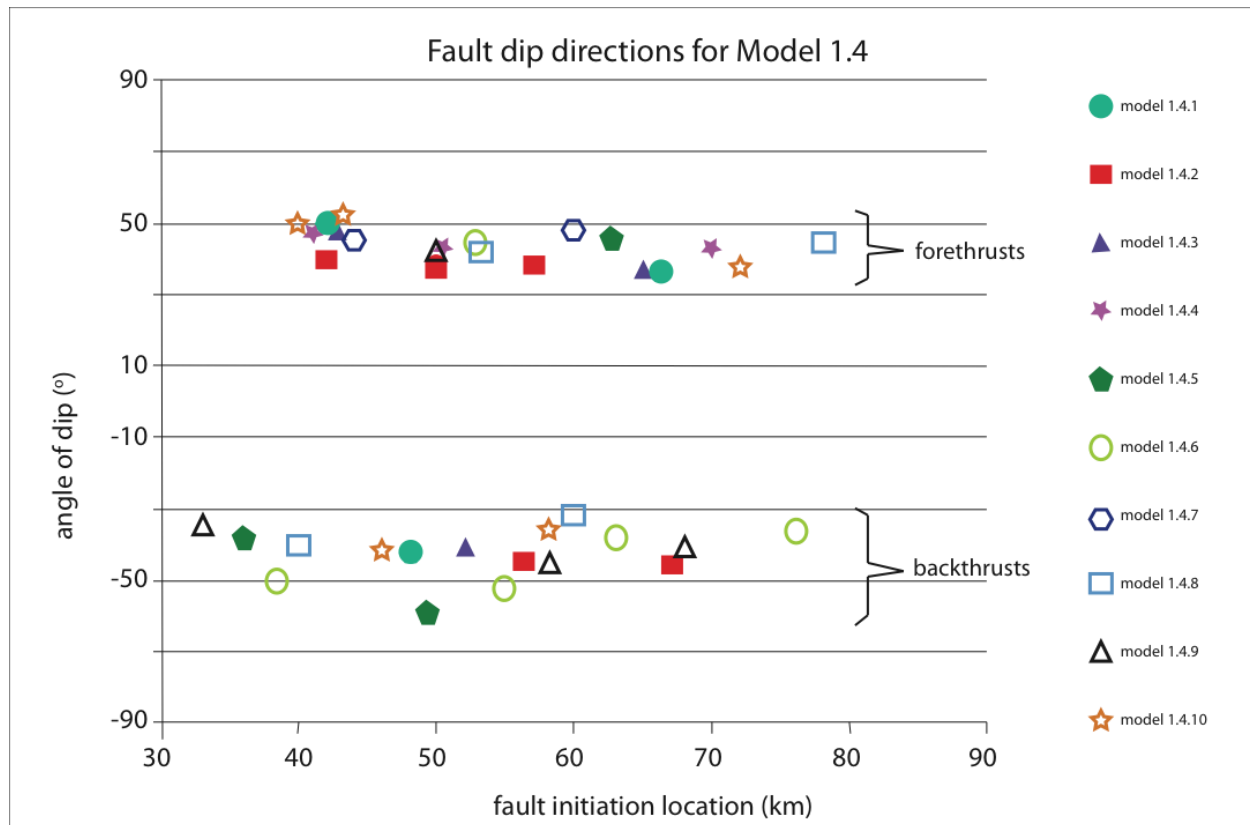
Figure 3.14 - Plot of fault dip angle versus fault location for ten runs of Model 1.4. Backthrusts are plotted as having negative dips. There was no preferred dip direction in the ten models.
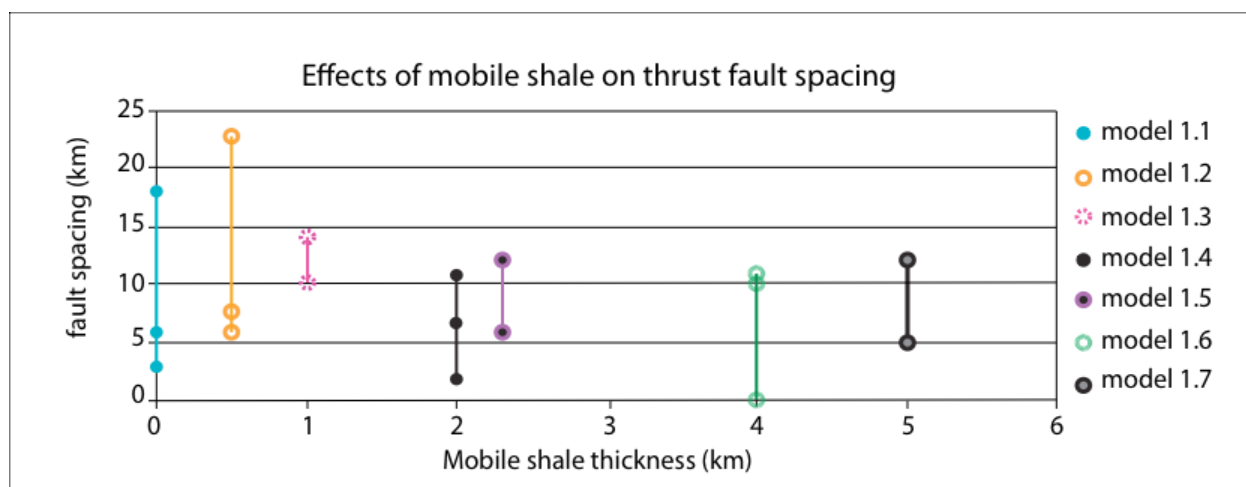
Figure 3.15 - Plot of mobile layer thickness versus fault spacing. No correlation.
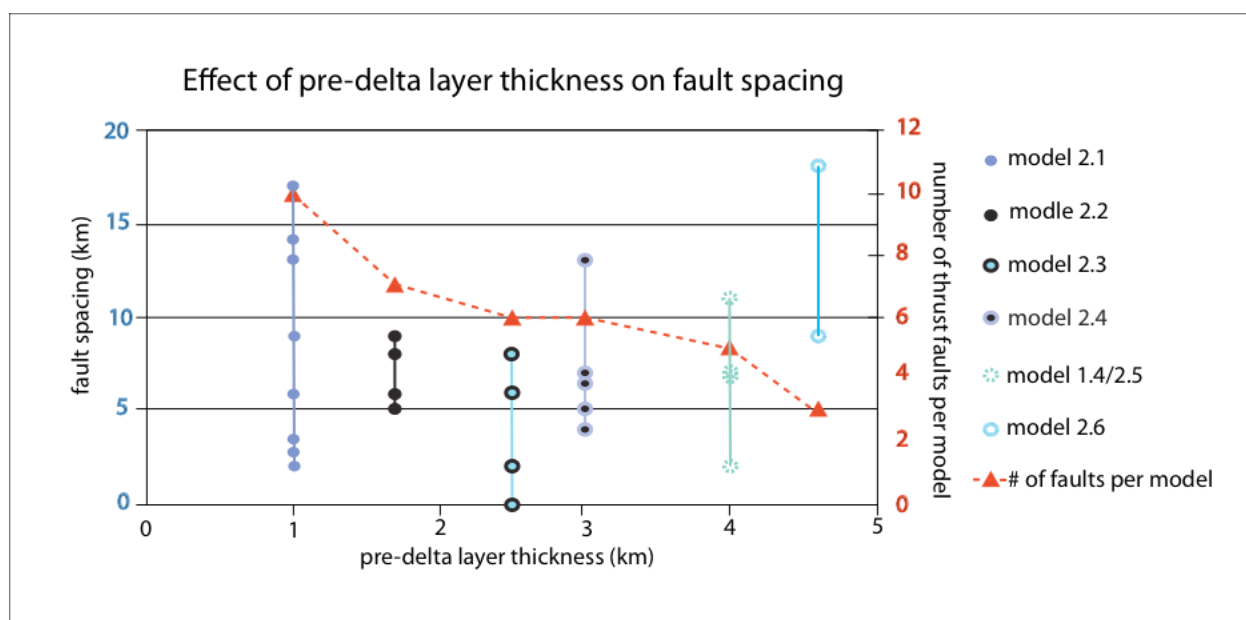
Figure 3.16 - Plot of pre-delta layer thickness versus fault spacing in blue, corresponding with the left axis, shows no correlation. The red triangles, corresponding with the right axis, show a negative trend of pre-delta thickness and number of faults per model for the same amount of sedimentary loading.

3.6.7. Stress Analysis

In order to investigate what might control thrust fault vergence we calculated the stress field and the σ_1 orientations of maximum principle stress, for model 1.6. Such continuum properties as stress can be calculated throughout the domain by averaging micromechanical properties for the particles. The average two-dimensional stress tensor over our domain is calculated by summing the normalized directional components of m contact forces acting on N particles (Morgan and McGovern, 2005(b)):

$$\sigma_{ij} = \frac{1}{V} \sum_{p=1}^{N} \left[\sum_{a=1}^{m} \left(r_i^a f_j^a \right) \right]_p$$

(Equation 7)

(in indicial notation; i, j = 1, 2, 3), where σ_{ij} represent the components of the average stress tensor, V is the volume of the averaging domain, r_i^a are the components of the particle radius normal to the contact, and f_j^a is the total force acting in the ith direction. The principle stresses, σ_1 and σ_3 are then derived, and differenced to yield the differential stress, which is fit to a continuous surface for plotting using GMT (Morgan and McGovern, 2005b).

The color-coded distribution of differential stress between 20 and 40 km distance is plotted for model 1.4 in Figure 3.17. Superimposed vectors (black lines) denote orientations of the maximum compressive stress, σ_1. As sediment loading initiates (Figure 3.17a), σ_1 magnitudes are large and subvertical in the predelta layer under the sediment wedge. σ_1 decreases in magnitude away from the sediments, although it remains approximately subvertical. As the simulation progresses and the sediment wedge grows,

the horizontal stress within the predelta layer increases in front of the sediment wedge until σ_1 becomes sub horizontal (Figure 3.17b). The region of subhorizontal σ_1 expands outward with subsequent thrust faulting (Figure 3.17c).

Similar stress fields were obtained for model 3, which had the sloping basement. This model produced only forethrusts, in contrast to model 1.4 forethrusts and backthrusts, but the stress field showed the same subhorizontal rotation of σ_1 as Figure 3.17, indicating that there was an equal likelihood of a backthrust forming, despite the basal dip.
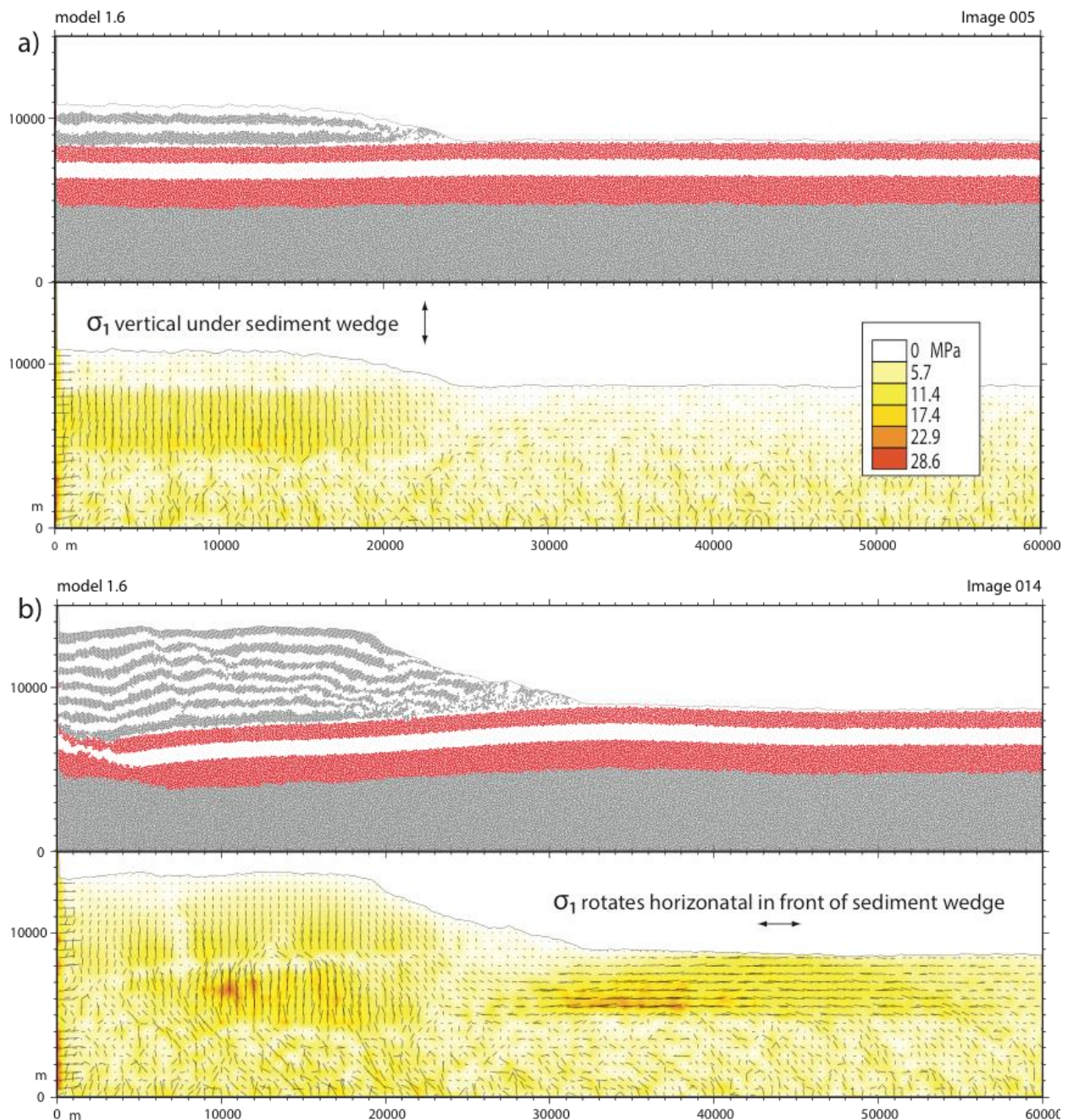
Figure 3.17 – Stress field. The top plots are the particle configurations for model 1.6, from 20 to 50 km. On the bottom the differential stress is plotted (darker yellow and red colors indicate increased stress) and overlain by black σ_1 indicators. a) The differential stress and σ_1 increase beneath the developing sediment wedge. σ_1 is largely vertical during the beginning of the simulation. b) As the sediment wedge increases, the stress field underneath it remains vertical with a detachment forming at the contact between the sediments and the predelta layer. In front of the sediment wedge, the σ_1 rotates to subhorizontal in the pre-delta layer.

3.7. Discussion

All five model suites formed toe thrust structures similar to those seen in the Niger Delta. We reproduced a linked extensional and contractional system driven by sediment loading, investigating the effects of stratigraphic thickness and sedimentation rate had on the evolution of toe thrust structures and décollements. Model suite 1 showed the effects of changing the thickness of the predelta layer, displaying a change from popup structures with a very thin mobile shale to an increase of in-sequence thrusts with thicker mobile shale. Model suite 2 investigated the effects of changing the predelta layer thickness, and found that increasing thickness correlated with decreasing thrust fault numbers, for the same amount of sedimentation. Model suite 3 showed similar patterns of deformation with a continentward sloping basement, although the number of thrusts also decreased when compared to model 1.4. Model suite 4 showed that decreasing the sedimentation rate primarily affected the extensional regime, amplifying the creation of fault bounded basins, but caused no obvious change in the location and type of structures found in the fold and thrust belts. In addition, the models with lower sedimentation rates had correspondingly lower profile sediment wedges. These models show that the artificially large sediment wedge slopes are not responsible for initiating deformation. The Niger Delta has a much larger extensional zone and depositional area as well as a varied sedimentation rate over that area, creating bathymetric slopes of less than 2° (Bilotti and Shaw, 2005). In contrast, our models had 20 km of uniform sedimentation, which was nevertheless enough to drive deformation. Finally, model suite 5 demonstrated that when both predelta and mobile shale layers were thinned basinward, (Model 5, Figure 3.13) deformation in the mobile

shale propagated much further basinward, forming thrust faults 60 km away from the sediment wedge. This resulted in the formation of a second fold and thrust belt separated from the first by a largely undeformed zone. The separation between the belts in our models is almost twice the distance seen in Figure 3.1b cross-section, though this distance does vary across the Delta. The model distance is also expected to decrease with continued deformation in the models, as well as changes in the rate of thinning of the stratigraphic units. This model suggests that the thinning of the Akata and Agbada formations in the Niger Delta could be responsible for the formation of the two fold and thrust belts and the intermediate detachment fold zone. In addition to the reproduction of two fold and thrust belts in model 5, Figure 3.18 compares schematics of seismic cross-sections from the Alpha structure in the Niger Delta (Kostenko et al, 2008) with snapshots from our models. The models succeed in representing simple structures such as popups (Figure 3.18a) as well as more complex structures such as an intersecting forethrust and backthrust, forming an x pattern (Figure 3.18b). In addition, toe thrusts were listric, similar to the Niger Delta (Briggs et al, 2006), steepening updip and curving near the intersection with the mobile shale layer.

3.7.1. Nature of modeled décollements

In contrast to seismic interpretations of distinct décollements in the Niger Delta, few clear discrete décollement surfaces developed in our models, particularly not in those models with thick mobile shale layers. Our models show that configurations with 2 km or less of mobile shale exhibited sliding along the base, which connected the extensional and contractional zones of the system. We interpret the sliding along the base of the model to

result from the boundary conditions, which combined a very smooth base and an assigned particle friction of zero to define a thin weak décollement surface at the base. When a rough basement layer was added to the models, no décollement formed along the rough basal surface, but instead deformation was distributed throughout the mobile shale (Figure 3.19). This highly distributed shear strain in mobile shale, which also occurred in models with mobile shale thicker than 2 km, (Figure 3.8) served the same role as a décollement, connecting the normal and thrust faults, but over a much thicker zone. Our models all used a homogenous mobile shale, and show that décollements do not localize under those conditions. This may be consistent with Corredor et al (2005) conclusion of penetrative shear within the Akata formation. Because the entire mobile shale undergoes distributed strain in our models, our simulations are not consistent with the interpretations of a thin décollement surface at or near the top of the mobile shale (Wu and Bally, 2000; Corredor et al, 2005). Therefore, in order to create a décollement on the order of 100 m thick at the top of the mobile shale (Briggs et al, 2006), the weak mobile shale layer must have a rheologic or lithologic change in properties (not evident in seismic data) that makes the weak zone very thin, perhaps related to overpressure, relative to the surrounding shale. This surface would have to be very smooth, since rough surfaces also favor distributed strain in the mobile shale layer (Figure 3.19). Changes in seismic reflectivity near detachment zones within the Akata formation in different parts of the Delta indicate that heterogeneities within the formation may be important for localizing detachments (Corredor et al, 2005; Benesh et al, 2014).
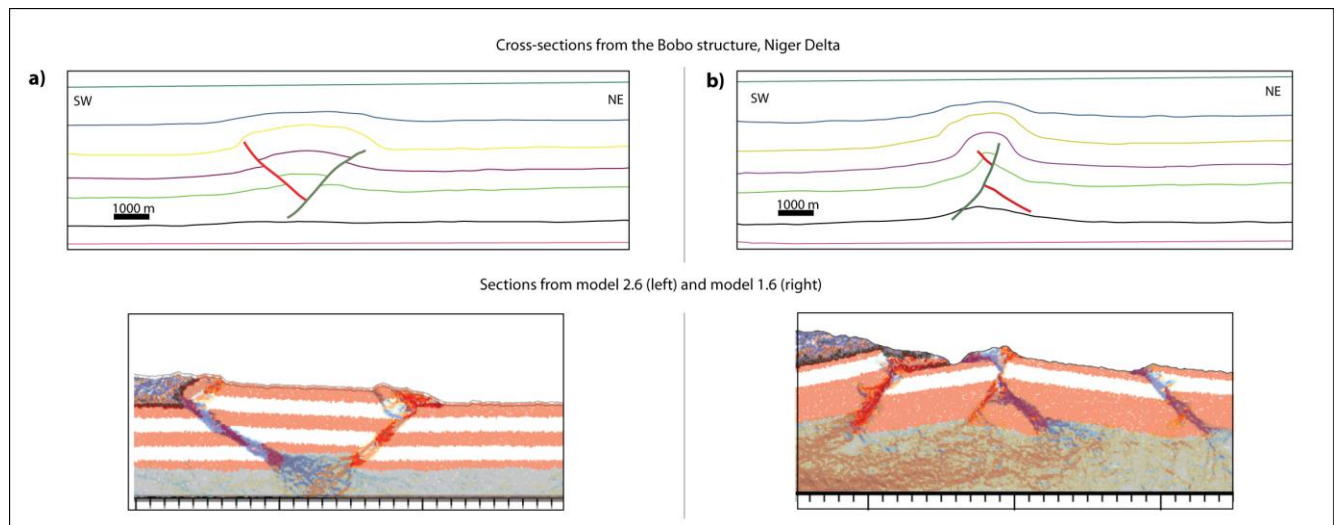
Figure 3.18 – Niger Delta comparison. Top panels show two seismic cross-sections from the Alpha structure in the Niger Delta from Kostenko et al, 2005. Bottom panels show snapshots from models 2.6 and 1.6. a) Popup structures. b) Backthrusts cut by forethrusts.
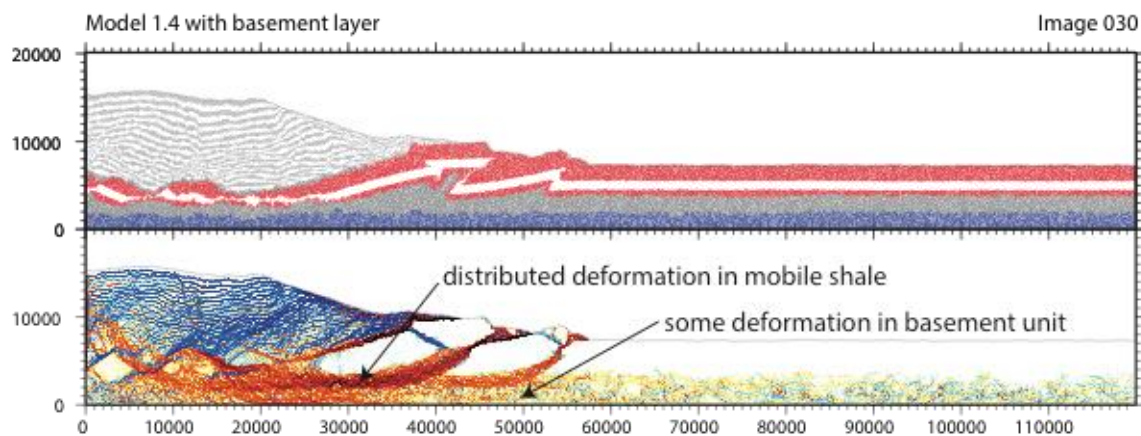
Figure 3.19 - Model 1.4 with basement. This model has the same configuration as model 1.4 except instead of a smooth basal boundary condition an additional (dark blue) layer of particles forms a basement layer in the model. These particles are bonded together at high bond strengths to minimize deformation; in the lower plot (2_{nd} strain invariant) a zone of distributed deformation forms above the basement in the mobile shale layer.

3.7.2. Stress fields and controls on structural vergence

All of our models exhibited both forethrusts and backthrusts, similar to the occurrence of such dual vergence in the Niger Delta outer fold and thrust belt. The dual vergence is enabled by mechanical decoupling of the predelta layer from the weak mobile shale, which allows for the development of nearly horizontal σ_1 in the pre-delta layer in front of the sediment wedge. An approximately horizontal σ_1, favors similar ramp angles for forethrusts and backthrusts so that they both accommodate the same amount of horizontal shortening for a given increase in gravitational potential energy (Dahlen, 1990). This rotation of σ_1 (Figure 3.17) is thought to be due to a basinward "push" created by updip extension along normal faults. This supports the statement by Corredor et al (2005) that backthrusts are formed in the northern lobe of the Niger Delta where σ_1 is horizontal.

Even in model 3.1, where the bathymetric slope was tilted 3°, the tilt was not enough to influence significantly the direction of σ_1, which was still subhorizontal, and not parallel to the basal slope, indicating that backthrusts are still capable of forming, even though there were only forethrusts formed in this model. Replicates of model 3.1, with different particle configurations, did form some backthrusts, similar to Figure 3.14. Therefore, the rotation of σ_1 during shortening creates a stress field where forethrusts and backthrusts are equally likely, and the distinct particle configuration determines which type of thrust will form at a given location.

Stress rotation to subhorizontal did not occur in the weak mobile layer, where σ_1 is more randomly oriented. As particles in the mobile shale are not bonded together, the domain has little cohesion, and therefore less ability to transmit stress (Figure 3.17). The

weak pre-delta layer appears to be necessary component for defining the weak "base"

enabling dual verging toe thrusts, acting as a stress guide that transfers stress from the

updip normal faults to the toe thrusts.

3.7.3. Strain

According to Morley et al (2011), the degree of extension and contraction in a linked

system are expected to be approximately equal. They also note that quantifying contraction

is difficult in young, poorly lithified sediments, and that sediment compaction and

dewatering may play a significant role.

However, we are able to explicitly quantify shortening in our models. We found that

the amount of shortening varies widely based on position. Figure 3.20 shows the

cumulative strain analyzed for three different locations in model 1.7. To get the amount of

shortening in the model, we found the positions of five particles grouped in locations on

either side of the final extensional zone (D1'), the thrust belt (D2'), and in front of the thrust

belt (D3'). We then found the original positions of these particles before the start of the

simulation (D1, D2, and D3). Ignoring any vertical changes in the positions of the particles,

we calculated the average changes in length of D1 to D1', D2 to D2', and D3 to D3'.

Underneath the sediment wedge, the pre-delta (red and white) unit has undergone about

5.6 km of extension, while in the fold and thrust belt, the total shortening is about 3.0 km of

contraction. Finally, out in front of the toe thrusts, the pre-delta layer has undergone about

0.3 km of contraction. Surprisingly, almost twice as much upslope extension occurs as

downslope contraction, a discrepancy that must be taken up through compaction and

porosity reduction within the system represented by particle rearrangement in our models.

Similar results were found in the Orange Basin, South Africa, where 24 km of extension and 16km of shortening were measured based on large scale seismic structures (Morley et al, 2011). Measurements of layer parallel shortening in tectonic forelands has been found in the Canadian Cordillera and in Venezuela (Roure, et al, 2010), indicating that penetrative strain in front of a thrust wedge occurs in both tectonic and gravitational systems.

These models and observations suggest that the Niger Delta and similar areas can't be restored using line length balancing algorithms, which do not account for this distributed compression in front of the toe thrusts. In addition, formations and reservoirs in the contractional zone of the gravitational system should be expected to be over-compacted due to distributed horizontal strain. Even locations on the current thrust structures would likely have seen penetrative deformation when the thrust belt was advancing. This agrees with work done by Kocher (Shell, pers. comm.) who found over-compaction in reservoir sands due to horizontal shortening, which in turn was caused by deltaic loading and gravity sliding.
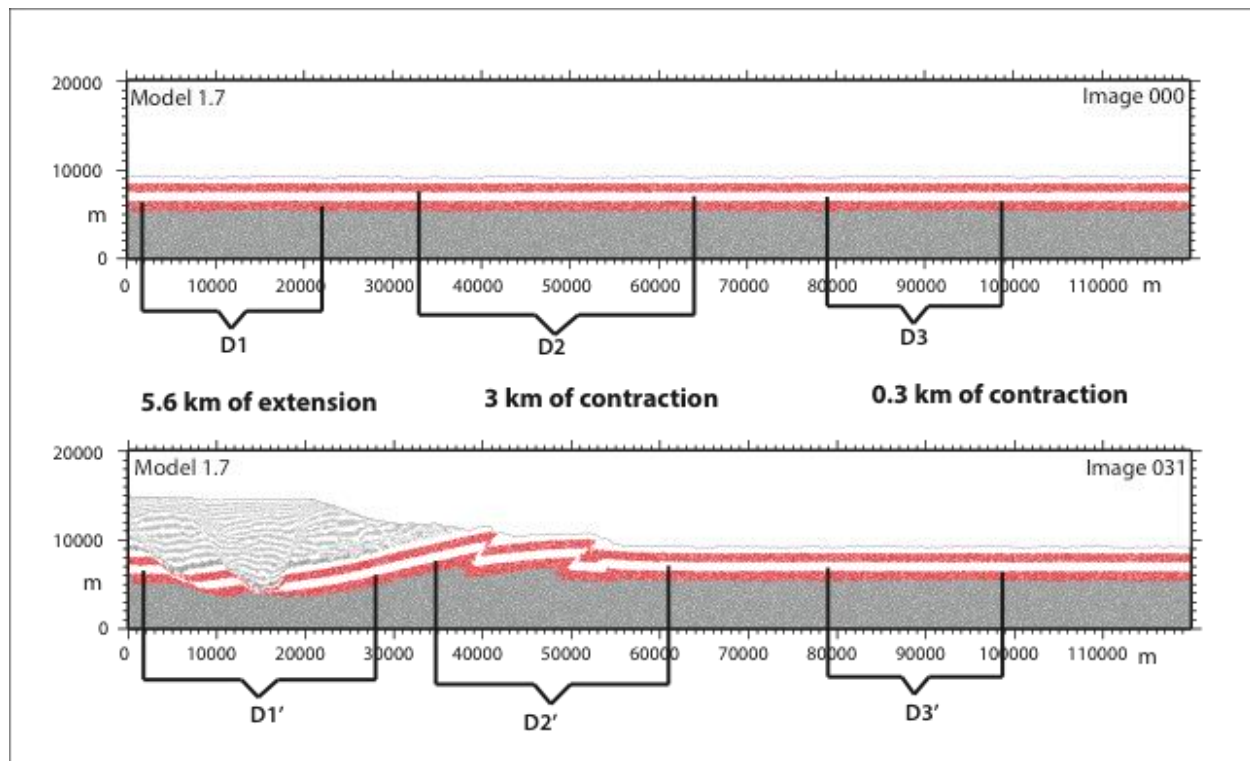
Figure 3.20 – Strain in Model 1.7. The initial (lower plot) and final (upper plot) particle configurations for Model 1.7. D1' is the line length of the extensional region.D1 marks the original distance at the start of the simulation between the particles in D1'. D2' spans the length of the fold and thrust belt, while D2 is the distance between the same particles in at the start of the simulation. D3' is an arbitrary length out in front of the fold and thrust belt, with D3 marking the original length of that line, based on particle positions.

3.8. Conclusions

Our simulations successfully formed linked systems of updip extension and downdip compression, driven by sediment loading on a weak substrate. Stress is effectively transmitted from updip to downdip through the pre-delta layer, with σ_1 rotating as it does to become favorable for dual thrust vergence, supporting Corredor et al (2005) description of stress in the northern lobe of the Niger Delta. This stress rotation is thought to be due to

a basinward "push" created by updip extension along normal faults. This rotation of stresses does not occur in the mobile shale layer.

Models with a thin mobile shale layer and a smooth basement preferentially form a very thin sliding surface at the base of the model, which connects strain in the extensional and compressional regions. In contrast, models with thick mobile shale, or a rough basement exhibited distributed strain occurring throughout the mobile shale layer, without concentrating into a décollement surface at the top or bottom of the mobile shale. This zone of strained mobile shale was usually initiated by a regional normal fault, and connected normal faults and thrust faults, as well as propagating in the mobile shale out in front of the active toe thrusts. Discrete thrust faults within the stronger, bonded pre-delta layer became broader regions of distributed strain as they propagated down into the mobile shale. Our models suggest that deformation in the mobile shale region will span the thickness of the mobile shale unless some mechanical contrast exists within the shale to localize strain. In model 5, where the stratigraphy is thinned basinward, this zone of strained mobile shale propagates up to 60 km in front of the developing fold and thrust belt, and initiates a second thrust belt.

Quantifying the amount of extension and contraction in three sections of model 1.7 demonstrated that the thrust fault zone undergoes about half as much strain as is accommodated in the extensional zone (Figure 3.20). Therefore, much of the contraction in the system is distributed throughout the model domain, including out in front of the thrust belt, similar to layer parallel shortening measured in tectonic forelands. This is

accommodated by particle rearrangement in our models, but represents processes like compaction and dewatering in natural systems.

These numerical models are simplified, and do not include deposition of synkinematic sediments over the fold and thrust belt(s), which occurs in the Niger Delta. However, our models successfully form a fold and thrust belt in front of the extensional zones, and the model with a progressively thinned mobile shale layer shows the start of a second, more distal fold and thrust belt that could represent the outer fold and thrust belt of the Niger Delta.

Chapter 4

Galicia Bank ocean-continent transition zone:
New seismic reflection constraints

4.1. Abstract

The West Iberia continental margin is a type locale for magma-poor rifting, and studies there have been instrumental in changing the classical view of the ocean-continent transition (OCT) from a discrete boundary juxtaposing continental and oceanic crust, into a more complicated zone of varying width that can include exhumed mantle. This study examines two new seismic lines in the Galicia Bank area extending west of the Peridotite Ridge, showing high resolution images of five new ridges. These ridges could be hyperextended continental crust, exhumed continental mantle, or rough ultra-slow spreading oceanic crust. There are no tilted fault blocks with pre-syn rift stratigraphy that would indicate continental crust. There are also no faults indicating mid-ocean spreading with seismic layer stratigraphy indicating normal oceanic crust. Therefore, it is likely the western ridges are also made of serpentinized mantle, defining a wide OCT similar to the southern Iberia abyssal plain.

4.2. Introduction

The West Iberia continental margin is a type locale for magma-poor rifting, and has been the subject of several seismic studies (GP (Groupe Galice, 1979), Lusigal (Beslier et al, 1993), ISE (Sawyer et al, 1997), Discovery 215 (Discovery 215 Working Group, 1998)), four Ocean Drilling Program (ODP) expeditions (legs 103 (Boillot et al, 1987), 149 (Sawyer et al, 1994), 173 (Whitmarsh et al, 1998), and 210 (Tucholke et al, 2004)), as well as other geophysical and submersible studies (Figure 4.1, Figure 4.2). These studies have been instrumental in changing the classical view of the ocean-continent transition (OCT), previously inferred to be a discrete boundary that juxtaposed continental and oceanic crust, into a more complicated zone varying width that includes exhumed continental mantle rocks often forming one or more semi-continuous peridotite ridges. The OCT on the Iberia margin is characterized by unusually high seismic velocities (>7.3 km/s) near the basement surface, weak and discontinuous magnetization, and the peridotite ridge(s) (Henning et al, 2004; Peron-Pinvidic et al, 2007). It extends up to 170 km wide in the Southern Iberia Abyssal Plain (SIAP) in the south and narrows to about 10 km wide in the northern Galicia Bank (Dean et al, 2000). The OCT zone is defined to be bounded on the east by the furthest extent of continental crust, observed on seismic profiles as fault-bounded rotated blocks. The western boundary of the OCT is defined as the first occurrence of oceanic crust, interpreted based on seismic refraction profiles (Whitmarsh et al, 1996; Dean et al, 2000) or seafloor magnetic anomalies (Pickup et al 1996; Sibuet et al, 2005; Sibuet et al, 2007; Hopper et al, 2004). This study presents new seismic reflection

data of the interpreted Galicia Bank OCT to further characterize and constrain the nature of the transition zone.

To the south, in the wide SIAP transition zone, the basement topography includes multiple margin parallel overlapping ridges interpreted to be made of serpentinized peridotite, two of which have been drilled (Dean et al, 2000; Henning et al, 2004). The narrower Galicia Bank transition zone has been interpreted to contain a single peridotite ridge with oceanic crust immediately west of the ridge (Beslier et al, 1993; Whitmarsh et al, 1996). However, the seismic profiles collected on the Galicia Bank margin all terminated at the Peridotite Ridge and did not extend into the interpreted oceanic crust domain. This study examines two new seismic lines in the Galicia Bank area, extending to the west of previous studies, which image the crust west of the Peridotite Ridge, in order to examine characteristics relevant to locating the OCT, as well as to find the contact between the zone of exhumed mantle and that of oceanic crust. By constraining and characterizing the OCT in this unique locale we can gain deeper understanding of the breakup of continents as a gradual or an abrupt process, which will tell us about the mechanics of how plates break apart, a first-order plate tectonic process.

4.3. Evolution of the Iberia margin

4.3.1. Geologic Setting

The Iberia and Newfoundland margins are conjugate, magma-poor and sediment-starved passive margins that developed from the Late Triassic to Early Cretaceous rifting

and separation of the North America and Europe/Iberia plates. The rifting of the margin is generally broken up into at least two different phases of extension: an older Late Triassic phase and a younger Late Jurassic to Early Cretaceous phase (Peron-Pinvidic et al, 2007; Tucholke et al, 2007). The earlier phase involved the formation of large and deep, but widely distributed, fault-bounded basins such as the Jeanne d'Arc, Lusitanian and Galicia Interior Basins, created in an environment variously described as pure shear (Peron-Pinvidic et al, 2007), stretching (Lavier and Manatschal, 2006), or wide rifting (Brun, 1999; Hopper et al, 2004).
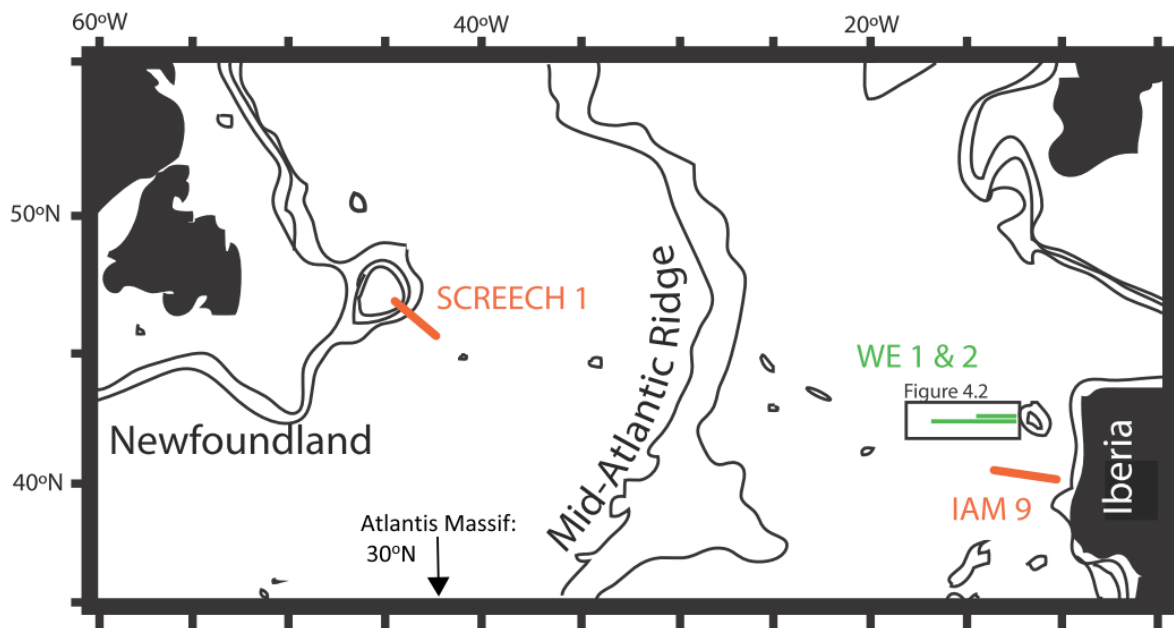
Figure 4.1 Iberia – Newfoundland conjugate margin. Locations of older seismic profiles IAM 9 (Dean et al, 2000) and SCREECH 1 (Hopper et al, 2004) are shown in orange on opposite sides of the conjugate margin. Green lines indicate the position of the new profiles described in this study. Modified from Hopper et al, 2004.

Figure 4.2 Location map of Galicia 3D Seismic Experiment, showing the 3D survey area (black box) and western extension profiles (green lines) overlying the bathymetry map. Older GP101 (Reston et al, 2006) and ISE1, 4, 5, 6 (Henning et al, 2004) also shown (orange and tan, respectively). Location shown in Figure 4.1. (Figure on next page)

Galicia 3D Seismic Experiment
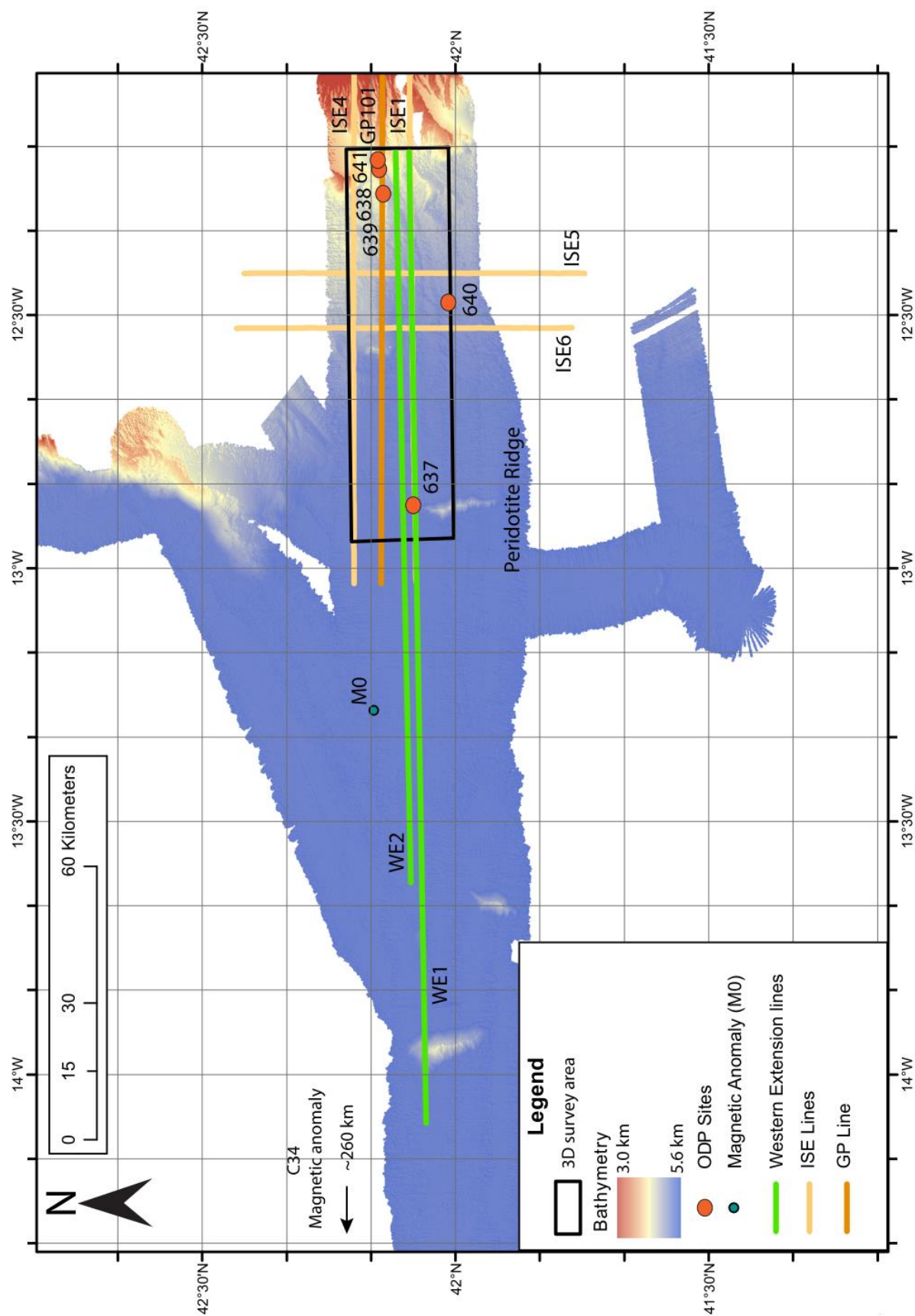
The younger phase was characterized by progressive localization of extension in the more distal parts of the margins prior to seafloor spreading. The continental crust was thinned to less than 10 km, and broke into distinct blocks along west dipping normal faults. These normal faults merged with the underlying S-reflector. The S-reflector is a prominent, bright reflector located at about 8 km below sea level, interpreted to be a detachment surface that separates overlying highly faulted continental crust from underlying serpentinized peridotite (Reston et al, 1996). Once the continental crust thinned to zero, subcontinental mantle was exhumed in the OCT (Peron-Pinvidic et al, 2007; Borgmeyer et al, 2010). The age of then final breakup of the continents and onset of oceanic spreading and generation of oceanic crust is still debated. Whitmarsh and Miles (1995) and Russell and Whitmarsh (2003) correlate the breakup with oceanic magnetic anomaly M3, suggesting an age of 128 Ma. Wilson et al (2001) suggests an age of 140–134 Ma based on drilling data. Tucholke et al (2007) and Peron-Pinvidic et al. (2007) proposed an age of 112 Ma based on seismic stratigraphy, and Dean et al (2007) correlate the breakup with magnetic anomaly M0 (Figure 4.2) suggesting an age of 125 Ma. Despite the uncertainty over the timing of the breakup, it was followed by a period of slow or ultra-slow mid-ocean ridge spreading, creating initial oceanic crust that is thinner (3-4 km) than normal oceanic crust along parts of the conjugate margins (Dean et al, 2000; Hopper et al, 2004; Sibuet et al, 2007). The first undisputed magnetic anomaly occurs along the ocean side of the Cretaceous Normal Superchron, anomaly C34, dated to 83 Ma, where seafloor spreading was well established (Bronner et al, 2011). C34 is approximately 260 km west of the Western Extension 1 profile.

4.3.2. Geologic and seismic background

Traditionally, the OCT is considered to be narrow in the Galicia Bank area; oceanic crust has been interpreted to occur on the western side of the Peridotite Ridge. Whitmarsh et al (1996) analyzed OBS (ocean bottom seismometer) data collected off the Galicia Bank margin in 1987, along an E-W transect coincident with seismic profile GP101 (Figure 4.1). Five approximately N-S refraction profiles were used to constrain a velocity model along GP101 (Figure 4.3). Within this model, the Peridotite Ridge represents the top of a 60 km wide, oval body of serpentinized peridotite that extends on either side beneath thinned continental crust on the east (Figure 4.3, profile 7E) and thin oceanic crust on the west (Figure 4.3, profile 7W), with increasing seismic velocities with depth (due to decreasing degrees of serpentinization). The crust west of the Peridotite Ridge is interpreted to be oceanic crust (Figure 4.3, profile 8), although with a thickness of 2.5-3.5 km rather than the normal 7 km. The velocity structure of the 2.5 to 3.5 km thick oceanic crust is similar to that of the crust immediately to the east of the ridge, but is attributed to thin oceanic crust rather than thinned continental crust (Whitmarsh et al, 1996).

Further south, in the SIAP, the ocean-continent transition zone is wider, and serpentinized peridotite has been found at multiple ridges during ODP legs 149 and 173. It is also modeled to be present in relatively flat stretches of basement west of the thinned continental crust (Figure 4.4). Dean et al (2000) analyzed OBS data collected in the SIAP in 1995, with the main E-W line coincident with a previous seismic reflection profile IAM-9, and to the south of five ODP sites. The OCT is modeled by a largely laterally continuous velocity model, although there is an additional velocity layer beneath the peridotite ridges

not found in the flatter portions of the OCT. However, in both areas the top of the basement has velocities similar to that of the base of the overlying sediments, 4.3-5.2 km/s, and increases with depth to 7.0-7.3 km/s at steep velocity gradients, due to the effects of decreasing serpentinization (Dean et al, 2000). West of the peridotite ridges, the basement is modeled with an initial velocity of 4.5 km/s, increasing with depth to 6.5 km/s. A second velocity layer was modeled with velocities of 6.7-7.2 km/s. Dean et al (2000) describe these two velocity layers west of the peridotite ridges to be similar to normal Atlantic oceanic crust layer 2/layer 3 velocity structure. This boundary is also close to the M3 magnetic anomaly, which Whitmarsh and Miles (1995) and Russell and Whitmarsh (2003) believe to indicate the first onset of sea floor spreading. Dean et al (2000) also indicated that the exact transition from the OCT serpentinized peridotite to oceanic crust (which is full thickness here unlike along GP101 in the Galicia Bank) is poorly constrained, and is likely a gradual transition rather than a sharp boundary.
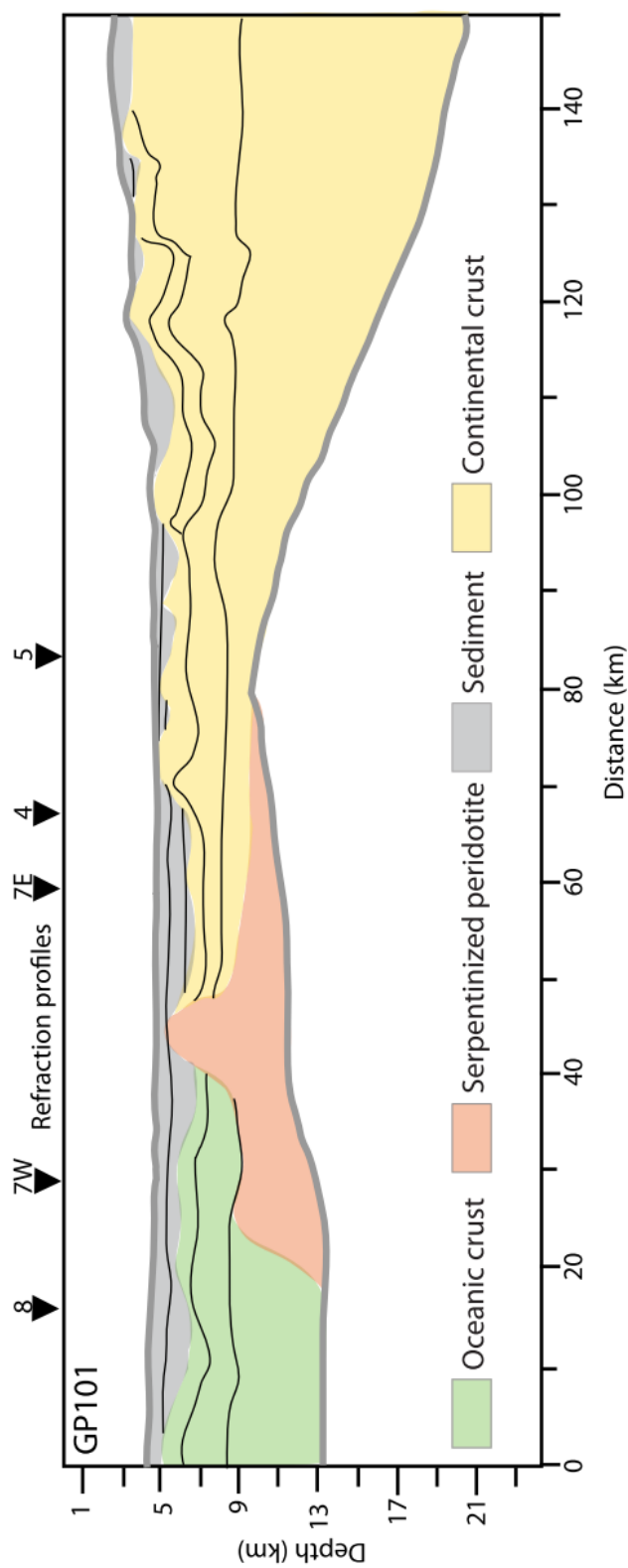
Figure 4.1 Refraction line 6 / GP101 crustal model. Transition from continental crust to exhumed mantle to thin oceanic crust. Triangles indicate locations of N-S refraction profiles. See Figure 4.2 for location. Modified from Whitmarsh et al (1996).
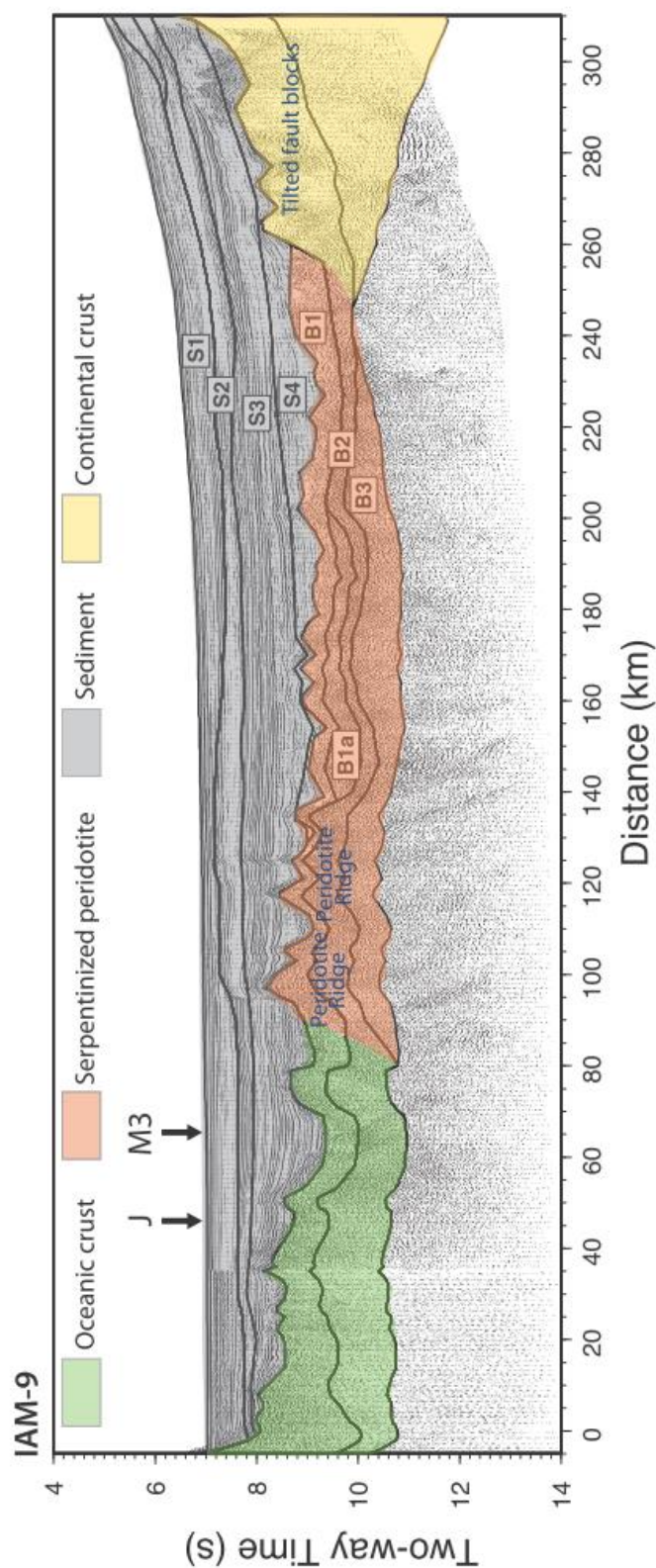
Figure 4.2 Interpreted seismic reflection line IAM 9. Continental crust, the wide zone of exhumed mantle including two peridotite ridges in the west, and the transition to oceanic crust are shown. J and M3 indicate magnetic anomalies, with J being equivalent with M0 in the Galicia Bank area (Bronner et al, 2011). The steep upward slope of the oceanic crust on the west end of the line is the flank of an emergent seamount imaged on the subsequent refraction cruise, but not the reflection profile. See Figure 4.1 for location. Modified from Dean et al (2000).

On the other side of the Atlantic Ocean, along the conjugate margin off Newfoundland, a seismic survey was conducted in 2000 to acquire data at key locations relative to the main geophysical and drilling transects off Iberia. SCREECH-1 is a seismic reflection and refraction profile conjugate to GP101 in the Galicia Bank (Hopper et al, 2004) (Figure 4.5). It was previously hypothesized that the OCT in Newfoundland would be similar to that seen in Galicia Bank and the SIAP, containing a transition zone of serpentinized peridotite between thinned continental mantle and oceanic crust (Dean et al, 2000). However, Hopper et al (2004) observed a distinct boundary, rather than a transition zone. Oceanic crust was interpreted immediately seaward of thinned continental crust, and characterized by a series of domino-style rotated blocks bounded by evenly spaced normal faults dipping 45° seaward. Although the crust is only 3–4 km thick, the OBS data was best fit by modeling a typical oceanic layer 2 layer 3 structure (Funck et al, 2003). This is also supported by the seismic reflection data (Hopper et al, 2004), which shows a volcanic stratigraphy similar to the tilted fault blocks imaged at the abandoned spreading center in the Labrador Sea (Srivastava and Keen, 1995). So although the OCT along the western conjugate margin lacks the exhumed mantle seen in Iberia, both margins support the interpretation of an early period of ultraslow spreading. Thin oceanic crust was suggested by Whitmarsh et al (1996) along GP101, similar to what is currently forming at the Southwest Indian and the Gakkel ultraslow spreading ridges, which have average crustal thicknesses of 3.8 km and 4 km, respectively (Hopper et al, 2004).
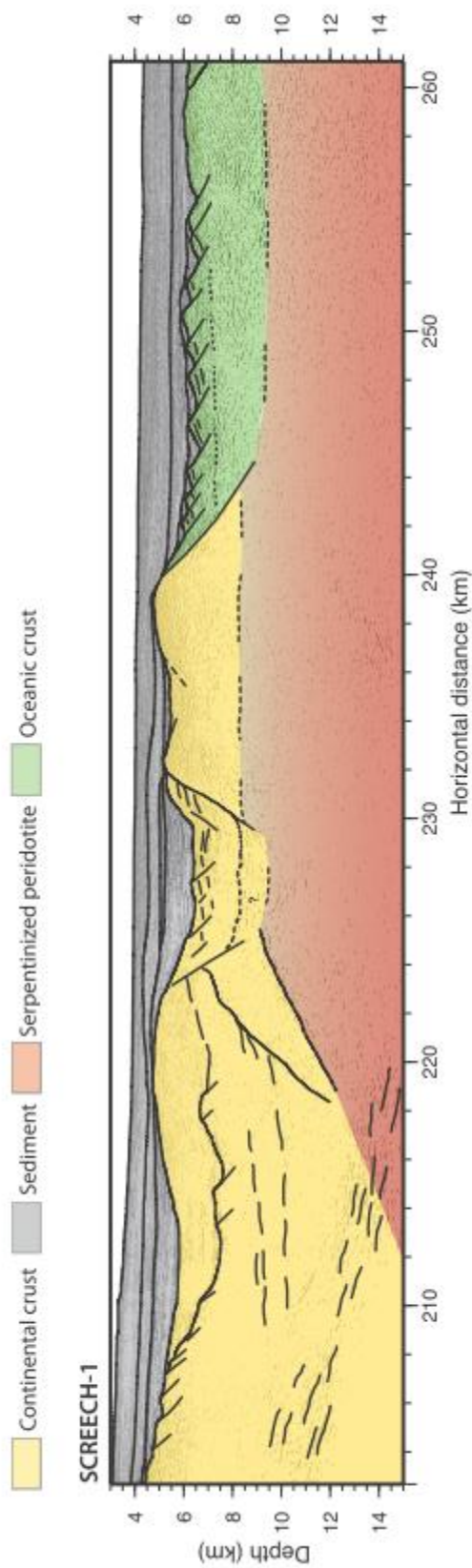
Figure 4.3 Interpreted seismic reflection line SCREECH 1. Conjugate with ISE 1. The continental crust transitions to oceanic crust along an abrupt fault contact; while serpentinized peridotite is interpreted below the thin continental and oceanic crust, it is not present along the basement surface. See Figure 4.1 for location. Modified from Hopper et al (2006).

4.4. Seismic dataset

In an effort to extend our understanding of the Iberia margin, the Galicia 3D Seismic Experiment involved collecting a 3D reflection seismic survey and wide-angle seismic survey of the Deep Galicia Basin (Figure 4.2). The seismic reflection data was acquired by the *RV Marcus G. Langseth* between 1 July and 2 August, 2013. The *Langseth* is owned by the U.S. National Science Foundation and operated by Lamont Doherty Earth Observatory of Columbia University. The primary acquisition of this cruise was a 3D seismic reflection survey covering a 65 km (East-West) by 20 km (South-North). In addition to the 3D seismic volume, the *Langseth* also acquired two single sail lines, forming extensions west of the 3D box. One of those extensions was preplanned (Western Extension 1), extending ~90 km west of the 3D box. The other extension involved ship maintenance while moving to the West of the 3D box, followed by acquiring a reflection sail line back to the 3D box (Western Extension 2). Western Extension 2 was 4.8 km north of Western Extension 1, and extended 50 km west of the 3D box.

The *Langseth* 3D acquisition configuration included four seismic streamers of ~6 km length, towed 200 m apart, with channels spaced at 12.5 m. Each streamer has 468 channels and the total of four streamers has 1,872 channels. The channels were towed 15 m deep. The *Langseth* 3D source configuration was two alternating source arrays, deployed 100 m apart, and deploy2ed at 12 m deep. Each source array consisted of 20 airguns of varying sizes, making a total of 3,300 cu. in. When using the four streamers and the dual gun arrays, the ship was able to record 8 adjacent CMP lines spaced 50 m apart and

covering a sail line 400 m wide. The navigation system was able to precisely locate each gun array center and each channel center at every shot.

Although these extensions were much like traditional 2D seismic profiles, we can also treat the lines as very narrow 3D seismic volumes (one sail line, 400 m wide). Treating them in this way, we can create a 3D "Inline" which is a truly straight line collecting all appropriate combinations of midpoints. This Inline forms a true 2D profile extracted from the 3D data.

We note that there were 4 flaws in the Western Extension 1: Three were caused by approaches of whales (18 km, 50 km, and 78 km), and one was caused by a brief change of parameters while entering the 3D seismic volume (88 km). In the case of whales we turned off the full seismic source arrays, and continued firing only with a very small, 40 cu. in., source.

These data have been processed by selecting a single Inline profile, sorting to CDP's (Crosslines in 3D terminology), spherical gain correction, velocity analyses at 1 km spacing, normal move out, alpha-trim stacking at 20 %, and Post-stack Kirchoff Time Migration. These were followed by depth conversion based on smoothed interval velocities (Figure 4.6b, e).

4.5. Results

The two margin-perpendicular Western Extension (WE) profiles (Figure 4.6) extend 120-160 km across the Galicia basin. These two profiles image a series of landward-rotated, normal-fault-bounded blocks of continental crust and sediments, underlain by the

S-reflector. The continental crustal blocks thin progressively westward until they terminate

at the Peridotite Ridge, which exposes continental mantle. This area has been described in

detail by Reston et al (1996), Henning et al, (2004) and Borgmeyer (2010). Borgmeyer

(2010) identified 6 continental blocks (A-G) on the E-W ISE seismic profiles (Figure 4.2), 5

of which are in our study area. A possible additional block may exist in the basin separating

the continental crust and exhumed mantle (Figure 4.6c, f, dashed line). These blocks are

bounded by west-dipping normal faults that merge with the underlying S-reflector where

visible. The S-reflector occurs as a prominent, bright reflector at about 8 km below sea

level, interpreted to separate overlying highly faulted continental crust from underlying

serpentinized peridotite (Reston et al, 1996; Reston et al, 2007). The S-reflector is also

thought to be a detachment fault, branching on its eastward end into one or two breakaway

faults that merge upward with the block bounding normal faults (Reston et al, 1996).

Adjacent to and immediately west of the continental blocks is the Peridotite Ridge, a

N-S trending ridge that is about 3.5 km tall in the southern part of the study area, extending

above the post-rift sediment, and gradually decreases in height to become buried by

sediment to the north. West of the Peridotite Ridge is another sequence of ridges, varying

in height, width, and shape. These two western extension profiles provide the first detailed

look at these western ridges, previously interpreted to correspond to oceanic crust. The

ridges include short (about 1 km), asymmetric and angular blocks similar to the

continental blocks or to fault bounded oceanic crust (Srivastava and Keen, 1995), as well as

taller symmetric and relatively smooth ridges similar to the Peridotite Ridge. Thus, their

initial identities are unclear. The continental blocks and western ridges have been

correlated between the two profiles, although there is variation in the height and width of some of the blocks/ridges, which will be discussed in the next section in order to establish their structure and composition.

4.5.1. Western Extension 1

Western Extension Line 1 (WE1, Figure 4.6d, e, f) is the southern dip profile in this study. It coincides with the western part of Henning et al's (2004) ISE-1 profile, but extends 85 km farther west, for a total of 160 km. It also very close to ODP Site 637, which penetrated the Peridotite Ridge.

At the eastern end of WE1, there are five continental crustal blocks bounded by four west dipping normal faults. The middle block, E, is draped with syntectonic sediment wedges and lacks a distinct peak; it is half the height of the adjacent blocks (Figure 4.6f). The faults bounding this block and those further west, sole into the S-reflector. The S-reflector is not observed under the eastern block C, which has a boundary fault that terminates in the crust. The S-reflector dives under the deep basin separating the continental crust and the Peridotite Ridge. It merges with the edge of the basin, and then disappears, and no similar detachment reflectors are seen on the western side of the Peridotite Ridge. The tip of the Peridotite Ridge just reaches the seafloor, and it is very symmetric with no distinct internal structure. It is flanked on either side by deep basins, which contain a very strong package of reflections at 8500 ms, continuous across the respective basins (Figure 4.6d).

a) Western Extension 2 — Area of 3D survey — Continental blocks — Figure 4.7a — Figure 4.8a

Two-way time (ms)

b) m/s — 2000, 4000, 6000

Two-way time (ms)

c) Peridotite Ridge — s-reflector — Vertical exaggeration 3:1 — C, D, E, F, G, 1-2, 3a

Depth (km)

Distance (km)
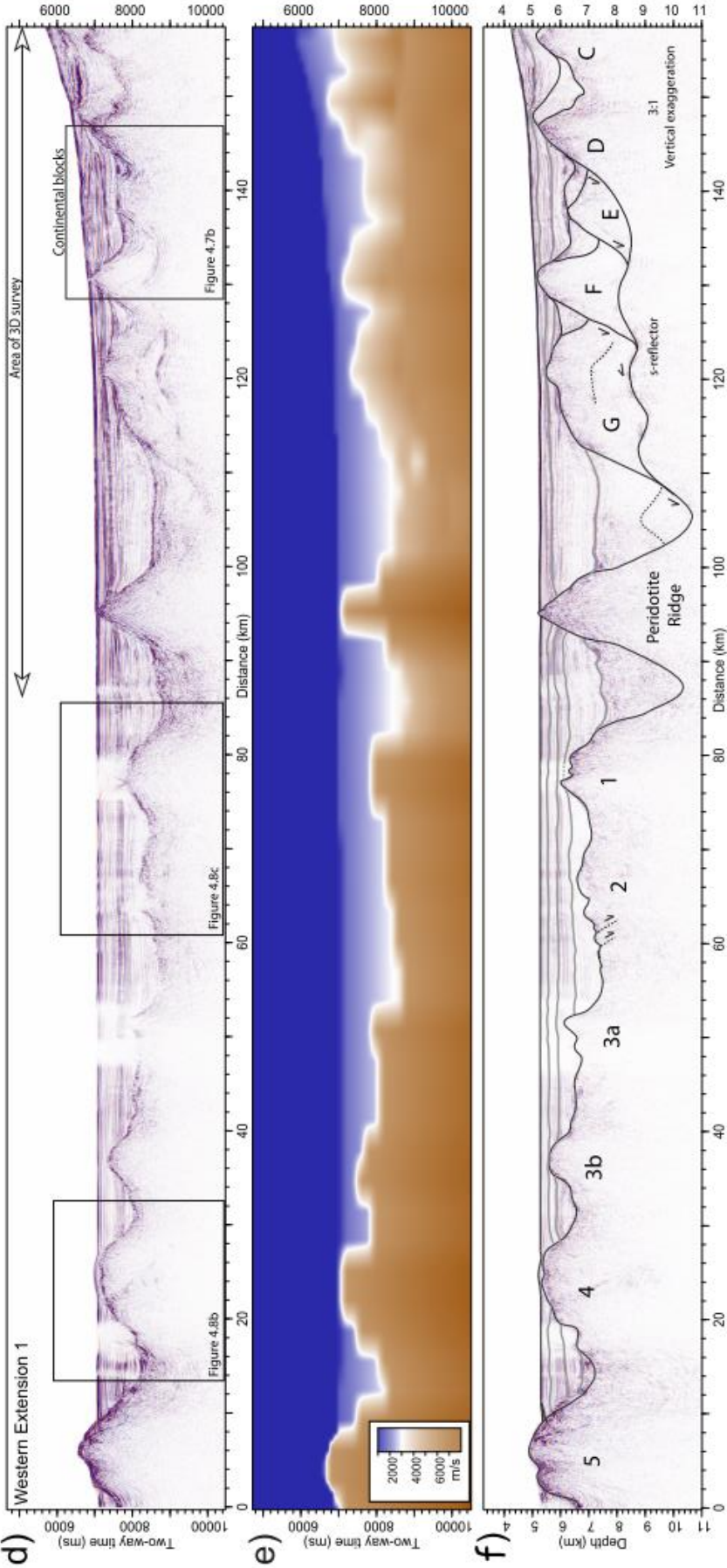
Figure 4.4 Western extension profiles 1 and 2. a) Time section of WE2, b) velocity model for WE2 and c) interpreted depth section (VE 3:1). d) Time section for WE1 and e) velocity model for WE1 and f) interpreted depth section (VE 3:1). Five continental blocks are interpreted on the eastern portion of both profiles, thinning westward and underlain by the bright S-reflector. The Peridotite Ridge is located west of the continental crust, and flanked on either side by deep basins. Further west are 2 (WE2) and 5 (WE1) new ridges, see discussion for interpretations. See Figure 4.2 for locations.

Westward, there is a series of five ridges that progressively become taller, until

ridge 5 is emergent above the post-tectonic sedimentation. Ridge 1 is half as tall as the

Peridotite Ridge, but otherwise very similar: symmetric and without internal structure.

Ridge 2 is separated from ridge 1 by a very shallow, perched basin. Ridge 2 is asymmetric,

with a longer western flank and the basement surface is rough and angular, possibly due to

small surface faults or fractures (Figure 4.6f). It is also separated from ridge 3 by a shallow

basin. Ridge 3 is divided into two peaks, 3a and 3b. The top of ridge 3a is obscured by a

data gap, but in general it is similar to ridge 2, with a rough angular surface. Ridge 3b

however, is more symmetric and has a smoother surface. The basement crust thickens

westward, so that the bottom of the basin between 3b and ridge 4 is at the same level as the

top of ridges 1 and 2. Ridge 4 is 12 km wide and almost reaches the seafloor; its top is

covered by a very thin layer of sediment (Figure 4.6d). It is symmetric and has few internal

reflections; the few that are present are chaotic and discontinuous. The basin between

ridges 4 and 5 is deeper than the one to the east, though the ridge is also taller. The whole

ridge is largely symmetric, although the western flank of the emergent section is slightly

concave, possibly due to erosion or mass wasting.

4.5.2. Western Extension 2

WE2 (Figure 4.6a, b, c) is approximately 4.8 km north of WE1, and is 40 km shorter,

with a total length of 120 km. It includes the same five continental crustal blocks described

for WE1 on its eastern end, although block E is more prominent along this transect, with a

distinct peak. It also contains a thick coherent pre-to-syntectonic wedge. The S-reflector is

also present under the three western-most blocks. The S-reflector merges with the faults

bounding blocks E and D that define forming breakaway faults (Figure 4.6c). Another difference between WE1 and WE2 is found in block G; this block is coherent on WE1, but its western flank on WE2 has been down-dropped into the basin along another normal fault. The Peridotite Ridge is continuous and similar along strike, although it is buried by sediment on WE2. The flanking basins are also present on the northern profile, with the same package of strong reflectors at 8,500 ms (Figure 4.6a), indicating the source of the reflectors is widespread and the basins filled uniformly in the N-S direction.

On the western flank of the Peridotite Ridge on WE2, ridges 1 and 2 form one 20 km wide ridge that is strongly asymmetric, with a steep east flank and a shallow western one (Figure 4.6a). The basement surface is similar to that of the southern ridge 2 i.e., very angular. The only other ridge present on the profile corresponds with ridge 3a. Ridge 3a has steep flanks and a sharp peak, and normal faults occur in the sediments above it, possibly due to post-tectonic differential sediment compaction. The overall height of the basement increases westward, similar to WE1. The profile does not extend to the larger ridges 4 and 5, making it unclear whether they are in fact N-S trending continuous ridges similar to the Peridotite Ridge, or more isolated seamounts. Based on the bathymetry (Figure 4.2) the western ridges appear to be oblong, and to trend N-S, although most of the emergent part of the ridge is south of WE1. But ridge 5, like the Peridotite Ridge, may also become buried further north.

4.6. Discussion and Interpretations

The main purpose of collecting the WE profiles was to image the crust west of the Peridotite Ridge in order to identify and characterize the contact between the serpentinized peridotite and oceanic crust. In addition, within the continental crust domain, the two WE profiles support earlier interpretations based on the GP and ISE data sets. They also improve the resolution to define the termination of the S-reflector, showing that the S-reflector dips westward under the eastern flanking basin of the Peridotite Ridge (Figure 4.6), rather than going over the Peridotite Ridge, as interpreted by Borgmeyer et al (2010).

To the west of the Peridotite Ridge the new profiles show five basement ridges, with a wide range of shapes and dimensions. Beslier et al (1993) and Whitmarsh et al (1996) placed oceanic crust immediately west of the Peridotite Ridge, although drilling expeditions in the SIAP have shown that the transition zone is locally much wider than previously expected. Therefore, there are three possible origins for the western basement in our study area: it could be (1) hyperextended continental crust, through which the Peridotite Ridge penetrated, (2) additional ridges of exhumed continental mantle similar to the Peridotite Ridge, or (3) oceanic crust formed at ultra-slow / slow spreading centers. Each hypothesis will be explored in the following sections.

4.6.1. Continental crust hypothesis

Generally, continental crust is interpreted to be thinned to zero thickness before the exhumation of continental mantle (Peron-Pinvidic et al, 2009). However, along the SIAP

near the Hobby High (just north of IAM-9, Figure 4.1) exhumed mantle has been interpreted between continental blocks: near the Hobby High Detachment fault (HHD), the breakaway fault is interpreted as concave downward, cutting into the mantle, enabling the overlying crustal block to slide westward as an allochthon on exhumed mantle (Peron-Pinvidic et al, 2007). Where observed on seismic profiles (Pinvidic et al, 2007; Reston et al, 2007; Borgmeyer, 2010), continental crustal blocks are generally angular, having been cut and rotated by listric normal faults. They are also characterized by syn-tectonic sedimentary wedges and internal layering reflecting pre-tectonic strata (Figure 4.7a, b). In addition, the S-reflector and HHD detachments demonstrate strong impedance contrasts between continental rocks and serpentinized mantle. Thus, allochthonous continental blocks should be bounded at the base by a visible seismic reflector (Manatschal et al, 2001). None of the five western ridges in WE1 and WE2 display these characteristics. Although ridge 1-2 in WE2 is somewhat angular, it has little to no internal structure in our seismic data, and there are no obvious block bounding faults or syn-rift wedges. No buried detachment faults are found west of the Peridotite Ridge. Therefore it is unlikely that any of the ridges consist of continental rocks.

4.6.2. Ultra-slow oceanic crust hypothesis

The traditional interpretation for the Galicia Bank is that oceanic crust occurs just west of the Peridotite Ridge, based on refraction data (Whitmarsh et al, 1996). However, according to Dean et al (2000) the transition is likely to by gradational, and there may not be an abrupt change in the velocity profile. Along the IAM-9 profile, there is a seamount on the western edge of the profile. The two OBS instruments closest to it recorded velocities

that matched well with Atlantic oceanic crust velocities. The profile of this seamount, an

emergent largely symmetric ridge (Dean et al, 2000), looks similar to ridges 4 and 5. But

overall, the bathymetry is quite different; profile IAM-9 intersects a circular peak whereas

ridge 5 intersected by WE1 (Figure 4.2) appears to be highly elongate. This morphology is

unlike that of a volcanic seamount, suggesting a different origin for the ridge.
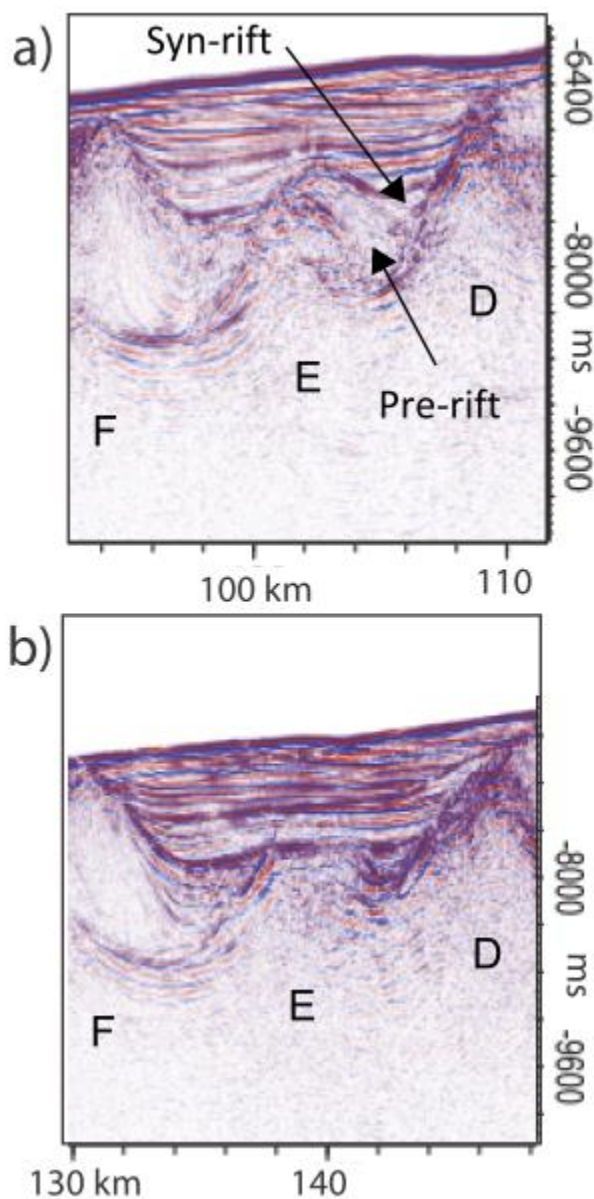

Figure 4.7 Continental blocks D, E and F. a) WE2 and b) WE1. Pre- and syn-rift sediments are labeled on block E in a). See Figure 4.6 for locations.

Both Whitmarsh et al (1996) and Hopper et al (2004, 2006) suggested that the interpreted thin crust between the OCT and full thickness oceanic crust on their respective sides of the conjugate margin was due to ultra-slow spreading, supported by current and extinct ultra-slow ridges. Other typical characteristics of ultra-slow spreading centers include rough basement topography, rotated blocks bound by normal faults, and highly varied refraction data showing complex layer thicknesses and velocities (Srivastava and Keen, 1995). The interpreted oceanic crustal regime on the profile from Newfoundland fits these specifications. For example, Figure 4.5 shows evenly spaced rotated and fault bounded blocks, as well as more varied but still angular topography further east. Supporting the case for oceanic crust in our area is the fact that magnetic anomaly M0 is located along ridge 2. This anomaly has been interpreted to define the start of oceanic crust (Figure 4.2) (Dean et al, 2000; Hopper et al, 2004). In fact, ridges 1, 2 and 3a bear some similarities to ultraslow oceanic crust. Both are quite angular and asymmetric, possibly due to fault rotation, although no faults are visible on our profiles. In addition, the top of the basement along and between these ridges is rough and jagged, with possible shallow normal faults (Figure 4.8a, c). Semi-chaotic reflectors under ridge 2 on WE1 also suggest the presence of volcanic strata as seen in Newfoundland and Labrador (Hopper et al, 2004; Srivastava and Keen, 1995). However, the wide, rounded and symmetric ridges 4 and 5 on WE1 are distinctly different. No similar features are seen in Newfoundland or in the Labrador extinct spreading center (Srivastava and Keen, 1995). They are within the range of heights and widths of typical seamounts, (Yang et al, 2013), but the elongate profile of ridge 5 in the bathymetry data is more reminiscent of peridotite ridges than rounded

seamounts. Therefore, the middle two to three ridges suggest the presence of oceanic crust, but the westernmost two ridges do not.

4.6.3. Exhumed mantle hypothesis

The presence of multiple overlapping peridotite ridges and a wide zone of exhumed mantle in the SIAP opens the possibility that similar features occur in Galicia Bank. It is possible that the transition zone in the northern section of the Iberia margin is also wider than previously predicted. The Peridotite Ridge in the Galicia Bank area has relatively steep flanks, dipping 20-28° in our two profiles. The ridge is also highly symmetric (Henning et al, 2004), with no internal reflections that would indicate layering. Ridges 3b, 4, and 5 are similar in their nature, although not quite as steep as the Peridotite Ridge. The steepest portions of their flanks dips 15-22°. They also do not have any internal reflectors. Unlike ridges 2 and 3a, they have relatively smooth surfaces, with no observed fault traces.

Although ridges 1, 2, and 3a differ from the Peridotite Ridge, having gentler slopes (ridge 2 has slopes of 6-12°) and asymmetric flanks, peridotite ridges are not the only structures interpreted to be exhumed mantle. In the SIAP profile IAM-9 a 100 km wide zone of interpreted exhumed mantle has rugged peaks that are about half as tall as the adjacent peridotite ridges (Dean et al, 2000), similar to ridges 2 and 3a. In addition, while M0 has often been interpreted to indicate the presence of oceanic crust, this is not conclusive because magnetic anomalies also occur in other settings. Combinations of basalt, gabbro, and serpentinized peridotite can also form weak magnetic anomalies on the seafloor. Sibuet et al (2007) demonstrated that the weak magnetic anomalies occurring within the OCT can be generated by serpentinization of the mantle during exhumation.

Another possibility is that the peridotite is intruded by sills (Sibuet et al, 2007). Therefore, western ridges 5, 4 and 3b are characteristic of the Peridotite Ridge, whereas ridges 1, 2 and 3b are more similar to non-ridge exhumed mantle in the SIAP then to the Peridotite Ridge (or they may be composed of oceanic crust, as described above). M0 is weak, and may reflect either the presence of oceanic basaltic crust, sills intruded into exhumed mantle, or serpentinization of exhumed mantle.

Figure 4.5 The western ridges 1,2 and 4. a) ridge 1-2 from WE2, b) ridge 4 from WE1, and c) ridges 1, 2 from WE1. a) and c) correspond to the same ridge complex on the two profiles, and are taken from the same E-W positions. See Figure 4.4 for locations.
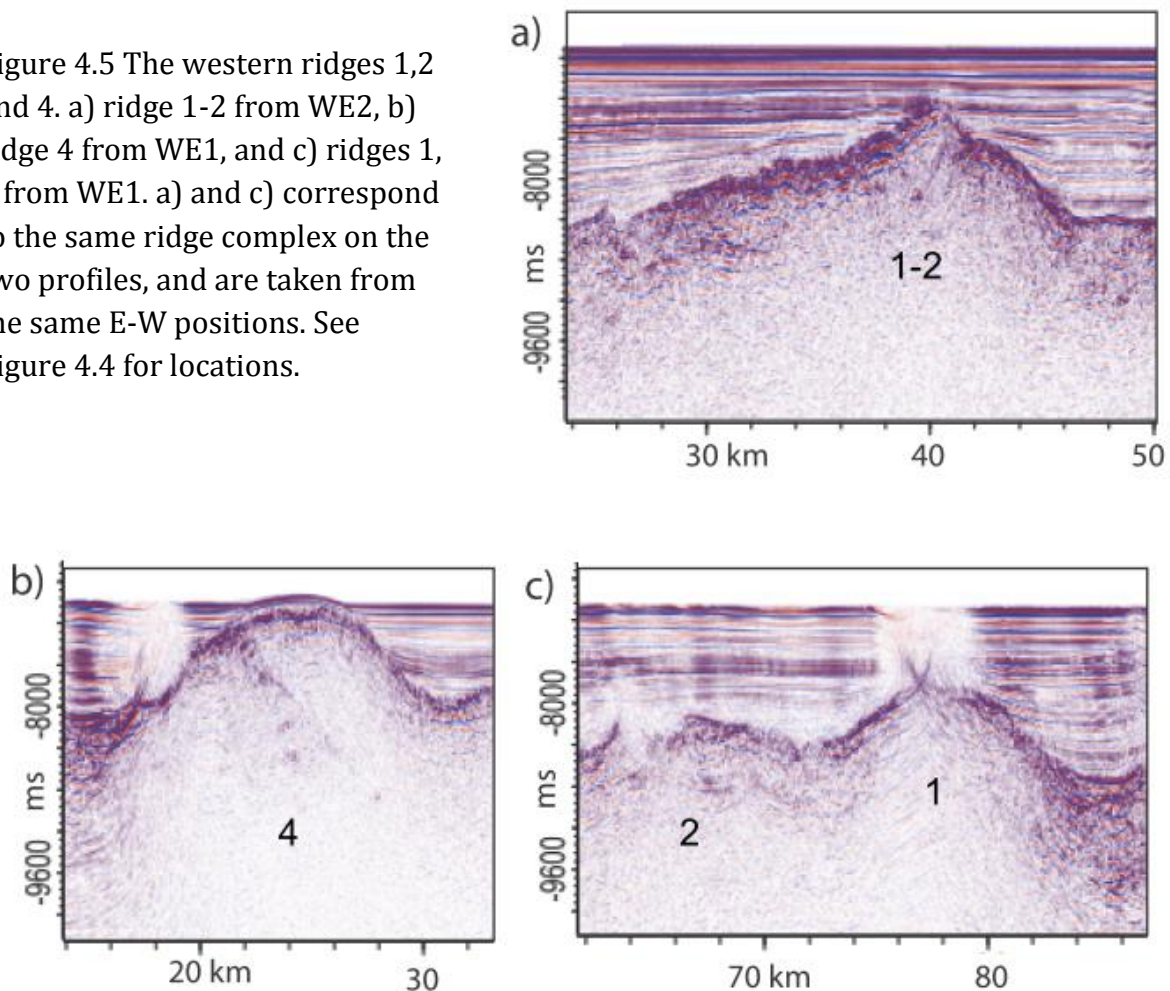
4.7. Implications: synthesis model

Examination of the two new Western Extension profiles along the Galicia margin reveals that ridges 1, 2 and 3a are most similar to thin oceanic crust and/or exhumed peridotite, while the westernmost ridges 3b, 4 and 5 look most similar to the Peridotite Ridge. Taken together, these observations imply more complexity in the Galicia OCT then previously assumed. We suggest that the early stages of spreading were accompanied by both volcanic activity and mantle exhumation, and a brief episode of volcanic activity during an overall period of mantle exhumation may have produced the configuration we see today (Figure 4.9). Exhumed mantle is characteristic of both OCT zones and ultra-slow or slow spreading centers. Such a complex transition, going from exhuming continental mantle to exhuming oceanic mantle with interspersed volcanism, may not be obvious in seismic velocities or reflection profiles because there is not a significant impedance contrast between the mantle rock exhumed in the two domains.

Of interest is that exhumed mantle has also been documented along slow and ultra-slow spreading centers, interspersed with basaltic crust. In that setting, exhumed mantle is exposed along oceanic core complexes analogous to on-land metamorphic core complexes (Cann et al., 1997; Tucholke et al, 1998; Ranero and Reston, 1999). Oceanic core complexes are described as domal geologic structures composed of ductilely deformed mantle rock that underlie a ductile-to-brittle high-strain zone, and have experienced several kilometers of normal-sense displacement during extension (Whitney et al, 2013). The Atlantis Massif is an oceanic core complex just west of the Mid Atlantic Ridge. The domal section of the ridge is about 11 km long, with a total width of 20 km of exposed mantle material. The core

complex reaches a height of 1-1.2 km above the adjacent seafloor (Whitney et al, 2013). This geometry is similar in dimension and height to WE ridges 4 and 5. Ridge 4 is about 12 km wide, and 1.1-1.2 km tall, although it is buried beneath post-rift sediment. Ridge 5 may extend beyond the profile, but it is at least 12 km wide, and 1.2-2 km tall. The similarities between these two WE ridges and oceanic core complexes allow that they may have formed through a similar process, and the occurrence of local oceanic core complexes may be representative of the OCT. Oceanic core complex – style exhumation may have generated ridges 3b, 4 and 5, interspersed with episodic and localized volcanism responsible for ridges 1 and 2, as well as magnetic anomaly M0 (Figure 4.9). In fact, a similar scenario has been interpreted for the Newfoundland SCREECH 1 profile. In Figure 4.5, Hopper et al (2004, 2006) noted a zone of thin ultra-slow spreading that generated oceanic crust. Just to the west of that zone, they interpret an area of exhumed mantle that was later covered by basalt flows once volcanism restarted.

We also note that ultra-slow or slow seafloor spreading may not result in perfectly symmetric features on the two sides of a conjugate margin. If faults on opposite sides of a spreading axis are active simultaneously and slip at the same rates, then matching oceanic core complexes / exhumed mantle domains might be expected to form and be preserved on both sides of the spreading axis. However, any variations in fault activity or volcanism can lead to differences in lithosphere structure and composition e.g., variations in ocean crust production versus mantle exhumation (Cannat et al., 2006; Whitney et al, 2013). Therefore, the differences in the SCREECH 1 and WE 1 & 2 profiles may be explained by different processes occurring on either side of the margin as lithospheric extension transitioned to

seafloor spreading. Consistent with this idea, drilling on the Newfoundland margin along the nearby SCREECH 2 transect (Shillington et al, 2006) recovered diabase sills in the OCT zone, suggesting that there might have been relatively more magma and associated volcanism on the western side of the nascent spreading axis, allowing for the formation of thin oceanic crust (Figure 4.5) while mantle was being exhumed on the eastern side (Figure 4.9). Peron-Pinvidic et al (2007, 2009) also showed that the final breakup of the two continents was gradual, and not a sharp, mappable event, which is also consistent with our hypothesis. Pulses of magma in-between episodes of mantle exhumation argue for such a gradual transition, especially if Galicia experienced enduring periods of oceanic mantle exhumation during the onset of seafloor spreading.

4.8. Conclusions

The aim of our study was to investigate how the continental breakup process and resulting ocean-continent transition are recorded along the Galicia Bank margin, and to test models with new data farther to the west of the known peridotite ridge. The eastern sections of the Western Extension profiles, spanning five continental blocks and the Peridotite Ridge, confirms previous interpretations of the architecture of the distal continental margin. The increased resolution shows new features, such as the presence of additional thin and faulted block(s) in the basin on the east flank of the Peridotite Ridge, and the dip of the S-reflector under this basin; these and other structures will be the focus of subsequent studies utilizing the 3D portion of the study area.

Figure 4.9 Model of lithospheric structure resulting from the transition from continental extension to seafloor spreading. Exhumation of continental mantle results in the formation of peridotite ridges, while episodic volcanism produces local thin basaltic crust. Asymmetric processes during initial rifting and spreading results in contrasting structures on two margins (Modified after Whitney et al, 2013 and Cannat et al, 2006).
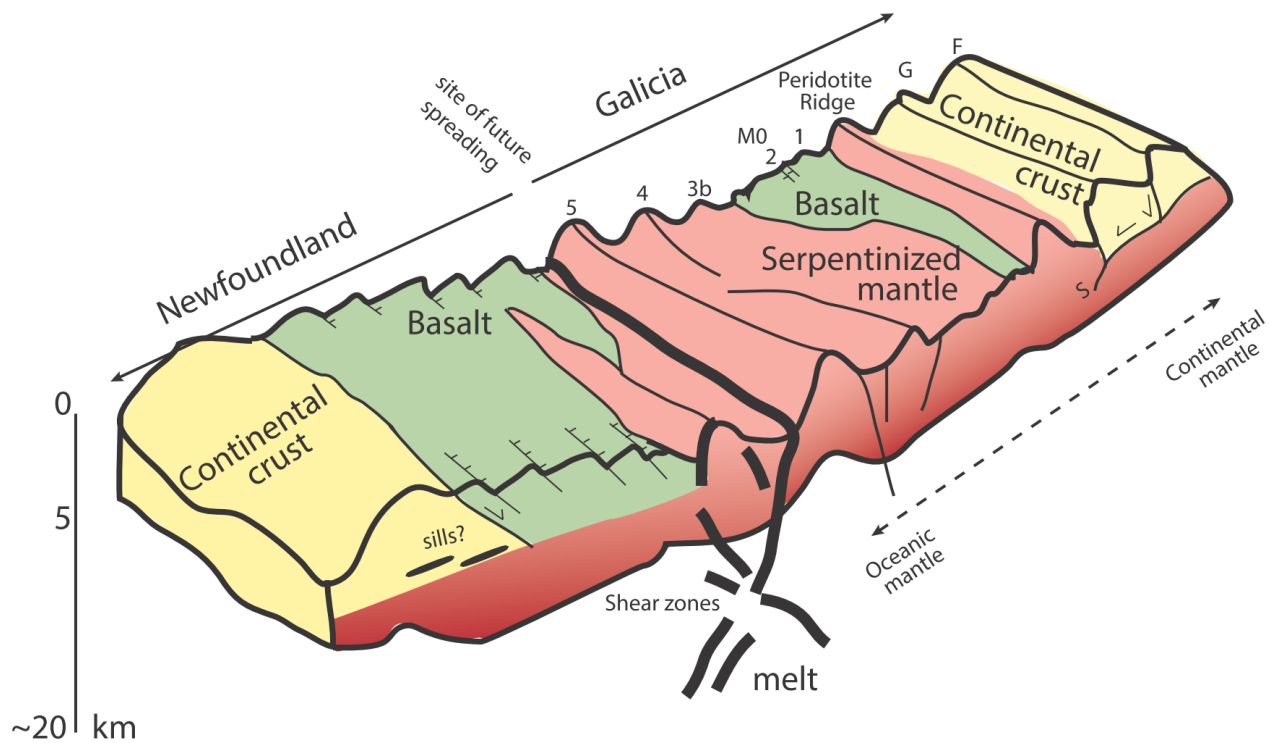
The 2D extensions west of the Peridotite Ridge revealed five new basement ridges, with widely disparate characteristics. The three possibilities considered for the origin of basement were 1) continental crust, 2) oceanic crust and 3) exhumed mantle. None of the ridges show the strong layering and syn-rift stratigraphy characteristic of continental blocks, nor did they show reflectors characteristic of detachment or fault surfaces. Comparisons to oceanic crust found in the SIAP, Newfoundland and Labrador demonstrated some similarities for western ridges 1-2 and 3a. In contrast, western ridges 3b, 4 and 5 show similarities with exhumed mantle in the SIAP and the Peridotite Ridge in

Galicia. These western ridges also display similar profiles to small oceanic core complexes that had been subsequently buried by sediments. We propose that the western ridges result from a combination of oceanic core complex formation and generation of new ocean crust, defining a new model for the transition from continental extension to ultra-slow or slow spreading, one which likely applies in both Galicia, the Sothern Iberia Abyssal Plain and possibly elsewhere. This is consistent with a gradual ocean-continent transition, and thus may not correspond with a distinct compositional or structural boundary, particularly when the transition involves transferring from exhuming continental mantle to exhuming oceanic mantle, as interpreted on the Galicia side of the margin (Figure 4.9). In addition, the potential for different periods and degrees of activity for detachment faults and volcanism on either side of a conjugate margin, means that the structure of the Galicia Margin may differ from the Newfoundland one. This can explain the fact that SCREECH 1 (Hopper et al, 2004, 2006) and WE1 appear to exhibit different amounts of oceanic basalt and exhumed mantle in their respective transition zones.

Subsequent work in the area, including velocity analysis from OBS's deployed along WE1 will add additional insight into the nature of the western basement ridges in Galicia. In addition, as western ridge 5 emerges above the post rift sediments, it would be an excellent location for future dredging or drilling.

References

Albertz, M., Beaumont, C., and Ings, S.J., 2010, Geodynamic modeling of sedimentation-induced overpressure, gravitational spreading, and deformation of passive margin mobile shale basins, in Wood, L., ed, Shale tectonics: AAPG Memoir 93, 29-62, doi 10.1306/13231307M933417.

Alzaga-Ruiz, H., Granjeon, D., Lopez, M., Seranne, M. and Roure, F., 2009, Gravitational collapse and Neogene sediment transfer across the western margin of the Gulf of Mexico: Insights from numerical models, Tectonophysics, 470:1-2, 21-41.

Banks, C.J. and Warburton, J., 1986, "Passive-roof" duplex geometry in the frontal structures of the Kirthar and Sulaiman mountain belts, Pakistan, Journal of Structural Geology, 8, 229-237.

Benesh, N.P., Plesch, A., Shaw, J.H., and Frost, E.K., 2007, Investigation of growth fault bend folding using discrete element modeling: Implications for signatures of active folding above blind thrust faults, J. Geophysical Research, 112, B03S04.

Benesh, N.P., Plech, A., and Shaw, J.H., 2014, Geometry, kinematics, and displacement characteristics of tear-fault systems: An example from the deep-water Niger Delta, AAPG Bulletin, 98:3, 465 – 482.

Beslier, M.O., Ask, M., and Boillot, G., 1993, Ocean Continent Boundary in the Iberia Abyssal-Plain from Multichannel Seismic Data, Tectonophysics, 218:4, 383-393.

Bilotti, F., and Shaw, J.H., 2005, Deep-water Niger Delta fold and theust belt modeled as a critical-taper wedge: The influence of elevated basal fluid pressure on structural styles, AAPG Bulletin, 89:11, 1475-1491, doi 10.1306/06130505002.

Boillot, G., E. L. Winterer, and A. W. Meyer, 1987, Proc. Ocean Drill. Program Initial Rep., 103, Ocean Drilling Program, College Station, TX.

Bonini, M., 2001, Passive roof thrusting and forelandward fold propagation in scaled brittle-ductile physical models of thrust wedges, J. Geophys. Res.,106:B2, 2291-2311.

Bonini, M., 2007, Deformation Patterns and Structural vergence in brittle –ductile thrust wedges: An additional analogue modeling perspective, 29, 141-158.

Borgmeyer A., 2010, Three-dimensional geometries of rifting on a hyperextended margin; Interpretation of seismic reflection profiles from the Deep Galicia Basin, Iberia, Master's thesis, Rice University, Houston, Texas, 64.

Briggs, S.E., Davies, R.J., Cartwright, J.A., and Morgan, R., 2006, Multiple detachment levels and their control on fold styles in the compressional domain of the Niger Delta, Basin Research, 18:4, 435-450, doi 10.1111/j.1365-2117.2006.00300.x.

Brun, J.P., 1999, Narrow rifts versus wide rifts: inferences for the mechanics of rifting from laboratory experiments, Phil. Trans. R. Soc. Lond. A, 357:1753, 695-712.

Burbidge D.R., and Braun, J., 2002, Numerical models of the evolution of accretionary wedges and fold-and-thrust belts using the distinct element method, Geophys. J. Int., 148, 542-561.

Cann, J. R., Blackman, D. K., Smith, D. K., McAllister, E., Janssen, B., Mello, S., Avgerinos, E., Pascoe, A. R., and Escartin, J., 1997, Corrugated slip surfaces formed at ridge-transform intersections on the Mid-Atlantic Ridge: Nature, 385, 329–332.

Cannat, M., Mendel, V., Ruellan, E., Okino, K., Escartin, J., Combier, V., and Baala, M., 2006, Modes of seafloor generation at a melt-poor ultraslow-spreading ridge, Geology, 34, 605–608, doi:10.1130/G22486.1.

Cardozo, N., Allmendinger, R.W., Morgan, J.K., 2005, Influence of mechanical stratigraphy and initial stress state on the formation of two fault propagation folds, J. Structural Geology, 27, 1954-1972.

Cohen, H.A., and McClay, K., 1996, Sedimentation and shale tectonics of the northwestern Niger Delta front, Marine and Petroleum Geology, 13:3, 313-328, doi 10.1016/0264-8172(95)00067-4.

Corredor, F., J.H. Shaw, and F. Bilotti, 2005, Structural styles in the deep-water fold and thrust belts of the Niger Delta. AAPG Bulletin, 89:6, 753 – 780, doi 10.1306/02170504074.

Couzens B. A., and Wiltschko, D. V., 1996, The control of mechanical stratigraphy on the formation of triangle zones, Bulletin of Canadian Petroleum Geology, 44:2, 165-179

Couzens-Schultz, B. A., Vendeville, B.C., and Wiltschko D. V., 2003, Duplex style and triangle zone formation: insights from physical modeling, Journal of Structural Geology, 25, 1623-1644

Cundall, P. A., and Strack, O.D.L., 1979, A discret numerical model for granular assemblies, Geotechnique, 29, 47-65.

Dahlen, F.A., 1990, Critical taper model of fold and thrust belts and accretionary wedges, Annu. Rev. Earth Planet. Sci., 18, 55-99, doi 10.1146/annurev.ea.18.050190.000415

Dean, S.L., Morgan, J.K., Fournier, T., 2013, Geometries of frontal fold and thrust belts: Insights from discrete element simulations, J. Structural Geology, 53, 43-53, doi 10.1016/j.jsg.2013.05.008.

Dean, S.M., Minshull, T.A., Whitmarsh, R.B. and Louden, K.E., 2000, Deep structure of the ocean-continent transition in the southern Iberia Abyssal Plain from seismic refraction profiles: the IAM-9 transect at 40°20°N, J. geophys. Res., 105, 5859–5885.

Discovery 215 Working Group 1998, Deep structure in the vicinity of the ocean-continent transition zone under the southern Iberia Abyssal Plain, Geology, 26, 743– 746.

Doust, H., and E. Omatsola, 1990, Niger Delta in divergent/passive margin basins, in J. D. Edwards and P. A. Santogrossi, eds., AAPG Memoir, 48, 201–238.

Funck, T., Hopper, J.R., Larsen, H.C., Louden, K.E., Tucholke, B.E. and Holbrook, W.S., 2003, Crustal structure of the ocean-continent transition at Flemish Cap: seismic refraction results, J. geophys. Res., 108, 2531.

Gordy, P.L, Frey, F.R. and Norris, D.K., 1977, Geological Guide for the CSPG 1977 Waterton-Glacier Park Field Conference, Canadian Society of Petroleum Geologists, Calgary.

Groupe-Galice, 1979, The continental margin of Galicia and Portugal: acoustical stratigraphy, dredge stratigraphy and structural evolution, Initial Reports Deep-Sea Drilling Project, 47:2, 633-662.

Guo, Y., and Morgan, J.K., 2004, Influence of normal stress and grain shape on granular friction: Results of discrete element simulations, J. Geophys. Res., 109, B12305.

Hardy, S., McClay, K., and Muñoz, J.A., 2007, Deformation and fault activity in space and time in high-resolution numerical models of doubly vergent thrust wedges, Marine and Petroleum Geology, 26, 232-248.

Hardy, S., 2008, Structural evolution of calderas: Insights from two-dimensional discrete element simulations, Geology, 36, 927-930.

Henning, A.T., Sawyer, D.S. and Templeton, D.C., 2004, Exhumed upper mantle within the ocean-continent transition on the northern West Iberia margin: Evidence from prestack depth migration and total tectonic subsidence analyses, J. geophys. Res., 109, B05103.

Hopper, J.R., Funck, T., Tucholke, B.E., Larsen, H.C., Holbrook, W.S., Louden, K.E., Shillington, D. and Lau, H., 2004, Continental breakup and the onset of ultraslow seafloor spreading off Flemish Cap on the Newfoundland rifted margin, Geology, 32, 93–96.

Hopper, J. R., Funck, T., Tucholke, B.E., Louden, K.E., Holbrook, W.S., and Larsen, H.C., 2006, A deep seismic investigation of the Flemish Cap margin: implications for the origin of deep reflectivity and evidence for asymmetric break-up between Newfoundland and Iberia, Geophys. J. Int., 164:3, 501-515.

Ings, S.J., and Beaumont, C., 2010, Continental margin shale tectonics: preliminary results from coupled fluid-mechanical models of large-scale delta instability, J. of the Geological Society, 167, 571-582, doi 10.1144/0016-76492009-052.

Jaeger, J. C., and N. G. W. Cook, 1969, Fundamentals of rock mechanics, Chapman and Hall, London, U.K..

Jamison, W.R., 1993, Mechanical stability of the triangle zone: the backthrust wedge, J. Geophy. Res., 98:B11 20015-20030.

Johnson, K. L., 1985, Contact Mechanics, Cambridge Univ. Press, Cambridge, U. K.

Jones, P.B., 1982, Oil and gas beneath east-dipping underthrust faults in the Alberta foothills, In: Powers, R.B., (Ed), Geologic studies of the Cordilleran thrust belt, Rocky Mountain Association of Geologists, 1, 61-74.

Jones, P.B., 1996, Triangle zone geometry, terminology, and kinematics, Bull. Canadian Petroleum. Geology., 44:2, 139-152.

Kostenko, O.V., Naruk, S.J., Hack, W., Poupon, M., Meyer, H., Mora-Glukstad, M., Anowai, C., and Mordi, M., 2008, Structural evaluation of column-height controls at a toe-thrust discovery, deep-water Niger Delta. AAPG Bulletin, 92:12, 1615-1638, doi 10.1306/08040808056.

Kruger, S.W., and Grant, N.T, 2012, The Growth History of Toe Thrusts of the Niger Delta and the Role of Pore Pressure, in K. McClay, J. Shaw, and J. Suppe, eds., Thrust fault-related folding: AAPG Memoir, 94, 357 – 390, doi 10.1306/13251345M943435

Lawton, D.C., Sukaramongkol, C., and Spratt, D.A., 1996, Seismic characterization of a "compound tectonic wedge" beneath the Rocky Mountain foreland basin, Alberta, Bull. Canadian Pet. Geo., 44:2, 258-268.

Lavier, L. L., and Manatschal, G., 2006, A mechanism to thin the continental lithosphere at magma-poor margins, Nature, 440:2, 324-328.

MacKay, P.A., 1996, The Highwood Structure: a tectonic wedge at the foreland edge of the southern Canadian Cordillera, Bull. Canadian Pet. Geo., 44:2, 215-232.

Maloney, D., Davies, R., Imber, J., Higgins, S., and King, S., 2010, New insights into deformation mechanisms in the gravitationally driven Niger Delta deep-water fold and thrust belt, AAPG, 94:9, 1401-1424, doi 10.1306/01051009080.

Manatschal, G., Froitzheim, N., Rubenach M. and Turrin, B.D., 2001, The role of detachment faulting in the formation of an ocean- continent transition: insights from the Iberia Abyssal Plain, Geological Society, London, Special Publications 2001, 187, 405-428.

Manatschal, G., Müntener, O., Lavier, L.L., Minshull, T.A. and Péron-Pinvidic G., 2007, Observations from the Alpine Tethys and Iberia–Newfoundland margins pertinent to the interpretation of continental breakup, Geological Society, London, Special Publications, 282, 291-324.

Maxwell, S.A., 2009, Deformation styles of Allochthonous salt sheets during differential loading conditions: Insights from discrete element models, Master's thesis, Rice University, Houston, Texas, 104 p.

McClay, K., Dooley, T., and Zamora, G., 2003, Analogue models of delta systems above ductile substrates, In: Van Rensbergen, P., Hillis, R.R., Maltman, A.J., and Morley, C.K. (eds), Subsurface Sediment Mobilization, Geological Society, London, Special Publications, 216, 411-428, doi 10.1144/GSL.SP.2003.216.01.27.

Menard, K.P., 2008, Dynamic Mechanical Analysis: A practical introduction, CRC Press, Boca Raton.

Mitra, G., 1994, Strain variation in thrust sheets across the Sevier fold and thrust belt (Idaho– Utah– Wyoming): implications for section restoration and wedge taper evolution. Journal of Structural Geology, 16, 585– 602.

Morency, C., Huismans, R.S., Beaumont, C., and Fullsack, P., 2007, A numerical model for coupled fluid flow and matrix deformation with applications to disequilibrium compaction and delta stability, J. Geophy. Res., 112:B10, 1978-2012, doi 10.1029/2006JB004701.

Morgan, J. K., and M. S. Boettcher, 1999, Numerical simulations of granular shear zones using the distinct element method, 1. Shear zone kinematics and the micromechanics of localization, J. Geophys. Res., 104, 2703-2719.

Morgan, J.K., 2004, Particle dynamics simulations of rate- and state-dependent frictional sliding of granular fault gouge, Pure appl. geophys., 161, 1877–1891.

Morgan, J.K., and McGovern, P.J., 2005, Discrete element simulations of gravitational volcanic deformation: 1. Deformation structures and geometries, Journal of Geophysical Research, 110, B05402

Morgan, J.K., and McGovern, P.J., 2005b, Discrete element simulations of gravitational volcanic deformation: 2. Mechanical analysis, Journal of Geophysical Research, 110:B05403, doi 10.1029/2004JB003253.

Morley C., K., and Guerin, G., 1996, Comparison of gravity driven deformation styles and behaviour associated with mobile shales and salt, Tectonics, 15, 1154-1170, doi 10.1029/96TC01416.

Morley, C.K., 2003, Mobile shale related deformation in large deltas developed on passive and active margins, Van Rensbergen, P., Hillis, R.R., Maltman, A.J. and Morley, C.K.

(eds), Subsurface Sediment Mobilization, Geological Society, London, Special Publications, 216, 335-357, doi 10.1144/GSL.SP.2003.216.01.22.

Morley, C.K., King, R., Hillis, R., Tingay, M., and Backe, G., 2011, Deepwater fold and thrust belt classification, tectonics, structures, and hydrocarbon prospectivity: A review, Earth Science Reviews, 104, 41-91, doi 10.1016/j.earscirev.2010.09.010.

Naylor, M., Sinclair, H.D., Willett, P.A., Cowie, P.A., 2005, A discrete element model for orogenesis and accretionary wedge growth, Journal of Geophy. Research, 110:B12403, doi 10.1029/2003JB002940.

Nilforoushan, F., Koyi, H.A., Swantesson, J.O.H., Talbot, C.J., 2008, Effect of basal friction on surface and volumetric strain in models of convergent settings measured by laser scanner, J. Structural Geology, 30, 366-379.

Pickup, S.L.B., Whitmarsh, R.B., Fowler, C.M.R. and Reston, T.J., 1996, Insight into the nature of the ocean-continent transition off west Iberia from a deep multichannel seismic reflection profile, Geology, 24, 1079–1082.

Péron-Pinvidic, G., Manatschal, G., Minshull, T. A. and Sawyer, D. S., 2007, Tectonosedimentary evolution of the deep Iberia–Newfoundland margins:Evidence for a complex breakup history, Tectonics 26, TC2011.

Ranero, C.R., and Reston, T.J., 1999, Detachment faulting at ocean core complexes: Geology, 27, 983–986, doi:10.1130/0091-7613(1999)027<0983:DFAOCC>2.3.CO;2.

Reston, T.J., Krawczyk, C.M. & Klaeschen, D., 1996, The S reflector west of Galicia (Spain): evidence from prestack depth migration for detachment faulting during continental breakup, J. geophys. Res., 101, 8075–8091.

Russell, S.M. & Whitmarsh, R.B., 2003, Magmatism at the west Iberia non-volcanic rifted continental margin: evidence from analyses of magnetic anomalies, Geophys. J. Int., 154, 706–730.

Roure, F., Andriessen, P., Callot, J.P., Ferket, H., Gonzales, E., Guilhaumou, N., Hardebol, N., Lacombe, O., Malandain, J., Mougin, P., Muska, K., Ortuño, S., Sassi, W., Swennen, R. & Vilasi, N., 2010, The use of paleo-thermo-barometers and coupled thermal, fluid flow and pore fluid pressure modelling for hydrocarbon and reservoir prediction in fold and thrust belts. Eds., Goffey G.P., Craig J., Needham T. and Scott R., Hydrocarbons in contractional belts, Geological Society of London Spec. Pub. 348, 87-114.

Sans, M., Verges, J., Gomis, E., Pares, J.M., Schiattarella, M., Trave, A., Calvet, F., Santanach, P., and Doulcet, A., 2003, Layer parallel shortening in salt-detached folds: constraint on cross-section restoration, Tectonophysics, 372, 85-104.

Sanz, P.F., Borja, R.I., Pollard, D.D., 2007, Mechanical aspects of thrust faulting driven by far-field compression and their implications to fold geometry, Acta Geotechnica 2, 17–31.

Sassi, W. and Faure, J., 1996, Role of faults and layer interfaces on the spatial variation of stress regimes in basins: inferences from numerical modelling, Tectonophysics, 266, 101-119.

Sawyer, D.S., Whitmarsh, R.B., and Klaus A., 1994, Proc. Ocean Drill. Program Initial Rep., 149, Ocean Drilling Program, College Station, TX.

Sawyer, D.S., Reston, T., Gussinye, M.P., Zelt, C.A., Austin, J.A., Nakamura, Y., Danobeitia, J., Cordoba D., and Scientific Party of Ewing Cruise 97-05, 1997, The Iberia Seismic Experiment (ISE97): MCS reflection profiles, EOS, 78, F468.

Shillington, D. J., Holbrook, W.S., Van Avendonk, H.J.A., Tucholke, B.E., Hopper, J.R., Louden, K.E., Larsen, H.C., and Nunes, G.T., 2006, Evidence for asymmetric nonvolcanic rifting and slow incipient oceanic accretion from seismic reflection data on the Newfoundland margin, J. Geophys. Res., 111, B09402, doi:10.1029/2005JB003981.

Sibuet, J.C., Srivastava, S., and Manatschal, G., 2007, Exhumed mantle-forming transitional crust in the Newfoundland-Iberia rift and associated magnetic anomalies, J. Geophys. Res., 112, B06205.

Skuce, A.G., 1996, Frontal Foothills structures in central Alberta: the thin end of the intercutaneous wedge?, Bull. Canadian Pet. Geo., 44:2 153-164.

Slotboom, R.T., Lawton, D.C., Spratt, D.A., 1996, Seismic interpretation of a triangle zone at Jumping Pound, Alberta, Bull. Canadian Pet. Geo., 44:2, 233-243.

Srivastava, S.P. and Keen, C.E., 1995, A deep seismic reflection profile across the extinct Mid-Labrador Sea spreading center, Tectonics, 14, 372–389.

Srivastava, S.P., Sibuet, J.-C., Cande, S., Roest, W.R. & Reid, I.D., 2000, Magnetic evidence for slow seafloor spreading during the formation of the Newfoundland and Iberian margins, Earth planet. Sci. Lett., 182, 61–76.

Stockmal, G.S., MacKay, P.A., Lawton, D.C., and Spratt, D.A., 1996, The Oldman River triangle zone: a complicated tectonic wedge delineated by a new structural mapping and seismic interpretation, Bull. Canadian Pet. Geo., 44:2, 202-214.

Stockmal, G.S., Lebel, D., McMechan, M.E., and MacKay, P.A., 2001, Structural style and evolution of the triangle zone and external Foothills, southwestern Alberta: Implications for thin-skinned thrust-and-fold belt mechanics, Bulletin Canadian Petroleum Geology, 49:4, 472.

Stockmal, G. S., Beaumont, C., Nguyen, M., and Lee, B., 2007, Mechanics of Thin-Skinned Thrust-and-Fold Belts: Insights from Numerical Models, In: Sears, J., Harms, T., Evenchick, C.A., (Eds), Whence the Mountains? Inquiries into the Evolution of Orogenic Systems: A Volume in Honor of Raymond A. Price, Geological Society of America, Spec. Paper 433, 63-99.

Storti, F., and McClay, K., 1995, Influence of syntectonic sedimentation on thrust wedges in analogue models, Geology, 23, 999-1002, doi 10.1130/0091-7613.

Strayer, L.M., and Suppe, J., 2002, Out-of-plane motion of a thrust sheet during along-strike propagation of a thrust ramp: a distinct-element approach, Journal of Structural Geology, 24, 637–650.

Strayer, L.M., Erickson, S.G. and Suppe, J., 2004, Influence of growth strata on the evolution of fault-related folds; distinct-element models, ed. McClay, K.R., Thrust Tectonics and Hydrocarbon Systems, AAPG Memoir 82, 413–437.

Tucholke, B.E., Lin, J., and Kleinrock, M., 1998, Megamullions and mullion structure defining oceanic core complexes on the Mid-Atlantic Ridge: Journal of Geophysical Research, 103, 9857–9866, doi:10.1029/98JB00167.

Tucholke, B.E., and Scientific Shipboard Party, 2004, Proc. Ocean Drill. Program Initial Rep., 210, Ocean Drilling Program, College Station, TX.

Tucholke, B.E., Sawyer, D.S., and Sibuet, J.C., 2007, Breakup of the Newfoundland Iberia rift, Geol. Soc. Spec. Publ., 252:1, 9-46.

Vann, I.R., Graham, R.H., and Hayward, A.B., 1985, The structure of mountain fronts, Journal of Structural Geology, 8:3, 215-227

Vidal-Royo, O., Hardy, S., and Muñoz, J.A., 2010, Influence of multiple décollement stratigraphy and growth strata on a detachment fold development: insights from 2D Discrete-Element Modelling and application to Pico del Águila anticline (External Sierras, Spanish Southern Pyrenees), Trabajos de Geología, Universidad de Oviedo, 30, 303-308.

Weiner, R.W., Mann, M.G., Angelich, M.T., and Molyneux, J.B., 2010, Mobile shale in the Niger Delta: characteristics, structure, and evolution, in Wood, L., ed, Shale tectonics: AAPG Memoir, 93, 145-161, doi 10.1306/13231313M933423.

Whitmarsh, R. B., and P. R. Miles, 1995, Models of the development of the West Iberia rifted continental margin at 40°30′N deduced from surface and deep-tow magnetic anomalies, J. Geophys. Res., 100:B3, 3789–3806.

Whitmarsh, R.B., White, R.S., Horsefield, S.J., Sibuet, J.-C., Recq, M. and Louvel, V., 1996, The ocean-continent boundary off the western continental margin of Iberia: crustal structure west of Galicia Bank, J. geophys. Res.,101, 28291–28314.

Whitmarsh, R.B., Beslier, M.-O., Wallace, P.J. and Shipboard Scientific Party, 1998, Proceedings of the Ocean Drilling Program, Initial Results, 173, 1–294, College Station, Texas, Ocean Drilling Program.

Whitney, D.L., Teyssier, C., Rey, P., and Buck, W.R., 2013, Continental and oceanic core complexes, GSA Bulletin, 125:3/4, 273–298, doi: 10.1130/B30754.1.

Wilson, R.C.L., Manatschal, G. and Wise, S., 2001, Rifting along non-volcanic passive margins: stratigraphic and seismic evidence from the Mesozoic successions of the Alps and western Iberia, Geological Society, London, Special Publications 2001, 187, 429-452.

Woodward, N.B., Gray, D.R., and Spears, D.B., 1986, Including strain data in balanced cross-sections, Journal of Structural Geology 8, 313– 324.

Wu, S., and Bally, A.W., 2000, Slope tectonics—Comparisons and contrasts of structural styles of salt and shale tectonics of the Northern Gulf of Mexico with shale tectonics of offshore Nigeria in Gulf of Guinea, in W. Mohriak and M.Talwani, eds., Atlantic rifts and continental margins: AGU Geophysical Monograph, 115, 151–172, doi 10.1029/GM115p0151.

Yamada, Y., Baba, K., and Matsuoka, T., 2006, Analogue and numerical modelling of accretionary prisms with a décollement in sediments, In: Buiter, S.J.H., and Schreurs, G., (Eds.), Analogue and Numerical Modelling of Crustal-Scale Processes, Geological Society, London, Special Publications, 253, 169-183.

Yang, H., Liu, Y., and Lin, J., 2013, Geometrical effects of a subducted seamount on stopping megathrust ruptures, Geophysical Res. Letters, 40, 1–6.